Studies on Structural, Microstructural and Electrical Properties of Cerium Based High Temperature Semiconducting Complex Oxides

Thesis submitted to the University of Kerala
for the award of the degree of

Doctor of Philosophy
in
Physics

Deepa M

MATERIALS AND MINERALS DIVISION
NATIONAL INSTITUTE FOR INTERDISCIPLINARY SCIENCE AND TECHNOLOGY (CSIR)
THIRUVANANTHAPURAM
KERALA

2010

DECLARATION

I hereby declare that this thesis entitled '**Studies on Structural, Microstructural and Electrical Properties of Cerium Based High Temperature Semiconducting Complex Oxides**' is an independent work carried out by me for the degree of Doctor of Philosophy in Physics of the University of Kerala under the guidance of **Dr. Peter Koshy**, Sr. Deputy Director & Scientist G, National Institute for Interdisciplinary Science and Technology, Thiruvananthapuram and **Dr. P. Prabhakar Rao,** Dy. Director & Scientist F, National Institute for Interdisciplinary Science and Technology, Thiruvananthapuram. I further declare that this thesis or part thereof has not previously been formed the basis for the award of any other degree or diploma.

Deepa M

29.04.2010

CERTIFICATE

This is to certify that the thesis entitled '**Studies on Structural, Microstructural and Electrical Properties of Cerium Based High Temperature Semiconducting Complex Oxides'** is an authentic record of bonafide research work carried out by Mrs. Deepa M for the degree of Doctor of Philosophy in Physics of the University of Kerala under our guidance and supervision.

Dr. Peter Koshy
Sr. Deputy Director &Scientist G
National Institute for Interdisciplinary
Science and Technology (CSIR)
Thiruvananthapuram

Dr. P. Prabhakar Rao
Deputy Director &Scientist F
National Institute for Interdisciplinary
Science and Technology (CSIR)
Thiruvananthapuram

PREFACE

Complex oxides have yielded numerous interesting materials of great importance to solid-state chemists, condensed matter physicists and materials scientists. They exhibit interesting transport properties such as superconductivity, metallic conductivity, semiconductivity, magnetism, etc. Semiconducting oxides are a very important group of materials; their applications span through photocatalysts, negative temperature coefficient (NTC) thermistors, gas sensors, etc. NTC ceramics, commonly polycrystalline spinels (MMn_2O_4, where M=Fe, Co, Ni, Cu and Zn) with a combination of cations of transition metals, are the known materials for thermistors. NTC thermistors are widely used in automotive, house appliances and aerospace as elements for suppression of in-rush current, temperature measurements & control etc. However, the applications of these materials are limited to temperatures below 300°C due to their instability and changing electrical characteristics at high temperature. Hence there is a need to develop new materials having good electrical characteristics at high temperatures.

A new class of semiconducting ceramics in different structural families: pyrochlore, powellite and tetragonal tungsten bronze have been developed by exploiting the variable valency of cerium (Ce). Quaternary oxides in A-Ce-M-M'-O (where A = Ca or Ba, M = Ti or Nb, M' = Nb, Ta, Mo or W) system have

i

been synthesized and the effect of cerium concentration on the structure, microstructure and electrical properties have been studied. The electrical conductivity measurements show that these oxides exhibit semiconducting behavior in a wide temperature range of 30°C to 600°C. The semiconducting nature of the compound is due to the conversion of Ce^{4+} to Ce^{3+} in the lattice to maintain the oxygen stoichiometry in the structure. Suitability of these single phase ceramics for high temperature NTC thermistor applications have been analyzed and aging tests were performed at 500°C for a period of 500h. These ceramics fulfill all the requirements of a material for high temperature NTC applications. The β constant (300°C to 600°C) of 5000 K–11000K provides a sensitivity α in the range of- 0.6% K^{-1} to-1.5% K^{-1} at 600°C. The aging factor is found to be in the range of 1-3% for a period of 500h. The NTC parameters can be tuned to the desired value by changing the Ce concentration in the compositions.

The first chapter of the thesis gives a general introduction to different crystal systems and semiconducting oxides. An overview of the literature on semiconducting properties and NTC thermistors are also presented here. The conventional solid state route adopted for the preparation of complex semiconducting ceramic oxides and different characterization techniques used are given in chapter two. Chapter three discusses the effect of Ce concentration

on the structure, microstructure and electrical properties of the $CaCe_xTiNbO_{7-\delta}$ ($0.5 \leq x \leq 1$) compositions. The X-ray photoelectron spectroscopy (XPS) confirms the presence of cerium in 3^+ state. The powder X-ray diffraction (XRD) analysis explains the displacive disorder in the cubic pyrochlore structure. The conductivity phenomenon of these compounds as a function of temperature and frequency has been studied.

The fourth chapter describes the Ca-Ce-Ti-Nb/Ta-O system with pyrochlore structure. XRD and Raman spectral studies substantiate cubic symmetry with *Fd3m* space group. The effect of sintering temperature on structure, microstructure and electrical properties is also discussed here. The fifth chapter discusses enhancement of the NTC properties of the $(Ca_{0.75}CeTi_{0.25})(Ti_{1.5}Ta_{0.5})O_7$ ceramics by addition of different amount of rare earth oxides such as Gd_2O_3, Sm_2O_3 and Y_2O_3.

Chapter 6 gives a detailed description on novel Ca-Ce-Nb-Mo/W-O NTC ceramics. The XRD and Raman spectral analysis confirms the powellite structure with $I4_1/a$ space group. The thermistor constant β varies from 5000K - 7000K in these compositions and the sensitivity is in the range of - 0.7% /K to -0.9 %/K at 600°C.

The tetragonal tungsten bronze structured NTC ceramics in Ba-Ce-Ti-Ta-O system is described in Chapter 7. The structural and microstructural

change with compositional variation in these compounds has been observed by XRD and scanning electron microscope (SEM). The conductivity mechanism is analyzed using the impedance spectroscopy. The possibility of using these semiconducting oxides for high temperature NTC applications has also been evaluated. The significant conclusions drawn from the above studies along with the scope for future work have been discussed in the final chapter.

Acknowledgements

Many people have helped me in different ways and at different times during the course of this research work. I would take this opportunity to thank some of those few without whom this thesis wouldn't have been a reality.

I am deeply indebted to Dr. Peter Koshy, Sr. Deputy Director and Scientist G, National Institute for Interdisciplinary Science and Technology, Thiruvananthapuram for his incessant encouragement, thought providing discussions and unfailing guidance at every stage of my PhD work. It is with great pleasure that I express my earnest gratitude to Dr. P. Prabhakar Rao, Dy. Director and Scientist F, National Institute for Interdisciplinary Science and Technology, Thiruvananthapuram for teaching me how to organize scientific thoughts, to write scientific documents and to present research effectively. The guidance and support that he has provided at various stages of research programme have been invaluable.

I express my sincere thanks to Dr. K. Ravindran Nair, Scientist (Rtd.) National Institute for Interdisciplinary Science and Technology, Thiruvananthapuram for the fruitful discussions in the early stages of my research work.

CONTENTS

LIST OF TABLES

LIST OF FIGURES

CHAPTER 1

INTRODUCTION AND LITERATURE REVIEW

1.1 Introduction

Ceramics based on oxides, nitrides, carbides, phosphates etc. have found industrial applications for a long time. In modern technology there is an ever increasing demand for materials that can withstand severe conditions of temperature, pressure and radiation field. Recent advances in the synthesis and characterization of new materials have been able to meet these challenges to a certain extent. Ceramic materials of ternary, quaternary or even more complex systems are now available for practical applications in various fields.

Complex oxides have yielded numerous materials of interest to solid state chemists, condensed matter physicists, and materials scientists. This is because of their general refractory character and the chemical stability at high temperatures in oxygen-containing atmosphere. They exhibit interesting transport properties such as super conductivity [Nakano T *et al* 1999], metallic conductivity [Porter L.C *et al* 1988], semiconductivity [Nowotny M.K *et al* 2010], magnetism [Kravchenko E. A and Orlov V. G 2002], ferroelectricity [Kimura H *et al* 2009] etc. These complex oxides crystallize in different structures such as pyrochlore, perovskite, spinel, garnet, powellite, fluorite etc.

Among the above, semiconducting oxides have been widely used in electronic industries because of their unique and useful electrical characteristics. Semiconductors are materials which show a negative

temperature coefficient of resistance and possess a conductivity which lies between that of conductors and insulators. Most commonly used semiconducting oxides are binary oxides of metals such as ZnO, SnO_2, In_2O_3, and CdO. These compounds possess distinctive properties and are now widely used as transparent conducting oxide materials [Sekhar C. Ray *et al* 1998] and gas sensors [Elisabetta D.B *et al* 2000]. Semiconducting oxides have generally used in gas sensors, photovoltaics, rechargeable Li batteries, photoelectrolysis of water for H_2 production, optoelectronic devices and as catalyst for oxidation of organic compounds [Dengwei J *et al* 2010; Monica Lira-Cantu and Frederik C. Krebs 2006; Yanqing Y *et al* 2010].

In addition to these applications, semiconducting ceramics are found to be a good candidate for high temperature sensor applications. Some useful semiconducting oxides have been developed in different structural families such as spinels, perovskites and pyrochlores for temperature measurements. The spinel-structured semiconducting ceramics are the most common materials for the manufacturing of negative temperature coefficient of resistance (NTC) thermistors. However, the application of these materials is limited to temperatures below 300°C due to their instability and changing electrical characteristics. Therefore, there is a need for the development of new materials which have good electrical characteristics at high temperatures.

Semiconducting ceramics consisting of a compound with definite composition and structure showing no decomposition or phase transformation from sintering down to room temperature have been suggested as more suitable for thermistors. The present investigation is focused on the synthesis and development of new semiconducting ceramics in pyrochlore, powellite and tetragonal tungsten bronze type structure for NTC thermistor applications.

1.2 Semiconducting materials

A relatively small group of elements and compounds have an important electrical property, semiconductivity, in which they are neither good electrical conductors nor good electrical insulators. Instead, their ability to conduct electricity is intermediate. This means conductivity is roughly in the range of 10^{-3} S/cm to 10^{-8} S/cm. Active devices made from semiconductor materials are the foundation of modern electronics, including radio, computers, telephones and many other devices. Semiconductor devices include the various types of transistors, solar cells, many kinds of diodes including the light-emitting diode, the silicon controlled rectifier, digital and analog integrated circuits. Solar photovoltaic panels are large semiconductor devices that directly convert light energy into electrical energy. Interestingly, it is not only the resistivity alone that distinguishes semiconductors from other materials, instead, they have a number of properties which differentiate them from insulators and conductors.

1.2.1 Properties of semiconductor

The resistivity of a semiconductor is more than that of an insulator but less than that of a conductor.

1. When a suitable metallic impurity is added to a semiconductor, its current conducting properties change accordingly.

2. Semiconductors possess a negative temperature coefficient of resistance (NTCR) that is, the resistance of a semiconductor decreases with increase in temperature and vice-versa.

3. In semiconductors, current can be carried either by the flow of electrons or by the flow of positively charged "holes" in the material.

A semiconductor can also be defined on the basis of energy bands. Energy band is nothing but the range of energy possessed by an electron in a solid. Thus on the basis of energy bands, semiconductor is a substance which has almost filled valence band and nearly empty conduction band with a very small energy gap (about 1 eV) separating the two.

During the recent decades, advances in semiconductor materials resulted in the development of a wide range of electronic and optoelectronic devices that affected many aspects of the technological society. In general, the main factors that determine basic properties (e.g., optical and electrical properties) of

semiconductors are related to the chemical composition and the crystallographic structure. The electrical conductivity of semiconductors can be varied widely as a function of (i) impurity content (e.g., doping), (ii) temperature (i.e., thermal excitation), (iii) optical excitation (i.e., excitation with photons having energies greater than the energy gap) and (iv) excess charge carrier injection (e.g., in semiconductor devices). It is this capability of controlling the electrical conductivity in semiconductors that offers myriad applications of these materials in a wide variety of electronic and optoelectronic devices.

1.2.2 Intrinsic semiconductors

These are materials whose properties are native to the material; it often implies an undoped semiconductor, examples are Silicon (Si) and Germanium (Ge).

1.2.3 Extrinsic semiconductors

These materials whose properties are influenced or controlled by intentionally added impurity atoms, or by the presence of impurities and/or defects; is often referred to as doped material. Dopants are specific impurity atoms that are intentionally added to a semiconductor in controlled amounts in order to increase either the electron or the hole concentration. Among dopants, donors are impurity atoms which increase the electron concentration, i.e., n-

type dopant, whereas acceptors are impurity atoms which increase the hole concentration, i.e., p-type dopant. In general, n-type semiconductor is a donor-doped material or a semiconductor containing more electrons than holes, and p-type semiconductor is an acceptor doped material or a semiconductor containing more holes than electrons. The majority carriers are the most abundant carriers in a given semiconductor sample, i.e., electrons in n-type and holes in p-type semiconductor; and minority carriers are the least abundant carriers in a given semiconductor sample, i.e., holes in n-type and electrons in p-type semiconductor.

The important elemental semiconductors are group IV materials, such as silicon (Si), germanium (Ge) and diamond (C). These group IV elemental materials all have diamond crystal structure, i.e., each atom is in a tetrahedral configuration with four nearest atoms, and thus they are also referred to as tetrahedrally-bonded semiconductors. Another group IV elemental semiconductor having such a structure is gray Tin (Sn).

1.2.4 III–V Compounds

The III–V compounds (e.g., GaAs, GaP, GaN, AlAs, InSb, InAs, and InP) are important semiconductors for various device applications. In general, these materials crystallize with a relatively high degree of stoichiometry and most of them can easily be obtained. Many of these compounds (e.g., GaAs,

InAs, InP, and InSb) have direct energy gaps and high carrier mobilities. Thus, the common applications of these semiconductors are in a variety of optoelectronic devices for both the detection and generation of electromagnetic radiation and also in high-speed electronic devices.

1.2.5 II–VI Compounds

The Zn and Cd chalcogenides (i.e., compounds with O, S, Se, and Te) cover a wide range of electronic and optical properties due to the wide variations in their energy gap. These compounds are also relatively easily miscible, which allows a continuous "tuning" of various properties. Some important commercial applications of these compounds include phosphors in lighting and various display applications (CRT and thin-film electroluminescent flat displays, e.g., ZnS: Ag and ZnS: Mn), infrared photodetectors for imaging systems, protective windows and optical elements (ZnSe and ZnS), nuclear radiation detectors (CdTe) and solar cells (CdS and CdTe). Other potential applications include short-wavelength light emitting devices (e.g., blue laser) and integrated optoelectronic systems (with Si and GaAs) for optical processing and computation.

1.2.6 IV–VI Compounds

The lead chalcogenides (i.e., PbS, PbSe, and PbTe) are characterized by narrow energy gaps, high carrier mobilities and high dielectric constants. The

unique feature of the direct energy gap in these compounds is that it increases with increasing temperature (i.e., the energy gap has a positive temperature coefficient, PTC), in contrast to the temperature behaviour of the energy gap in other elemental and compound semiconductors that have a negative temperature coefficient. Main applications of these compounds are in light-emitting devices and detectors in the infrared spectral region.

1.2.7 I-III-VI$_2$ Compounds

The compound semiconductors such as $CuAlS_2$, $CuGaS_2$ and $CuInSe_2$ are of interest in various device applications. These semiconductors have the direct energy gaps in the range between about 1 and 3.5 eV, and they crystallize in the tetragonal structure, which is close to the structure of a mineral chalcopyrite. Some possible applications of the compound semiconductors include, e.g., (i) light emitting devices based on a wide energy-gap material such as with the energy gap of 3.5 eV that would accommodate visible (including blue) luminescence centers and (ii) photovoltaic solar cells with the energy gaps of 1.04 and 1.53 eV, respectively. In solar cells, semiconductor compounds that contain magnetic ions (e.g., Cr, Mn, Fe, Co, Ni, and Eu) may also exhibit magnetic properties. For example, some oxide semiconductors, such as FeO, NiO, and EuO, exhibit various magnetic properties (e.g., FeO and NiO are antiferromagnetic materials, EuO and EuS

9

are semiconducting ferromagnetic materials). Other magnetic semiconductors include diluted magnetic semiconductors, such as $Cd_{1-x}Mn_xTe$, $Pb_{1-x}Mn_xTe$ and $In_{1-x}Mn_xAs$ in which a fraction of nonmagnetic cations are substituted by magnetic ions. Such materials exhibit both semiconducting properties and magnetic behaviour. Depending on the amount of the magnetic ions substituting for nonmagnetic cations and also on temperature, diluted magnetic semiconductors can exhibit various magnetic properties.

1.2.8 Organic semiconductors

The general advantages of organic semiconductors include their diversity and relative ease of changing (accommodating) their properties to specific applications. Some examples of organic semiconductors include materials, such as anthracene, $C_{14}H_{10}$ and polyacetylene. The electrical conductivity of polyacetylene can be varied by many orders of magnitude by doping with donors (e.g., alkali metals) or acceptors (e.g., iodine). Early experiments, several decades ago, have demonstrated that anthracene, as well as others, are photoconductors. In fact, it should be noted that the first practical application of anthracene (as the photoconductor) was as a photoreceptor material in imaging systems (i.e., electro photography). Currently various organic photoreceptors are widely employed in these applications, offering low cost and relative ease of preparation in flexible configurations.

1.2.9 Oxide semiconductors

Oxide semiconductors are also referred to as semiconductor ceramics. These are often polycrystalline and polyphase materials with grain sizes in the range between about 1 to 10μm and the properties of the grains and grain boundaries play a crucial role in both the understanding and applications of these materials. In this context, the control of the composition and microstructure of the grains and, especially grain boundaries are most important challenges in developing these materials. It has been established that (i) the grain boundaries generally have an associated space–charge region controlled by the defect structure of the material, (ii) the grain boundaries are paths for the rapid diffusion for various impurities and (iii) grain boundary segregation, precipitation and oxidation typically affect various properties of these materials. Some examples of the oxide semiconductors (with corresponding energy gaps) are Cu_2O (2.1eV), Bi_2O_3 (2.8eV), ZnO (3.4eV), SnO_2 (3.7eV), $BaTiO_3$ (3eV), $SrTiO_3$ (3.3eV), $LiNbO_3$ (4eV) and these materials are employed in a variety of electronic devices and sensors, such as (i) PTC thermistors (ii) varistors (i.e., resistors with nonlinear, but symmetric, current–voltage characteristics) that are used for the protection of electronic devices and circuits (iii) capacitors of high dielectric constant that can be

11

employed in MOS structures (in dynamic random access memory, DRAM) (iv) gas sensors and (v) electro-optic modulators.

1.3 Negative Temperature Coefficient of Resistance (NTCR) properties

Sensors play a major role in any control and automation system. The sensors convey the details of the status of the real world in a more precise way than any human senses can. They exist to cover most measurable quantities of the real world and include motion, temperature proximity, light, sound moisture and many more. Temperature can be measured via a diverse array of sensors. All of them infer temperature by sensing some change in physical characteristics.

There are mainly four types of temperature sensors. Those are categorized as follows: (i) thermocouples, (ii) resistance temperature detectors (RTDs), (iii) integrated circuit (IC) sensors and (iv) thermistors. Obviously, the choice of a particular sensor depends on the required accuracy, speed of response, temperature range, thermal coupling, environment (chemical, electrical or physical) and cost. Thermocouples are widely used as temperature sensors because they are small, robust, relatively inexpensive, easy to use and cover the widest temperature range. They are especially useful for making measurements at extremely high temperatures (up to 2300°C). Nonetheless, they must be shielded from harsh atmospheres and liquids due to corrosion

degradation. The most common metals used for the fabrication of thermocouples are iron, platinum, rhenium, tungsten, copper, alumel (Al–Ni alloy), cromel (Ni–Cr alloy) and constantan (Cu–Ni alloy) [McGee T.D 1988]. The output given by thermocouples is only in the range of a few millivolts; therefore they require precision amplification for further information processing. Nevertheless, their main disadvantages are associated with lower sensitivity (microvolts per degree) and accuracy in comparison with thermistors, and the need for a reference temperature. Thermocouples are characterized by a larger linearity than thermistors, but a smaller linearity than RTDs. Unlike thermocouples, RTDs, ICs and negative temperature coefficient of resistance (NTCR) thermistors are passive sensors that require current excitation to produce a voltage output, which becomes larger than that given by thermocouples. Modern Si- and Ge-based semiconductors are often integrated into multifunction ICs, which offer reasonable accuracy and high linearity over an operating temperature range of $-55^{o}C$ to $+150 ^{o}C$. In some industrial applications below 600°C, RTDs are replacing thermocouples. Nevertheless, when compared with NTCR thermistors, platinum RTDs are less sensitive to small temperature changes, and have a much slower response time. In fact, thermistors' high sensitivity (typically between $-2\%/ ^{o}C$ and $-6\%/ ^{o}C$, at $25^{o}C$) allows the detection of minute variations in temperature which

13

sometimes could not be observed with an RTD or thermocouple. In practice, only electronic semiconductors are used as materials for NTCR sensors. In oxide semiconductors the concentration of charge carriers is determined solely by the doping level, however their mobility is temperature activated.

The relation between resistance and temperature for a negative temperature coefficient thermistor is expressed by the following equation

$$R_T = R_N \left[\beta \left(\frac{T_N - T}{TT_N} \right) \right] \qquad (1.1)$$

where R_T is the resistance at temperature T, R_N is the resistance at temperature T_N known, and β is a thermistor characteristic parameter. Rewriting and rearranging the terms of equation (3), β can be derived as follows:

$$\beta = \left[\frac{TT_N}{T_N - T} \right] \ln \left(\frac{R_T}{R_N} \right) \qquad (1.2)$$

The thermistor sensitivity is defined by the temperature coefficient of resistance α, which can be expressed as a function of the β parameter, according to the following equation:

$$\alpha = (1/R)[d(R)/dT] = -\beta/T^2 \qquad (1.3)$$

This indicates that the temperature sensitivity decreases with increasing temperatures. In most commercial spinel-based NTCR ceramics, the β-values vary between 2000 and 5000 K, which imparts room temperature values

ranging from -2.2 and -5.5%/K, respectively. In order to fulfill the requirements imposed by each specific application, most electroceramic manufacturers offer thermistor components in a wide variety of designs, ranging from surface-mounted to radial or axial leaded packages, as illustrated in Fig. 1.1. The electrical characteristics of these components can be geometrically and chemically tailored to meet specific requirements.

Fig.1.1 Examples of NTCR components: (a) leadless (b,c) lead space(d) glass-encapsulated (e) resin-encapsulated (f) SMD(surface-mounted device) and (g,h) probe sensors (Courtesy from: EPCOS AG, Germany).

The first evidence for the NTCR behaviour was registered on February 21, 1833 by the English natural philosopher Michael Faraday, who observed the resistance of silver sulphide, Ag_2S, to decrease with increasing temperature

[Faraday M 1833]. Nevertheless, this phenomenon remained a mere scientific curiosity for nearly 100 years, until the observation of similar response in transition-metal oxides such as Fe_3O_4, CoO, and NiO. This discovery prompted the design of novel instruments, whose fundamental operation was based on the NTCR behavior. In 1930 Samuel Ruben suggested the use of fused mixtures of Cu_2S and Sb_2S to fabricate temperature measurement devices [Ruben S 1930]. In 1935, the Dutch company Koninklijke Philips Electronics N.V presented a ''novel'' NTCR product, which would be traded under the name ''Starto''. This material consisted basically of a mixture of Hattenleidelheimer clayz with semiconductive silicon or other substance having similar characteristics. But it was less satisfactory than expected [Amstel J 1935].

In the late 1930s, the Bell Telephone Laboratories also embarked on the commercial exploitation of the NTCR behavior exhibited by spinel-structured ceramics. These relatively inexpensive ceramics were based on mixtures of oxides of manganese and iron or oxides of nickel and manganese [Becker J. A *et al* 1947]. Most NTCR ceramics are based on Mn_3O_4 ceramics, where Mn^{3+} is partially replaced by other transition metals such as Ni, Co, Fe, and Cu in order to induce semiconductivity in this rather resistive material. These substitutions lead to the formation of Mn^{3+}/Mn^{4+} pairs on the octahedral sites,

which are essential for electrical conductivity. $NiMn_2O_4$ is definitely the most studied spinel for NTCR applications. This compound is unanimously recognized as an inverse spinel; however, the exact nature of the valences and distribution of the cations have proved to be controversial. In 1957 Dunitz and Orgel investigated the electronic properties of transition-metal oxides, with special emphasis on spinels (e.g., $CuFe_2O_4$, $CuCr_2O_4$, $ZnMn_2O_4$, and $NiCr_2O_4$)[Dunitz J. D and Orgel L. E 1957]. Most of the work on NTC ceramics is dedicated to the spinel structured ceramics, such as the improvement of structural stability at high temperatures, reproducibity of the electrical properties etc [Park K and Han I.H 2005].

Although, transition-metal perovskites have been studied for more than half a century, owing to their fascinating electronic and magnetic properties, their potential as NTCRs has been seriously considered only recently. This investigation was prompted by the fact that commercial NTCRs based on spinels are not suitable for high-temperature applications for a number of different reasons such as too low resistivity and activation energy, poor thermal stability, etc. In 1996, Macher et al. showed that the conductivity of $LaCo_{1-x}M_xO_3$, (M = Al, Ti) can be systematically controlled, enabling a wide application range [Macher K. R *et al* 1996]. Later, in 2000, Feltz reported on the preparation, structure, and electrical properties of $Sr_xLa_{1-x}Ti_{x+y}Co_y^{III}Co_{1-x-2y}^{II}$

17

O_3 $(0<x<1, 0<y<(1-x)/2)$ ceramics. These apparently aging-free materials showed useful properties for NTCR applications to temperatures as high as 500°C [Feltz A *et al* 2000]. Recently, Liu et al. investigated the NTCR behavior exhibited by $BaTiO_3$ based ceramics doped with $BaBiO_3$ composites [Liu X *et al* 2008]. Despite the great chemical versatility exhibited by the pyrochlore structure, only a very few NTC ceramics has been reported with this structure. E. I. Du Pont de Nemours and Company filed a patent which for the first time suggested the use of semiconductive pyrochlores to fabricate NTCR thermistors [Schubert K E 1969]. Recently Nobre and Lanfredi have reported measurable NTCR behavior in $Bi_3Zn_2Sb_3O_{14}$ at temperatures >400°C [Nobre M.A.L and Lanfredi S 2002].

The major problem that NTC ceramic industry facing now is aging of the thermistor material. The change of the electrical properties with respect to time is generally referred to as aging. Aging in NTCR ceramics manifests itself through a noticeable time dependence of both total resistance and sensitivity, which becomes ultimately reflected as a thermometric drift. Apparently, this phenomenon affects all NTCR ceramics to a more or less extent, independent of their composition. And it becomes more predominant in the case of high temperature thermistors. There is an increasing need for sensors capable of operating at extreme conditions, in particular at high temperatures (near

1000°C or above). Semiconducting ceramics consisting of a compound with definite composition and structure showing no decomposition or phase transformation from sintering down to room temperature have been suggested as more suitable for thermistors. In such a single phase ceramic, aging of the electrical properties should be significantly reduced.

In spite of the great chemical versatility exhibited by different crystal structures, the NTC thermistor research was always confined to spinels and perovskites. In the present investigation three different crystal structures namely pyrochlore, powellite and tetragonal tungsten bronze are selected and a new class of semiconducting materials has been synthesized and characterized for NTC thermistor properties. Hence, it is important to discuss about the structure of these types of compounds and the recent research developments taken place in this area.

1.4 Pyrochlore structure

The mineral pyrochlore $(Na,Ca)_2Nb_2O_6(OH,F)$, was named in 1826 from the Greek for *fire* and *green* because some specimens turned green upon ignition [Gaines R.V *et al* 1997]. Pyrochlore also denotes a large group of 22 crystallographically similar minerals that are highly diverse chemically and widely distributed geologically. The general formula is **$A_2B_2O_6(O,OH,F)$**, where, in geological specimens, **A** is a relatively large cation (Ca, K, Ba, Y,

Ce, Pb, U, Sr, Cs, Na, Sb, Bi, and/or Th; radii larger than or equal to 1.0 Å)

and **B** is a smaller cation (Nb, Ta, Ti, Sn, Fe, and/or W); the seventh anion

position in the crystal structure can be occupied by O^{2-}, OH^-, and/or F^- [Gaines

R.V *et al* 1997].
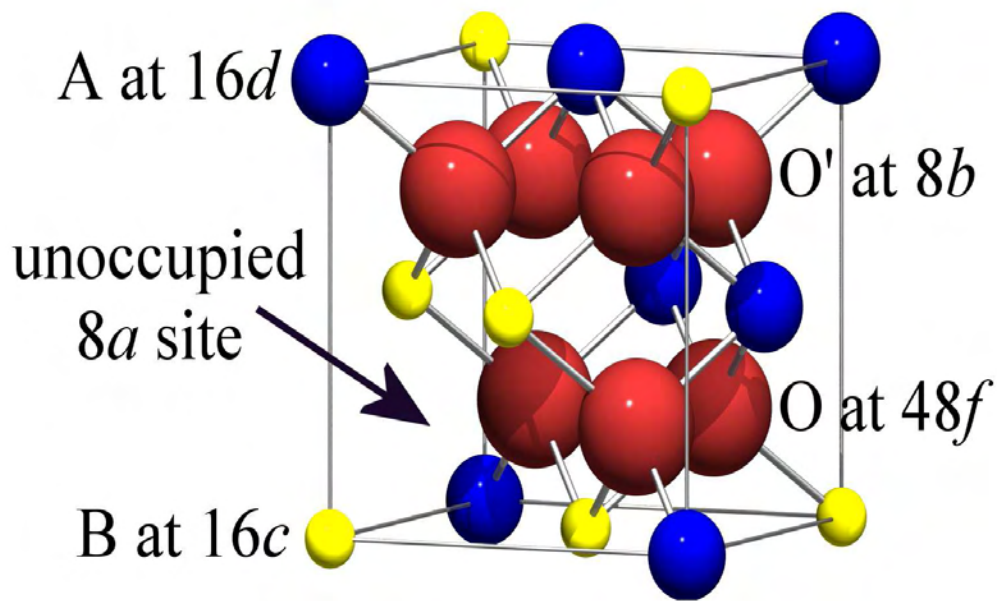
Fig.1.2 Unit cell of pyrochlore. Blue spheres represent A^{3+} cations, yellow B^{4+}
and red O^{2-}

The space group is *Fd3m*, with the unit cell containing eight molecules

($Z = 8$) and four crystallographically nonequivalent sites. A common way of

describing the structure is by fixing its origin on the B site, with atoms located

at the following positions (using Wyckoff notation): A at 16*d*, B at 16*c*, O at

48*f* and O' at 8*b* [Subramanian M.A *et al* 1983]. The only internal positional

variable of the pyrochlore structure is the oxygen x parameter, which characterizes the 48f oxygen atoms.

Different structural modeling can be imagined for the pyrochlore structure such as a structure based on fluorite cell, interpenetrating networks of two types of networks B_2O_6 and A_2O' [Subramanian M.A *et al* 1983] and anticristobalite type. Among these the first two depictions are often used for analysis of the structure.

.
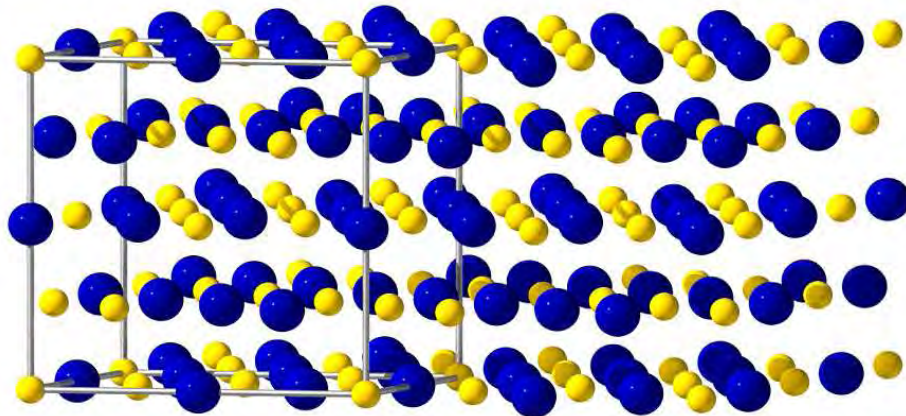
Fig.**1.3** The cationic sublattice of pyrochlore

The most popular depictions are based on a fluorite type of cell. According to those descriptions, the structure is considered as an ordered defective fluorite. The A and B cations form the face centered cubic array and are ordered into rows in the [110] directions. In defect fluorites, the seven oxygen atoms are tetrahedrally coordinated by four random cations and evenly distributed over eight equivalent sites. In the pyrochlore structure, two different

oxygen sites occur: Six oxygen atoms occupy the 48*f* sites, surrounded by two A cations and two B cations, while the seventh oxygen atom occupies the 8*b* site and is surrounded by four A cations. The remaining unoccupied 8*a* site is surrounded by B cations. Finally, the 48*f* anions are shifted toward the smaller B cations by an amount defined by the *x* (48*f*) positional parameter. In the ideal fluorite structure, oxygen positional parameter (*x*) is = 0.375 while for ideal pyrochlore it is 0.3125. Fig.1.2 shows one-eighth of a unit cell of the pyrochlore structure; this partial unit cell is analogous to a single fluorite unit cell.

The pyrochlore structure can be imagined as interpenetrating networks and can be represented as $[A_2O'][B_2O_6]$ which implies that the structure consists of rigid three dimensional corner sharing BO_6 octahedra with A and O' atoms in the large cavities with O and O' atom in the non equivalent sites 48*f* and 8*b* respectively.

There are two types of cation sites, A and B. The larger A cations (usually of the order of 1 Å) is 8 fold coordination with O ions and smaller B cations(of the order of 0.6 Å) in 6 fold coordination with O ions are ordered in alternatively <110> direction. The ionic radius ratio and the oxygen '*x*' parameter decide the formation and stability of the oxide pyrochlores. The ionic radius ratio (RR) is defined as r_A/r_B where r_A is the ionic radius of A

cation with eight coordination and r_B is that of the B cation with six coordination taken from Shannon's table [Shannon R. D 1976]. The RR usually ranges from 1.46 to 1.8.

Pyrochlore, a superstructure, produces a diffraction pattern that contains two subsets of intensity maxima. The first set of reflections corresponds to those characteristic of the parent fluorite structure. These substructure reflections contain only information on the average structure already known to be fluorite-like. The second set of peaks, the superstructure reflections, contains all of the information on the perturbations needed to create the pyrochlore superstructure from an ideal fluorite arrangement. The contributions to these intensities are the difference in scattering power of the species occupying the A and B cation sites, the displacement of O(1) from the ideal position 3/8 1/8 1/8, and the distribution of oxygen vacancies (and thus, in turn, the scattering power of oxygen).

The fundamental reflections of pyrochlore *Fd3m* space group are available in the International tables for X-ray crystallography. However superlattice (when considered as a derivative of fluorite) or ordering reflections are given by (111), (311), (331), (531) at $2\theta = 14°$, $27°$, $36°$, $50°$, etc. and these reflections arise from both cations and anions.

1.4.1 Displacive disordered pyrochlores

Misplaced displacive pyrochlores have also been a point of interest since most of its property arises from the structural specialty of the compound rather than the elemental constitution [Nguyen B *et al* 2008]. Displacive pyrochlores have been a point of controversy for a long time since it was very difficult to accept the fact that small cations like Zn^{2+}, Ti^{4+}, etc can occupy the bigger A site of the pyrochlore; Bi-Zn-Nb-O system are in this category [Matjaz valant and Peter K. Davies 2000]. Very recently Ca containing ternary pyrochlores are also reported with Ti in the A site causing displacive disorder in the system [Nguyen B *et al* 2008; Roth R.S *et al* 2008]. The radius ratio of pyrochlores precludes the formation of rare earth titanate ($Ln_2Ti_2O_7$) cubic pyrochlores for Ln =La to Nd. And especially in the case of Ce containing pyrochlores, pure phase formation is observed to be very difficult [Machida M *et al* 2000]. Moreover it is very difficult to prepare Ce containing pyrochlores through solid state route due to its variable valency.

Very weak reflections of (442)/(006) and (446)/(028) at a 2θ value of 52° and 75° respectively will be observed in the XRD pattern of these kind of pyrochlores. These are the forbidden reflections of the cubic pyrochlore structure indicating the displace disorder in the $O'A_2$ substructure [Nguyen B *et al* 2007]. Here the small B cations will be mixing with the large cations in the

A site for the stabilization of the compound in the pyrochlore .The disordering is such that misplacement of eight coordinated B site cation by displacement of A and O' ions to the less symmetry positions. Thus these compounds are known as misplaced-displacive cubic pyrochlores.

In addition to the rich structural chemistry pyrochlores exhibit a remarkable variety of properties including dielectric materials, catalysts [Zhang H *et al* 2008], solid electrolytes, magnetic materials [Zouari S *et al* 2009], actinide host phases for nuclear waste encapsulation [Boccaccini A.R *et al* 2004] etc. Since pyrochlore has wide spread applications, the literature review with respect to semiconducting oxides is given within the scope of this thesis.

Many of the semiconducting pyrochlore oxides have been studied for their ability to split water for hydrogen production [Paulauskas I E *et al* 2008]. In addition to that pyrochlore semiconducting oxides have been proved to be good photocatalyst for the decomposition of organic dye and thus for decontamination of water [Malato S *et al* 2004]. Reduced niobates with a pyrochlore structure $CaLaNb_2O_7$ have been studied for their semiconducting properties. Semiconducting to metallic behiour has been reported for rare earth molybdenum pyrochlores $Ln_2Mo_2O_9$ (Ln=Sm-Yb,Y) [Shi F.N *et al* 1995].

1.5 Powellite

Alkaline earth tungstates, molybdates and vanadates are found to be in ABO_4 type compounds (A=Ca, Ba, Sr, Bi.......),(B=V, Mo, W..........). Structurally these compounds exist in several forms such as scheelite, powellite, wolframite, fergusonite etc. Sheelite - powellite series ($CaWO_4$ – $CaMoO_4$) constitutes an interesting example of anionic substitution. Both end members crystallizes in the same space group ($I4_1/a$) and are isostructural. The unit cell parameter a(=b) in both scheelite and powellite, c is larger in powellite and it has been observed that the c/a ratio is usually significantly larger for molybdates than for tungstates in scheelite type compounds.

Powellite type ABO_4 compounds with eight coordinated A cations and tetrahedral B cations are commonly binary oxides in both natural and synthetic systems. The crystal structure of ABO_4 can be explained by the AO_8 polyhedra and BO_4 tetrahedra as the building blocks. The AO_8 polyhedra share four of its edges with four other AO_8 polyhedra extending in the c-directions. Each oxygen atom of the AO_8 polyhedra is connected to one B cations. Thus, each oxygen atom is coordinated with two of A and one B cations. A typical three-dimensional representation of ABO_4 unit cell is shown in Fig.1.3. In other words, a cubic close packing of A^{2+} and BO_4 tetrahedral units in an ordered manner can explain the powellite structure. This versatile structure allows a

variety of A and B cations with 1+, 2+, 3+, 4+ valency and 5+, 6+ valency respectively to be accommodated [Robert M. Hazen 1985].The only condition is that the A and B cations should be capable of eight fold and tetrahedral coordination respectively.
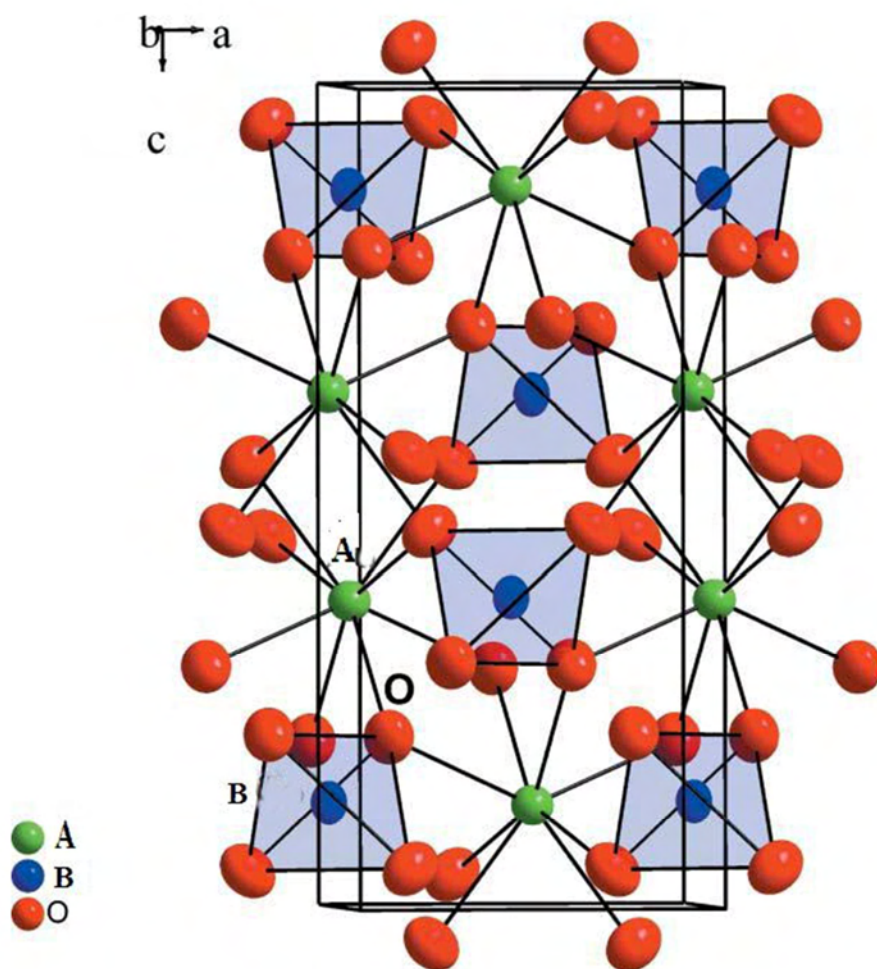
Fig.1.4 Unit cell of powellite. Green spheres represent A^{2+} cations, blue B^{4+} and red O^{2-}.

Tungstates and molybdates having powellite or scheelite structure are found to be very interesting due to their structural, electronic, and catalytic

27

properties. Because of their exceptional properties, they are found to have potential applications in various fields, such as photoluminescence, hosts for lanthanide activated lasers etc. Many of the electrical properties of the tungstates and molybdates have been reported; such as semiconductor to metal transition in $Ln_2Mo_2O_9$ compounds [Shi F. N *et al* 1995], ionic conductivity studies of $BiVO_4$ [Lu. T and Steele. B.C.H 2002] and low TCK dielectrics behavior of Ca-RE-Nb-Mo-Oxides [Nair K.R *et al* 2008].

1.6 Tungsten bronze structure

Tungsten bronzes M_xWO_3 (M = alkali atoms) have long been the subject of investigations for their interesting structural, electronic, and electrochromic properties [Carina Börrnert *et al* 2010; Chi E. O *et al* 2006; Ratnakar R. N and Warren K. C *et al* 1986]. These materials crystallize into variety of structures including perovskite tungsten bronze, [Grenthe C *et al* 2002; Filonenko V.P *et al* 2002] tetragonal tungsten bronze (TTB) [Jamieson P. B. *et al* 1968], hexagonal tungsten bronze (HTB) [Hussain A and Kihlborg L 1976], and intergrowth tungsten bronze (ITB) [Kihlborg L *et al* 2001]. Most of the earlier studies have concentrated on the tetragonal tungsten bronzes. The word ''bronze'' has been applied to non-stoichiometric crystalline transitional metal oxide, especially those ternary systems.

A1 SITE   A2 SITE   B1 SITE   B2 SITE   C SITE
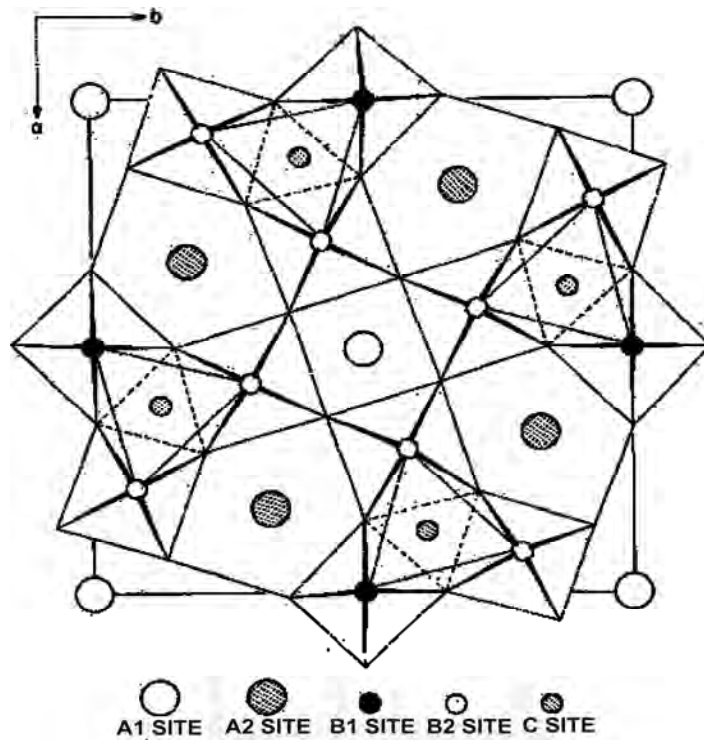
Fig.1.5 Tetragonal tungsten – bronze structure

The tetragonal tungsten–bronze type structure can be considered as a derivative of the classical perovskite structure. They can formally be derived from perovskite structure by rotation of fourfold group of chains of MO_6 octahedra through 45° about the *c* axis (001) so that four-fifths of the square perovskite tunnels are replaced alternately by triangular and pentagonal tunnels. The open nature of the structure as compared to the perovskite allows a wide range of cation and anion substitutions without loss of ferroelectricity.

The crystal structure of the TTB phase is shown in Fig. 1.4 [Abrahams S. C *et al* 1979].

The crystal structure of TTB-phase was first described by A. Magneli in 1949. The tetragonal tungsten bronze (TTB) is built up of a corner shared niobium/tantalum – oxygen octahedra network with three different types of channels in the structure. It can be described by the general formula $(A_1)_2(A_2)_4C_4Nb_{10}O_{30}$ where A_1, A_2 and C are the notations of the different sites in the crystal structure (1). Cations in the A_1 cavities have cubooctahedral coordination by oxygen atoms while in A_2 and C cavities they have a pentacapped pentagonal prismatic coordination and tricapped trigonal prismatic coordination, respectively. The size of these cavities decreases in the order $A_2>A_1>C$. In the TTB type compounds alkaline and/or alkaline earth metals are located in the A and B sites while in the C site small cations.

The tungsten–bronze structure has a general chemical formula $[(A_1)_2(A_2)_4(C)_4][(B_1)_2(B_2)_8]O_{30}$. This crystal structure has three types of tunnels along the *c*-axis. Each unit cell contains ten BO_6 octahedra (B =Nb, Ta, W etc.) which means that there are 4 triangular, 4 pentagonal and 2 square tunnel sites available. Two kinds of A sites, A_1 and A_2 are observed in TTB structure, in which the A_1 site is similar to that in perovskite-type structure [Wakiya N *et al* 1999]. Cations occupying the square perovskite type tunnel sites (A_1 sites) are

30

coordinated by 12 oxygen atoms and have 10 other cations within 400 pm. This site must be able to accommodate oxide coordination numbers greater than nine and is therefore usually filled in by large alkali, alkaline earth or Pb cations. The tolerance factor of this site is given by the equation

$$t_{A_1} = \frac{(r_{A_1} + r_o)}{\sqrt{2}(r_B + r_o)} \qquad (1.4)$$

where r_{A1}, r_B, r_o are the ionic radii of A_1 and B site ions and O^{2-} respectively.

The cations in A_2 occupy pentagonal site and their coordination number is 15. The tolerance factor is given by

$$t_{A_2} = \frac{(r_{A_2} + r_o)}{\sqrt{23 - 12\sqrt{3}}(r_B + r_o)} \qquad (1.5)$$

where r_{A2}, r_B, r_o are the ionic radii of A_2 and B site ions and O^{2-} respectively.

The B site is in octahedral coordination environment. This site is usually occupied by transition metal ions. The C site, which is a narrow tunnel, allows only small cations, such as Li ions, to occupy this site. Since the smallest interstitial C site is usually empty, the general formula for filled tungsten–bronze structure can be $A_6B_{10}O_{30}$. Taking into account the TTB structure, a wide variety of cations substitution is possible due to the presence of several interstices called A, B and C, respectively [Slater P.R *et al*1999; Tatsumi K *et*

al 1997; Tribotte B *et al* 1999]. Thus, the TTB having a very rich structure is capable of exhibiting a large number of interesting properties as a consequence of their non centro-symmetry, which include second harmonic generation (SHG), pyro electricity and piezo electricity. The present study includes the semiconducting properties of TTB structured compounds.

As discussed above, the tetragonal tungsten–bronze compounds show diversity in their properties. Also, numerous compounds are possible due to the different interstitial positions present in their structure. Intensive research has been carried out in tetragonal tungsten–bronze based compound for the search of novel physical properties. It is reasonable to discuss some of the recent works in this area, as the work presented in this thesis, is associated to this field. The electrical properties of $Sr_6Nb_{10}O_{30}$ have been studied in the temperature range of 10-300K by Y. Kown et al and it has been reported as a semiconductor [Kown Y *et al* 1997]. A new series of tungsten bronzes in B_xWO_3 ($0.01 \leq x \leq 0.08$) were synthesized by hybrid microwave method and has been reported by Juan Guo *et al* [Guo J *et al* 2007]. Resistivity measurement indicates that $Na_{0.56}WO_3$ shows a change from metallic to anomalous semiconducting behavior accompanied by phase transformation from tetragonal to cubic phase [Fan R *et al* 2000].

1.7 Scope of the present work

Preparation of high temperature NTC thermistors with unique characteristics is an interesting area of recent research. A new class of seminconducting ceramics has been synthesized by exploiting the variable valency of Cerium (Ce). The semiconducting nature of the compound is due to the conversion of Ce^{4+} to Ce^{3+} in the lattice to maintain the oxygen stoichiometry in the structure. In the present investigation, three different crystal families: pyrochlore, powellite and tetragonal tungsten bronze have been selected, on the basis of the technological importance of these structures. Various cations like Tantalum or Niobium, Molybdenum or Tungsten are substituted at the B site of these structures to observe how these substitutions affect their structure and properties. A detailed study of the structure, microstructure and properties of these newly prepared compounds has been carried out and efforts have been made to correlate the results of different investigations. In addition to the preparation of semiconducting ceramic materials with interesting properties, attempts have been made to characterize them for thermistor applications.

CHAPTER 2

METHODS OF PREPARATION AND CHARACTERIZATION

2.1 Introduction

In most cases the fabrication process starts from a mass of powder obtained from commercial sources. Nevertheless, knowledge of powder synthesis methods is very important. Equally important are methods that can be used to determine the physical, chemical and surface characteristics of the powder. The characteristics of the powder depends strongly on the method used to syntheses it and, these in turn influence the subsequent processing of the ceramic. The powder characteristics of great interest are the size, size distribution, shape, degree of agglomeration, chemical composition and purity [Rahaman M N 2003]. Many methods are available for the synthesis of ceramic powders, these ranges from mechanical methods involving predominantly grinding or milling for the reduction in size of a coarse, granular material to the chemical methods involving chemical reactions under carefully controlled conditions.

Most widely used methods for the fabrication of ceramics from powders are melt casting and firing. These two routes are actually very old techniques used by even the earliest civilization. Melt casting technique is usually limited to glass fabrication, due to uncontrolled grain growth and other undesired features such as low mechanical strength etc. However, by adopting glass

ceramic route one can improve the properties of glass ceramics. For the production of polycrystalline ceramics firing method is used.

It is necessary to understand the fundamental mechanisms, which take place during different steps of the process to obtain reliable and desirable properties of the final parts. Several methods can be divided into three categories (a) Mechanical methods (b) solid state reaction methods and (c) chemical methods [Seagal D 1991].

Ceramic powder synthesis by mechanical method involve grinding, milling for the reduction in size of a coarse granular material (comminution). Chemical methods include chemical reactions at controlled conditions. Preparation of fine powders is beneficial as it will give high density ceramics at low firing temperatures [Zhou Y. C *et al* 1993; Pierre E. D *et al* 1985; Brook R. J *et al* 1990]. As the size of the powder is decreased to 1 µm, the particles have greater tendency to form agglomerates which result in non-uniform packing. Nearly all production processes of ceramic parts include a sintering step at a high temperature, which influences overall material properties [Cheremisinoff N. P 1990].

2.2 Solid state route for ceramics synthesis

This is one of the easiest and oldest techniques used for the preparation of ceramic materials. The conventional ceramic synthesis can be depicted by the following flow chart.

Raw material
↓
Mixing and Drying
↓
Calcination
↓
Forming
↓
Sintering
↓
Finishing
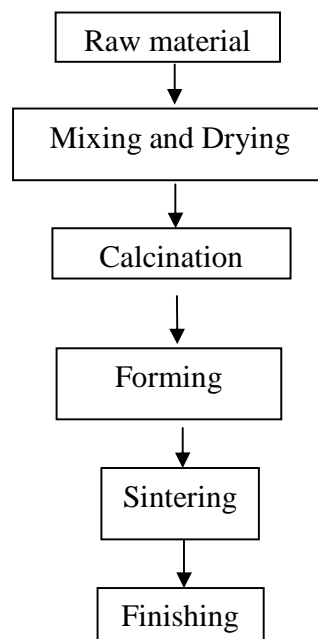
Fig. 2.1 Flow chart for different stages of general ceramic processing.

It involves mainly three steps (i) thorough mixing of the stoichiometric oxides (ii) high temperature treatment (iii) finishing. Chemical reactions in powder are quite complicated. High temperature heating results in the production of new materials at the expense of free energy, at the points of contact through solid state diffusion. Eventually this product layer acts like a potential barrier between two grains and thus hindering further grain to grain material transport. This demands the need of new points of contact to be

introduced which is usually achieved through grinding or ball milling. This frequent grinding followed by calcinations maximizes the product to reactant ratio.

When the rate of product formation is controlled by diffusion through product layer, the product thickness is observed to follow a parabolic growth law given by the equation

$$X^2 = Kt \qquad\qquad (2.1)$$

where K is a rate constant that obeys Arrhenius relation and t the duration of heat treatment.

| Powder | Partially reacted | Fully reacted |
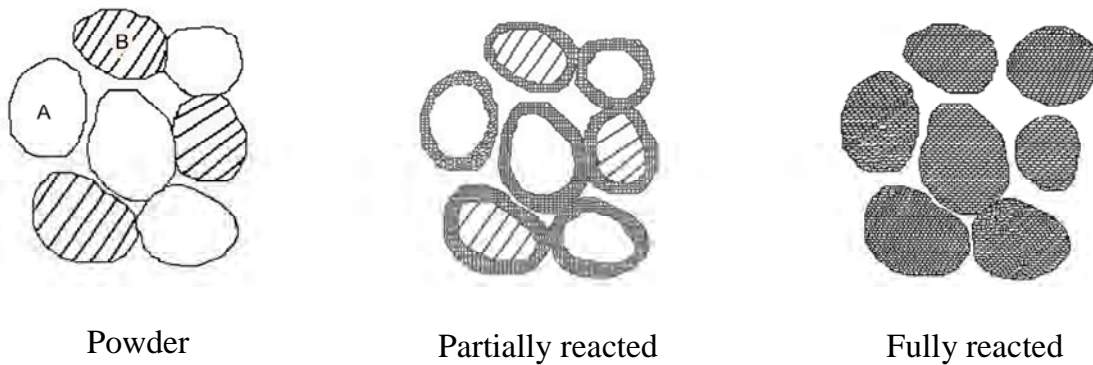
Fig.2.2. Reaction between two particles to form a product at the points of contact.

The volume of unreacted material at a time t is given by

$$V = 4/3\ \pi(r\text{-}y)^3 \qquad\qquad (2.2)$$

where r is the initial radius of the reactant and y is the thickness of the reaction layer.

In terms of α - the portion of reactant already reacted, the above equation can also be written as

$$V = 4/3 \ \pi r^3 \ (1-\alpha) \qquad (2.3)$$

Comparing the two equations

$$y = r \ [1-(1-\alpha)]^{1/3} \qquad (2.4)$$

Assuming that y grows according to parabolic relationship given by the above equation

$$[1-(1-\alpha)^{1/3}]^2 = Kt/r^2 \qquad (2.5)$$

Which is known as Jander equation for isothermal reaction [Rahaman M N 2003]. The reactant particles are schematically illustrated to emphasize the fact that no matter what the particle size is; each reactant particle contains only one type of cation. The severe reaction conditions are necessary to obtain single phase product because of diffusional limitations of the solid state reactions. Initial reaction is rapid but further reaction goes slower and slower as the product layer builds up and diffusion paths become longer.

The different steps used for ceramic synthesis and characterization techniques used are described in the following sections.

2.2.1 Selection and weighing of raw materials

The highly purified (99.99%) materials for synthesis (reactants) are selected depending upon the composition. Stoichiometric amounts of the constituent oxides are calculated. Raw materials are weighed accordingly using an electronic balance with accuracy up to four decimal places.

2.2.2 Mixing and drying

The stoichiometrically weighed reactants are mixed together in an agate mortar with aceton as the mixing medium. After mixing the powder is kept in a hot air oven at 100°C for 30 min. This process is repeated 3 times so as to get a homogeneous, finely powdered mixture. For solid state diffusion mechanism, the growth of the reaction product in powder system occurs at the contact points. The homogeneity of mixing is one of the most important factors which decide the ability of a process to produce homogeneous, single phase powder. The size and distribution of the reactant particles are important factors for deciding the degree of homogeneity. A homogeneous mixture has great influence on the diffusion distances and the number of contacts between the reactant particles. The presence of agglomerates results in porosity of the final product. Therefore, it is necessary to mix the reactants to a high level and to powder them repeatedly. During mixing process these agglomerates get broken

and defects are introduced into the grains which enhance the diffusion mechanism.

2.2.3 Calcination

Calcination involves heat treating a powder or mixture of powders at a temperature well below its melting point to effect decomposition, that is , to liberate unwanted gases and/or chemically bound waste, solid state reactions and structural transformations to produce the desired composition and phase product.

There are different heating stages in the preparation of ceramics through solid state route. Calcination is an intermediate heating at a lower temperature through which chemical reactions between solid starting materials, usually in the form of mixed powders, take place. The reactants normally consist of oxides, carbonates, nitrates, sulphates etc.

The kinetics of solid state reactions occurring during calcinations may be controlled by any one of the three processes: (i) the reaction at the interface between the reactant and solid product (ii) heat transfer to the reaction surface (iii) gas diffusion or permeation from the reaction surface through the porous product layer. The calcination conditions such as temperature, duration of heating and atmosphere are important factors controlling shrinkage during

sintering. Though the final phases of interest may not be completely formed, the calcinations yield a consistent product.

2.2.4 Grinding

Grinding prepares the reacted material for ceramic forming. The process by which smaller particles are produced by reducing the size of larger ones by means of crushing, grinding and milling is called comminution. The grinding process has an effective role in deciding the degree of homogeneity. It can be accomplished by different methods. Generally grinding to somewhere around 1 to 10μm is advisable. Grinding the solid reactants to very fine powder (<1 µm) can lead to the formation of agglomerates which result in non-uniform packing. Agate mortar with pestle is used for grinding the powder reactants.

2.2.5 Addition of binder

Binder is added to the powdered samples for making them into the desired shape, usually in the form of small solid cylinders. The addition of binder imparts sufficient strength and elastic properties which helps in the handling and shaping of ceramic powders. To improve the rheological properties of powder ceramics, it is a usual practice to add water soluble organic binders such as polyvinyl alcohol during pressing of ceramic samples. The usually used polymer binders are PVA (Polyvinyl Alcohol), PEG (Polyethylene Glycol) etc. The polymeric dispersions and organic binders

provide the pressed ceramic powders with optimal properties from the point of view of thickening abilities and mechanical strength of pressed samples. The binder concentration for different types of processes is different. In dry processing it is about 3%, in wet processing it is about 3–17% and in plastic forming it is up to 20% [McHale A E 1991]. During heating, these binder materials will burn out since they have low boiling point.

2.2.6 Compaction

Compaction of powder has a vital role in usual ceramic fabrication processes. The packing structure of the green body basically influences the microstructural development during sintering and consequently determines the properties of sintered ceramics. Compaction is defined as the densification process of powders within a closed vessel. The pressure forming cycle consists of four stages, (1) Pouring of the powder into the die cavity (2) compaction (3) decompaction and (4) ejection of compact from die. A large number of ceramics are formed by uniaxial pressing because of its high productivity and suitability for automation. The calcined powder undergoes a limited sintering and hence it is again grounded thoroughly. The resulting powder is mixed well with suitable binder of appropriate amount. This mixture is then again ground using mortar and pestle. This thoroughly mixed powder is transferred to a suitable die and is subjected to compaction by slow uniaxial dry pressing to

ensure the escape of entrapped air. Uniaxial pressing involves the compaction of powder into a rigid die by applying pressure in a single axial direction through a rigid punch or piston.

Samples of 10 mm diameter and 2–3 mm thicknesses are prepared to maintain the aspect ratio so that the pressure distribution is more or less uniform in the powder compacts. A pressure of 150-250MPa is applied for ceramic forming.

2.2.7 Solid state sintering

When thermal energy is applied to a powder compact, the compact is densified and the average grain size is increased. This process is called sintering. It is one of the oldest human technologies, the firing of clay materials. Here the system is heated in the range of 0.5–0.75 of the melting temperature. The powder does not melt but instead the particles join together, resulting in densification of the body due to the atomic diffusion in the solid state. This type of sintering is called solid state sintering. In this stage the green body is heated to produce the desired microstructure. The changes occurring during this stage may fairly complex, depending on the complexity of the starting materials. The driving force in sintering is the reduction in surface free energy of the consolidated mass of particles. This reduction in free energy due to atomic diffusion either results in densification or coarsening. Higher

sintering temperatures are used to promote inter diffusion of the constituents of the powder blend or to attain higher sintered density.

2.2.8 Finishing

This is the final stage of ceramic fabrication. In order to improve surface finish and also to remove surface flaws some kind of final treatment is necessary. This can be achieved through polishing of the surface using emery paper.

2.3 Characterization techniques

Characterization refers to the use of external techniques to probe into the internal structure and properties of a material. Characterization can take the form of actual materials testing, or analysis. Analysis techniques are used simply to magnify the specimen, to visualize its internal structure and to gain knowledge about the distribution of elements within the specimen and their interactions.

2.3.1 X-ray diffraction technique

Numerous analytical techniques are used to characterize these materials. One of these methods, X-ray powder diffraction (XRD), is an instrumental technique that is used to identify crystal structure of minerals, as well as other crystalline materials. One of the main methods to decode the structure of condensed matter on atomic scale is X-ray diffraction. In the electromagnetic

spectrum X-rays are to be found between ultraviolet light and high energy gamma rays. The wavelength range lies between 0.01 and 10 nm and is therefore of the order of distances between molecules and crystal lattice constants. X-rays with wavelengths longer than 1 nm are called soft X-rays, those of shorter wavelengths are considered hard.

One of the phenomena of interaction of X-rays with crystalline matter is its diffraction, produced by the reticular planes that form the atoms of the crystal. A crystal diffracts an X-ray beam passing through it to produce beams at specific angles depending on the X-ray wavelength, the crystal orientation and the structure of the crystal. In the macroscopic version of X-ray diffraction, a certain wavelength of radiation will constructively interfere when partially reflected between surfaces (i.e., the atomic planes) that produce a path difference equal to an integral number of wavelengths. This condition is described by the Bragg law:

$$2d \sin \theta = n\lambda \qquad (2.6)$$

where n is an integer, λ is the wavelength of the radiation, d is the spacing between surfaces and θ is the angle between the radiation and the surfaces. This relation demonstrates that interference effects are observable only when radiation interacts with physical dimensions that are approximately the same size as the wavelength of the radiation [Cullity B. D, 1959]. Since the distances

46

between atoms or ions are of the order of 10-100Å, diffraction methods require radiation in the X-ray region of the electromagnetic spectrum, or beams of electrons or neutrons with similar wavelength. So, through X-ray spectra one can identify and analyze any crystalline matter. In powder X-ray diffraction the powder provides all the possible orientations of the small crystals giving rise to a large number of diffraction cones, each one corresponding to a family of planes satisfying the Bragg's law. For large grains, rings are discontinuous and formed by small spots. As the size of the grains diminishes, the spots are closer and for an optimum size a continuous ring is obtained, which is transferred into a peak when working with graphic registers or lines in a photographic register [Hammond C 2001]. For lower grain sizes, the clarity of rings is lost again and wide peaks or bands appear. When the crystals are not randomly but preferentially oriented the intensity of the different rings and along each ring are not uniform. Perhaps the most routine use of diffraction data is for phase identification. Each crystalline powder gives a unique diffraction diagram, which is the basis for a qualitative analysis by X-ray diffraction. Identification is practically always accompanied by the systematic comparison of the obtained spectrum with a standard one (a pattern), taken from any X-ray powder data file catalogues, published by the American Society for Testing and Materials known as ASTM and the International Centre for Diffraction

Data (ICDD) [Moore D M and Reynolds Jr. R. C 1989]. The diffraction profiles of a mixture of crystalline specimens consist in spectra of each of the individual crystalline substances present, superposed. Moreover, an accurate analysis of phase transitions in materials can also be carried out when analyzing samples treated at different annealing temperatures or even performing in-situ XRD analysis.

2.3.2 Raman spectroscopy

Raman and IR spectroscopy are found to be useful techniques for the structural investigation of materials. The energy of a molecule or ion consists in four components that for a first approximation can be treated separately: the translational energy, the rotational energy, the vibrational energy and the electronic energy. When the molecule is placed in an electromagnetic field, a transfer of energy from the field to the molecule will occur only when the difference in energy between two quantified states equals hν, being h the Planck's constant and ν the frequency of light.

Raman effect is an inelastic scattering process. The scattered photons have frequency shifts (10–4000 cm^{-1}) characteristic of the vibrational or rotational energies of the molecule. A particular vibrational motion of the molecule may produce Raman scattering as well as infrared absorption of radiation. In such cases same information is obtained from both methods. But,

in the case of molecules possessing centre of symmetry, the Raman active vibrations are infrared inactive and vice versa. The vibrations which are symmetric with respect to centre of symmetry are IR inactive, since there is no change in the dipole moment. However, these vibrations are Raman active since they produce a change in polarizability. The vibrations which are antisymmetric with respect to centre of symmetry are IR active as it can produce a change in dipole moment. These vibrations will be Raman inactive [Long D. A 1977].

2.3.3 Scanning electron microscopy

The scanning electron microscope (SEM) is a type of electron microscope capable of producing high-resolution images of a sample surface. It is primarily used for the study of surface morphology of solid specimens, which gives image at very high magnification and high resolution. Due to the manner in which the image is created, SEM images have a characteristic three-dimensional appearance and are useful for judging the surface structure of the sample.

The resolution of the SEM image depends on the quality of the optical system that forms the electron beam including the nature of the electron source. SEM's can typically resolve objects as small as 10nm. The magnification of SEM is not directly related to optical system, unlike a light

microscope is related to the ratio between the size of the scan of the object compared to the size of the scan on the image display. It has a large depth of field enabling to have more of a specimen to be in a focus at one time.

The SEM consists of three basic units. The electron optical column, the vacuum system and the signal detectors and display system. The primary function of the lenses is to demagnify the electron beam. The vacuum system consists of two pump systems. Scan generators control the magnifications. The electron beam commonly used in SEM is accelerated through a voltage of about 1-50KeV.

Non-conductive solid specimens should be coated with a layer of conductive material, except when observed with Variable Vacuum or Environmental SEM. Such coatings are made on the surface of non-conductive samples using gold or palladium [Goldstein J. I *et al* 1981].

2.3.4 Energy dispersive X-ray spectroscopy

Energy dispersive X-ray spectroscopy (EDS or EDX) is an analytical technique used in conjunction with Scanning Electron Microscopy (SEM), predominantly for the elemental analysis or micro chemical characterization of a specimen. The interaction of electron beam with specimen produces a variety of signals such as secondary electrons, backscattered electrons, auger electrons, X-rays etc. X-ray signals are typically produced when a primary

beam of electrons causes ejection of inner shell electrons from the sample. An outer shell electron takes its place and gives off an X-ray signal whose energy can be related to its nuclear mass and the difference in energies of the electron orbit involved. The X-ray released by the electron is then detected and analyzed by the energy dispersive spectrometer and they are characteristic of the difference in energy between the two shells and of the atomic structure of the element from which they were emitted. In EDS the X-rays are arranged in a spectrum by their energy and most commonly from low atomic number (low energy) to high atomic number (high energy). The energies of which are unique for each element [Severin K. P 2004].

The characteristic X-rays produced are detected using a Si-Li detector, which is working at liquid nitrogen temperature. The energy of the detected X-ray is compared with the energy of scale in the system and produce characteristic peaks at different energy levels according to the elements present. The area under the peak gives information about the amount of each element present in the sample [Goodhew P J *et al* 2001]

EDS is multi-elemental and non destructive and can be applied to large as well as small samples of different compositions and character. Quantitative analysis is possible for all elements with atomic numbers greater than that of beryllium (Be). This can be a powerful tool for detecting the presence of a

contaminant (impurity) in the sample as well as determining the chemical composition of the sample.

2.3.5 X-ray photoelectron spectroscopy (XPS)

In an XPS analysis, the sample is irradiated with electromagnetic radiation of energy hν and it emits electrons because of the photoelectric effect. These electrons have kinetic energy of the form:

$$K.E = h\nu - E_B \qquad (2.7)$$

where E_B is the bond energy of the electron.

The incident radiation has energy greater than 1KeV and then the electrons come from the inner levels. The most usual source of X-rays is a sample of Mg or Al. In it, electrons from a cathode produce ionization of the inner levels of this element and then X-rays are emitted.

An XPS spectrum is obtained as a plot of the number of detected electrons per energy interval versus their kinetic energy and the minimum width of the lines comes from the uncertainty in the radiation energy. In order to have a reproducible analysis, the bond energies must have a reference. In gas phase the bond energy is the energy that an electron in the vacuum must receive to reach the zero potential without kinetic energy. In solids, the bond energy is the energy that we must supply to an electron to reach the Fermi level.

To have a good calibration of the lines, in metals $E_B = 0$ in the Fermi level and this is the level with K.E greater in the XPS spectrum. The bond energy is proportional to Z^2 so that the measure of E_B allows the identification of the materials. Further, the XPS analysis can identify atoms of the same element with different bonds. The reason is that when the other atoms are more electronegative, the measured E_B is greater because other atom loses part of its negative charge and the internal electrons are more attracted by the core. This produces a chemical shift in the line that allows the identification of this different bonding of the element.

In order to find out the concentration of an element, the areas of the lines are compared. When overlapping occurs, a deconvolution must be made. In this process each contribution receives a Gaussian or Lorentzian form. Another important characteristic of this analysis is that the area scanned is of the order of hundreds of μm^2, very large when compared with those from other techniques. Moreover, the technique induces some damage to the sample, overheating the analyzed zone and destroying the local crystal structure.

2.3.6 Impedance spectroscopy

The Complex Impedance Spectroscopy is a powerful technique to characterize many electrical properties of materials. It is useful to evaluate and separate the contribution of the overall electrical properties in the frequency

domain due to electrode reactions at the electrode/sample interface and migration of ions through the grains and across the grain boundaries in a polycrystalline material.

In order to conduct the impedance analysis the circular flat faces of the sintered pellets are painted with ultra fine and high quality silver paste for good electrical contact prior to the measurement. Then the samples were electroded using silver leads. After electroding the samples are cured in an oven to remove moisture and other volatile substances.

It is a non-destructive experimental technique for the characterization of electrical properties of some electronic materials. The technique is based on analyzing the ac response of a system to a sinusoidal perturbation and subsequent calculation of impedance as a function of the frequency of the perturbation. The analysis of the electrical properties (conductivity, dielectric constant/loss, etc.) carried out using relaxation frequency (ω_{max}) values gives unambiguous results when compared with those obtained at arbitrarily selected fixed frequencies. The frequency dependent properties of a material can be described as complex permittivity (ε^*), complex impedance (Z^*), complex admittance (Y^*), complex electric modulus (M^*) and dielectric loss or dissipation factor (tan δ) [Barsoukov and Macdonald 1987]. The real

(ε', Z', Y', M') and imaginary (ε'', Z',Y", M") parts of the complex parameters are in turn related to one another as follows:

$$\varepsilon^* = \varepsilon' - j\varepsilon'' \tag{2.8}$$

$$\varepsilon' = -\frac{Z''}{\omega C_0 \left[(Z')^2 + (Z'')^2\right]} \tag{2.9}$$

$$\varepsilon'' = \frac{Z'}{\omega C_0 \left[(Z')^2 + (Z'')^2\right]} \tag{2.10}$$

$$M^* = M' + jM'' = 1/\varepsilon^* = j\omega\varepsilon_0 Z^* \tag{2.11}$$

$$Z^* = Z' - jZ'' = \frac{1}{jC_0\omega\varepsilon^*} \tag{2.12}$$

$$Y^* = Y' + jY'' = j\omega C_0\varepsilon^* \tag{2.13}$$

$$\tan\delta = \frac{\varepsilon''}{\varepsilon'} = \frac{M''}{M'} = \frac{Z'}{Z''} = \frac{Y'}{Y''} \tag{2.14}$$

The Nyquist plot is one popular format for evaluating electrochemical impedance data. This format is also known as a Cole–Cole plot or a complex impedance plane plot. The Nyquist plot has several advantages. The primary one is that the plot format makes it easy to see the effects of the ohmic resistance. If you take data at sufficiently high frequencies, it is easy to extrapolate the semicircle toward the left, down to the X axis to read the ohmic

resistance. The shape of the curve (often a semi-circle) does not change when the ohmic resistance changes. Consequently, it is possible to compare the results of two separate experiments that differ only in the position of the reference electrode [Holze R 2008].

2.3.7 Conductivity measurements

Two probe method is one of the standard and most commonly used methods for the resistivity measurement of very high resistivity (near insulators) samples.

The conductivity of the sample is given by

$$\sigma = \ell \, / \, RA \qquad\qquad (2.15)$$

Where ℓ is the thickness of the pellet

R is the measured resistance at temperature T

A is the area of cross section of the pellet.

In order to measure the electrical conductivity, the pellets were coated with a high-temperature silver paste and cured at 600°C for 30 min and silver wires were attached to electroded surfaces. The conductivity was measured in a temperature range of 30 – 600°C using a high resolution PM 2525 Philips digital multimeter. The resistance readings were recorded with slow heating after equilibrating the pellet for 2 min at each measuring temperature. The

aging coefficient was measured by the relative $\Delta R/R$ of the pellets held at

500°C in air for different periods of time up to 500 h.

CHAPTER 3

STRUCTURE AND ELECTRICAL PROPERTIES OF NONSTOICHIOMETRIC SEMICONDUCTING PYROCHLORES IN Ca– Ce – Ti – Nb – O SYSTEM

3.1 Introduction

Oxides of the pyrochlore family have a general formula, $A_2B_2O_7$ and among the ceramic materials they are an important class of materials both from the fundamental and technological point of view. A wide variety of compounds are reported with this structure having a variety of properties such as semiconductivity, dielectric, photocatalyst, sensor etc [Prabhakar Rao P *et al* 2004; Su W.F and Lu Y.T *et al* 2003; Luan J *et al* 2007; Kosacki I *et al* 1995]. This versatile structure allows a variety of A and B cations with 2+, 3+ valency and 4+, 5+ valency respectively to be accommodated. The conditions are that the A and B cations should be capable of 8 fold and 6 fold coordination respectively and the ionic radius ratio of A cation to B cation should lie within the range of 1.46 to 1.8 [Subrahmanian M A *et al* 1983].

Furthermore, misplaced displacive pyrochlores are a point of interest since most of its property arises from the structural specialty of the compound rather than the elemental constitution [Nguyen B *et al* 2008]. Displacive pyrochlores had been subject of controversy for a long time since it was very difficult to accept the fact that small cations like Zn^{2+}, Ti^{4+}, etc can occupy the bigger A site of the pyrochlore; Bi-Zn-Nb-O system fall under this category [Matjazvalant *et al* 2007]. Very recently Ca containing ternary pyrochlores are also reported with Ti in the A site causing displacive disorder in the system [Nguyen B *et al* 2008; Roth R S *et*

al 2008]. It has also been observed that the radius ratio of pyrochlores precludes the formation of rare earth titanate ($Ln_2Ti_2O_7$) cubic pyrochlores for Ln =La to Nd. Especially in the case of Ce containing pyrochlores pure phase formation is observed to be very difficult [Machida M *et al* 2000]. To tailor the properties of pyrochlores and to enhance their application functionality, it is desirable to understand their nonstoichiometry in a consistent manner.

Complex impedance spectroscopy (CIS) has been considered as a powerful non-destructive technique in describing the electrical processes occurring in a system on applying an ac signal as input perturbation. The output response, when plotted in a complex plane plot, appears in the form of a succession of semicircles representing electrical phenomena due to bulk material, grain boundary effect and interfacial phenomena if any. In view of this specialty, CIS makes it possible to separate the contribution due to different components in a polycrystalline sample, that of course have different time constants, in the frequency domain [Sen S and Choudhary R.N.P *et al* 2004]. Impedance relaxation frequency and hence relaxation time (τ) is a parameter that depends on the intrinsic properties of the material and not on the sample geometrical factors. The term intrinsic properties of the material refer to the properties attributed to structure/microstructure. These properties govern the distribution of resistive and capacitive components in the material on which relaxation

time ultimately depends in accordance with the relation. So, the results obtained using impedance analysis is basically unambiguous and provide true picture of the sample electrical behavior. This aspect motivated us to take up this study on these compounds.

In the present study, a series of nonstoichiometric compositions having the formula, $CaCe_xTiNbO_{7-\delta}$ (x = 0.5, 0.6, 0.7, 0.8, 0.9, 1) is prepared to investigate the extent of tolerance of the nonstoichimetry at the A site to get a phase pure pyrochlore type oxide. Here in this study it has been attempted to vary the concentration of Ce and analyzed the effect of Ce concentration on the structure, microstructure and electrical properties of these compositions. The conductivity phenomenon of these compounds as a function of temperature and frequency has been studied using impedance spectroscopy.

3.2 Experimental

The polycrystalline samples with varying Ce content having the general formula, $CaCe_xTiNbO_{7-\delta}$ (x = 0.5, 0.6, 0.7, 0.8, 0.9, 1) were synthesized by the conventional solid state route. Stoichiometric amounts of $CaCO_3$, CeO_2, TiO_2, and Nb_2O_5 were taken as the starting raw materials (All chemicals of 99.9% purity are supplied by M/s Acros). In sequence these oxides were rigorously mixed using an agate mortar with acetone as the mixing medium. The mixing was repeated thrice in order to get a homogeneous mixture. Crystalline powders were prepared by calcinations

of precursor at 1300°C for 3h. The calcinations were repeated with intermittent grinding. The calcined powders were then made into cylindrical pellets of 10 mm diameter and 2 mm thickness by isostatic pressing at a pressure of 250 MPa. 4 wt. % of polyvinyl alcohol (PVA) in distilled water served as an organic binder for compacting the pellets. The pellets were preheated at 600°C to remove PVA and then the temperature was increased to 1350°C for 9 h.

The crystal structure of the samples was identified by powder X-ray diffraction analysis with Ni filtered CuKα radiation using a Phillips X'pert Pro Diffractometer. The X-ray photoelectron spectroscopy (XPS) analysis was performed on the pellets in an ultrahigh vacuum using PHI Versa Probe Scanning XPS Microprobe with monochromatic X-ray source of Al Kα (hv = 1486.6 eV). In order to measure the electrical conductivity, the pellets were coated with high temperature silver paste and then were electroded with silver wires. The microstructure and microchemical analysis of the samples were recorded on the thermally etched pellets by a scanning electron microscope (SEM) of JEOL make JSM 5600LV and energy dispersive spectrometer coupled with the SEM. The impedance response of these pellets was studied over the frequency range 10Hz-1MHz in the temperature range 30-600°C using the impedance analyzer (Solartron, SI 1260). The electrical conductivity was measured in a temperature range of

50 to 600 °C using a high resolution digital multimeter of Philips make PM 2525.

3.3 Results and Discussion

3.3.1 Powder X-ray diffraction analysis

Fig. 3.1 shows the powder XRD patterns of $CaCe_xTiNbO_{7-\delta}$ (x = 0.5, 0.6, 0.7, 0.8, 0.9, 1). The characteristic peaks observed in the patterns are indexed according to the cubic pyrochlore structure with space group $Fd3m$ and Z = 8. As can be seen from the patterns, a single phase is obtained only for the $CaCe_{0.7}TiNbO_{6.55}$ composition. A secondary phase of Nb_2O_5 with minor amount of Ca, Ce and Ti (marked as arrows in Fig. 3.1) is observed for the compositions with less Ce content: $CaCe_{0.5}TiNbO_{6.25}$ and $CaCe_{0.6}TiNbO_{6.4}$. Presence of a Ce rich secondary phase is seen in $CaCe_{0.8}TiNbO_{6.7}$, $CaCe_{0.9}TiNbO_{6.85}$ and $CaCeTiNbO_7$ compositions. This secondary phase is marked by squares in Fig. 3.1. The phase stability of $A_2B_2O_7$ ordered pyrochlores is determined by the ionic radius ratio, (r_A/r_B) (average ionic size of the cations at A site to that at B site) and this cationic radius ratio lies between 1.46 and 1.78 under ambient conditions [Subrahmanian M A *et al* 1983]. In the present system, this ratio varies from 1.809 to 1.815 (Table 3.1) indicating outside the scope for pyrochlore structure formation in the present system. The ionic radii of Ca^{2+} and Ce^{3+}, in 8-fold coordination are 1.12 Å and 1.143 Å and that of Ti^{4+} and Nb^{5+} in 6-fold coordination are 0.6014 Å and 0.64 Å respectively [Shannon R.D *et*

al 1976]. However, it is observed from the XRD patterns that $CaCe_{0.7}TiNbO_{6.55}$ has a cubic pyrochlore structure without any secondary phases.
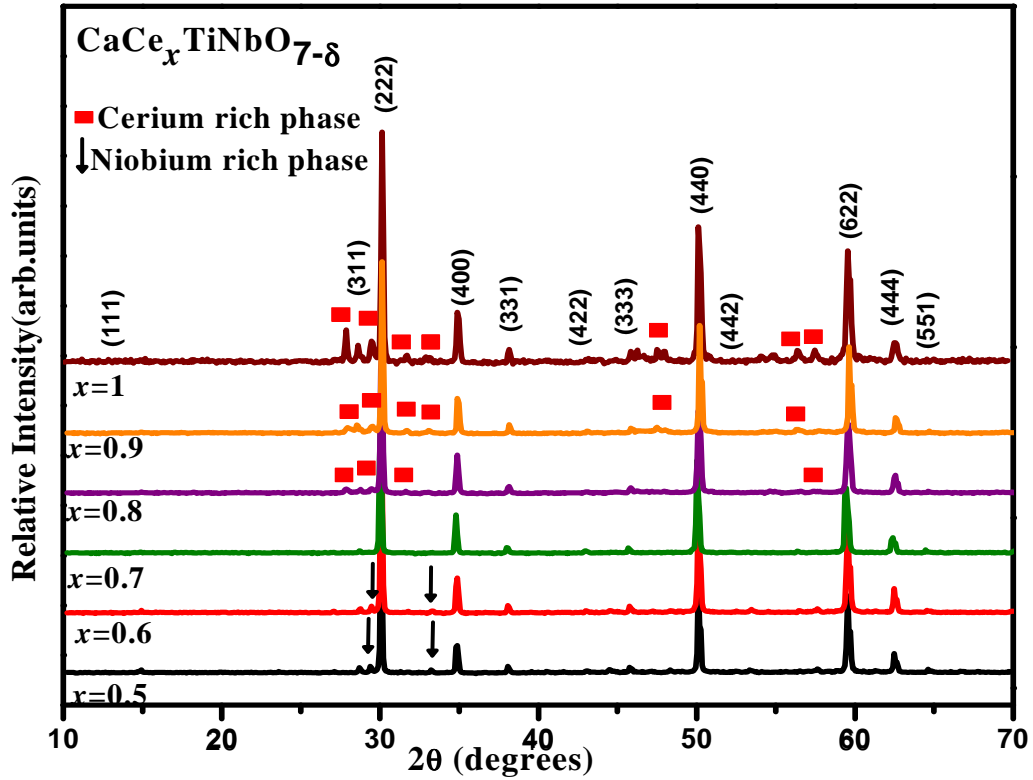
Fig. 3.1 Powder X-ray diffraction patterns for various compounds in $CaCe_xTiNbO_{7-\delta}$ (*x*=0.5 to 1) system

But, recent studies on the pyrochlores in $(Ca_{1.5}Ti_{0.5})(NbTi)O_7$ [Roth R.S *et al* 2008] and $CaO-TiO_2-(Nb,Ta)_2O_5$ [Vanderah T.A *et al* 2006] indicated that Ti^{4+} ions (up to 25% of the large A-site cations) mixes up with the much larger Ca^{2+} ions on the A-sites by displacing from the ideal 8-coordinated position to achieve satisfactory coordination environment. The XRD patterns of such pyrochlores are characterized by (442) reflection, forbidden for an ideal pyrochlore and required lower symmetry positions

for the A and O' ions. Such pyrochlores are termed as misplaced displacive cubic pyrochlores.
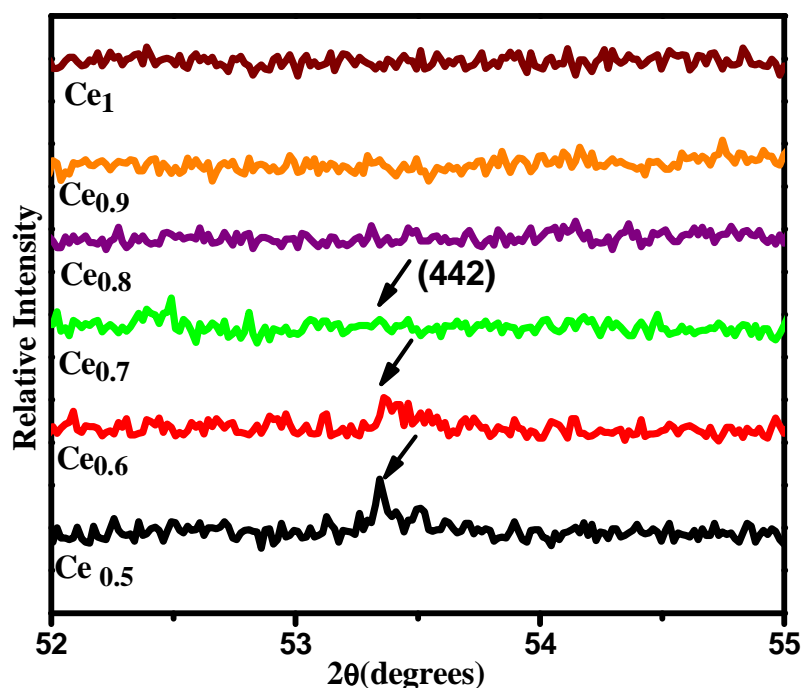
Fig. 3.2 The selected region of X-ray powder diffraction pattern showing weak pyrochlore forbidden (442) reflection,

Very weak reflections of (442) /(006) at a 2θ value of $53°$ observed in the XRD patterns of $CaCe_{0.5}TiNbO_{6.25}$, $CaCe_{0.6}TiNbO_{6.4}$ and $CaCe_{0.7}TiNbO_{6.55}$. These are the forbidden reflections of the cubic pyrochlore structure indicating the displacive disorder in the $O'A_2$ substructure [Nguyen B *et al* 2007] and is shown in Fig. 3.2. These results suggest that some amount of Ti might be occupying the A sites (mixing up with Ca and Ce cations) in order to stabilize in phase pure pyrochlore type structure. It is also observed that as the Ti content in the A site increases, the intensity of (442) reflection becomes more visible indicating

misplacement of more of 8 coordinated B site Ti in the A site by displacement of A and O' ions to the less symmetry positions. For a better understanding, the compositions are rewritten in the pyrochlore formula by displacing some Ti atoms from B site as indicated in Table 3.1. Thus these compounds can be considered as misplaced-displacive cubic pyrochlores.

Composition	$A_2B_2O_7$ based formula	Lattice parameter (Å)	A/B ratio	Activation energy (eV)
$CaCe_{0.5}TiNbO_{6.25}$	$(CaCe_{0.5}Ti_{0.25})(Ti_{0.75}Nb)O_{6.25}$	10.2774(5)	1.809	0.75
$CaCe_{0.6}TiNbO_{6.4}$	$(CaCe_{0.6}Ti_{0.2})(Ti_{0.8}Nb)O_{6.4}$	10.2871(5)	1.811	0.66
$CaCe_{0.7}TiNbO_{6.55}$	$(CaCe_{0.7}Ti_{0.15})(Ti_{0.85})NbO_{6.55}$	10.3098(1)	1.812	0.63
$CaCe_{0.8}TiNbO_{6.7}$	$(CaCe_{0.8}Ti_{0.1})(Ti_{0.9}Nb)O_{6.7}$	10.2806(5)	1.813	0.52
$CaCe_{0.9}TiNbO_{6.85}$	$(CaCe_{0.9}Ti_{0.05})(Ti_{0.95}Nb)O_{6.85}$	10.2810(7)	1.814	0.55
$CaCeTiNbO_7$	$CaCeTiNbO_7$	10.3046(2)	1.815	0.51

Table. 3.1 Lattice parameter, A/B ratio and electrical conductivity data for various compositions in Ca – Ce – Ti – Nb – O system.

The lattice parameter '*a*' is obtained from the least square method and is given in Table 3.1. It can be noticed from these values that the lattice parameter increases on incorporation of more cerium content till a phase pure compound is obtained in Ca – Ce – Ti – Nb – O system. Based on the

relative ionic size considerations of Ce^{3+} (CN (VIII) = 1.143 Å), one can explain the increase in the lattice parameter of pyrochlore structure.

3.3.2 Scanning electron microscopy and Energy dispersive spectra
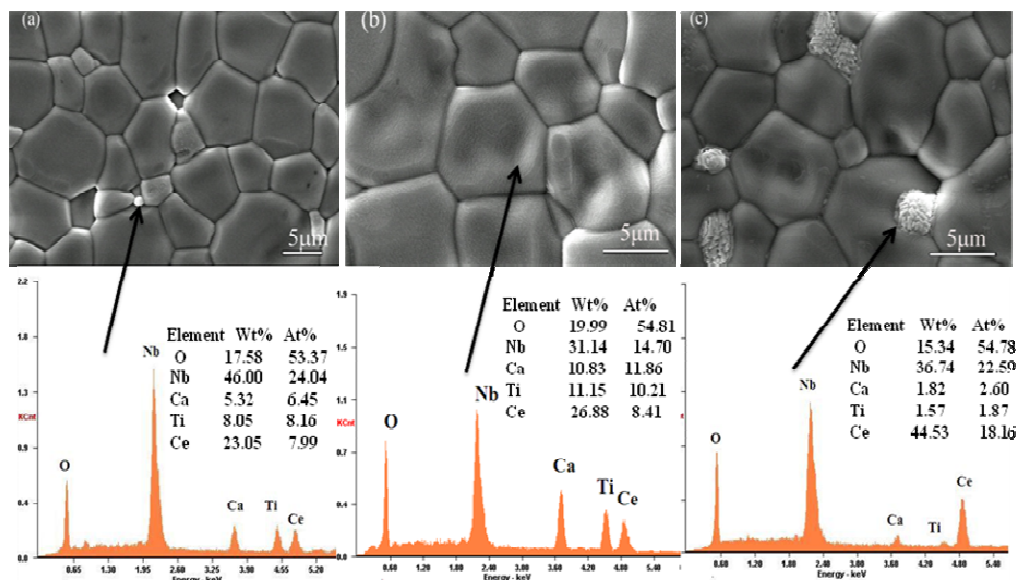
Fig.3.3 Typical scanning electron micrographs of (a) $CaCe_{0.6}TiNbO_{6.4}$, (b) $CaCe_{0.7}TiNbO_{6.55}$, (c) $CaCe_{0.8}TiNbO_{6.7}$ with microchemical analysis.

Fig. 3.3a-c shows typical sintered microstructure and EDS spectra for the $CaCe_{0.6}TiNbO_{6.4}$, $CaCe_{0.7}TiNbO_{6.55}$ and $CaCe_{0.8}TiNbO_{6.7}$ respectively. The micrographs reveal well sintered grains in the size range 2-5 μm. It is also clear from the SEM micrographs that only $CaCe_{0.7}TiNbO_{6.55}$ microstructure reveals monophasic morphology with uniform grain size. The microstructure of other two compositions indicates the presence of secondary phase morphology with the main sintered microstructure. Compositions with Ce content less than 0.7 shows presence of very minor amount of Nb_2O_5 secondary phase with a little Ca, Ti and Ce

substitution and compounds with Ce content greater than 0.7 showed Ce-Nb rich secondary phase as confirmed by the EDS analysis. These results are consistent with the XRD analysis.

3.3.3 X-ray photoelectron spectroscopic studies
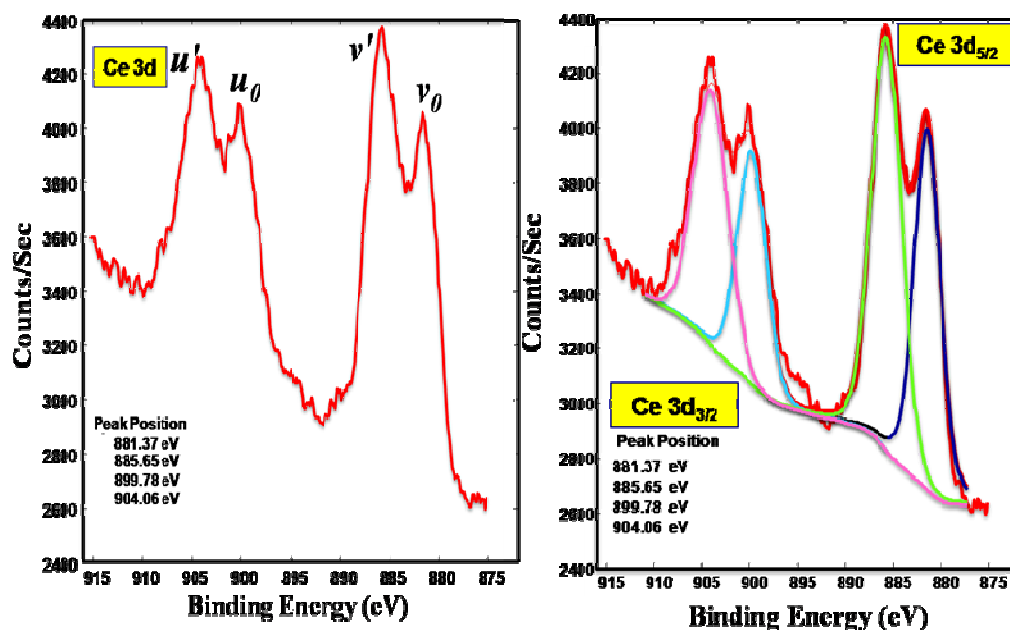
Fig. 3.4. Ce 3d XP spectra and the curve fitting example of Ce 3d XPS peaks of $CaCe_{0.7}TiNbO_{6.55}$

Fig. 3.4 displays Ce 3d XP spectra and the curve fitting example of Ce 3d XPS peaks of $CaCe_{0.7}TiNbO_{6.9}$. The final state occupation of electrons in Ce 4f determines the distinct features of the spectra. The Ce 3d spectrum of Ce^{3+} consists of two pairs of doublets namely u_0/v_0 and u'/v'. These doublets correspond to a mixture of the $Ce3d^9 O 2p^6 Ce4f^1$ and $Ce 3d^9 O 2p^5 Ce 4f^2$ final states [Mullins D.R *et al* 1998]. The XPS Ce $3d_{5/2}$ and $3d_{3/2}$ doublets are commonly denoted by u and v and extend in the energy

range of 880-920 eV. The u'/v' doublet is due to the photoemission from the Ce(III) cations [Reddy B.M *et al* 2003]. Other doublet observed in the spectrum is labeled as u_0 and v_0. These peaks are a shakedown feature resulting from the transfer of one electron from a filled O 2p orbital to a Ce 4f orbital during photoemission from Ce^{3+} cations. The presence of u_0/v_0 and v'/u' doublet peaks in the spectra indicates that the $CaCe_{0.7}TiNbO_{6.55}$ sample contains the reduced cerium i.e. Ce^{3+}.

3.3.4. Impedance analysis

Impedance spectroscopy has been employed to evaluate the electronic and ionic components of the total charge transport. This method involves the employment of low amplitude ac frequency signal over the sample and separation of real and imaginary parts of impedance. The impedance measurements were carried out for all the samples in the frequency range of 10 Hz to 1 MHz and in the temperature range of 30 to 600 °C. The Fig. 3.5, Fig. 3.6 and Fig 3.7 shows the impedance curves of (a) real (Z') and (b) imaginary (Z") components and (c) log ac conductivity as a function of log frequency at various temperatures for $CaCe_xTiNbO_{7-\delta}$ (x = 0.5, 0.6, 0.7, 0.8, 0.9 and 1). In order to explain the conductivity mechanism the impedance spectra of $CaCe_{0.7}TiNbO_{6.55}$ composition has been chosen and explained in detail.
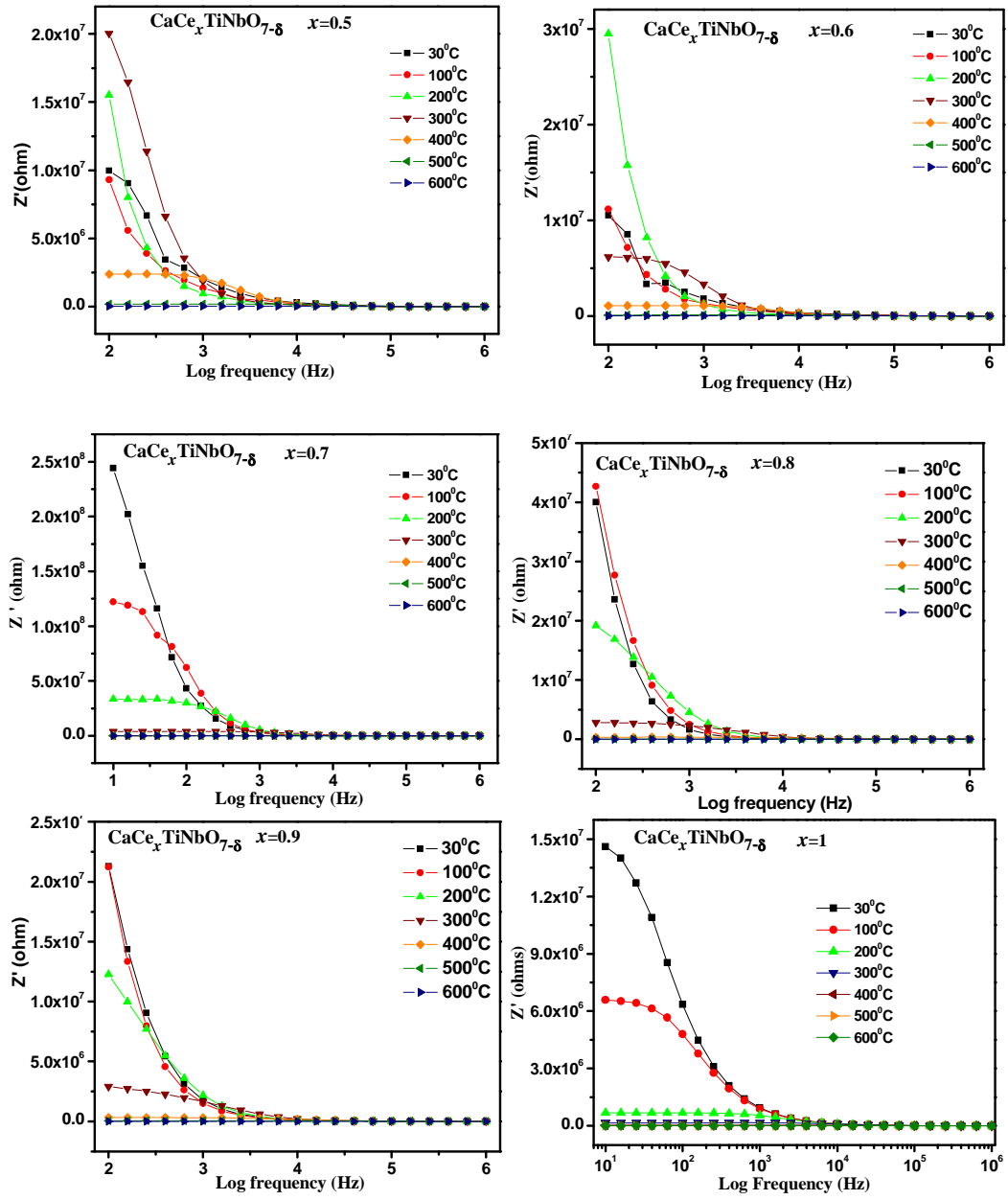
Fig. 3.5 Impedance curves of real (Z') component as a function of log frequency at various temperatures for $CaCe_xTiNbO_{7-\delta}$ (where x = 0.5, 0.6, 0.7, 0.8, 0.9 and 1)
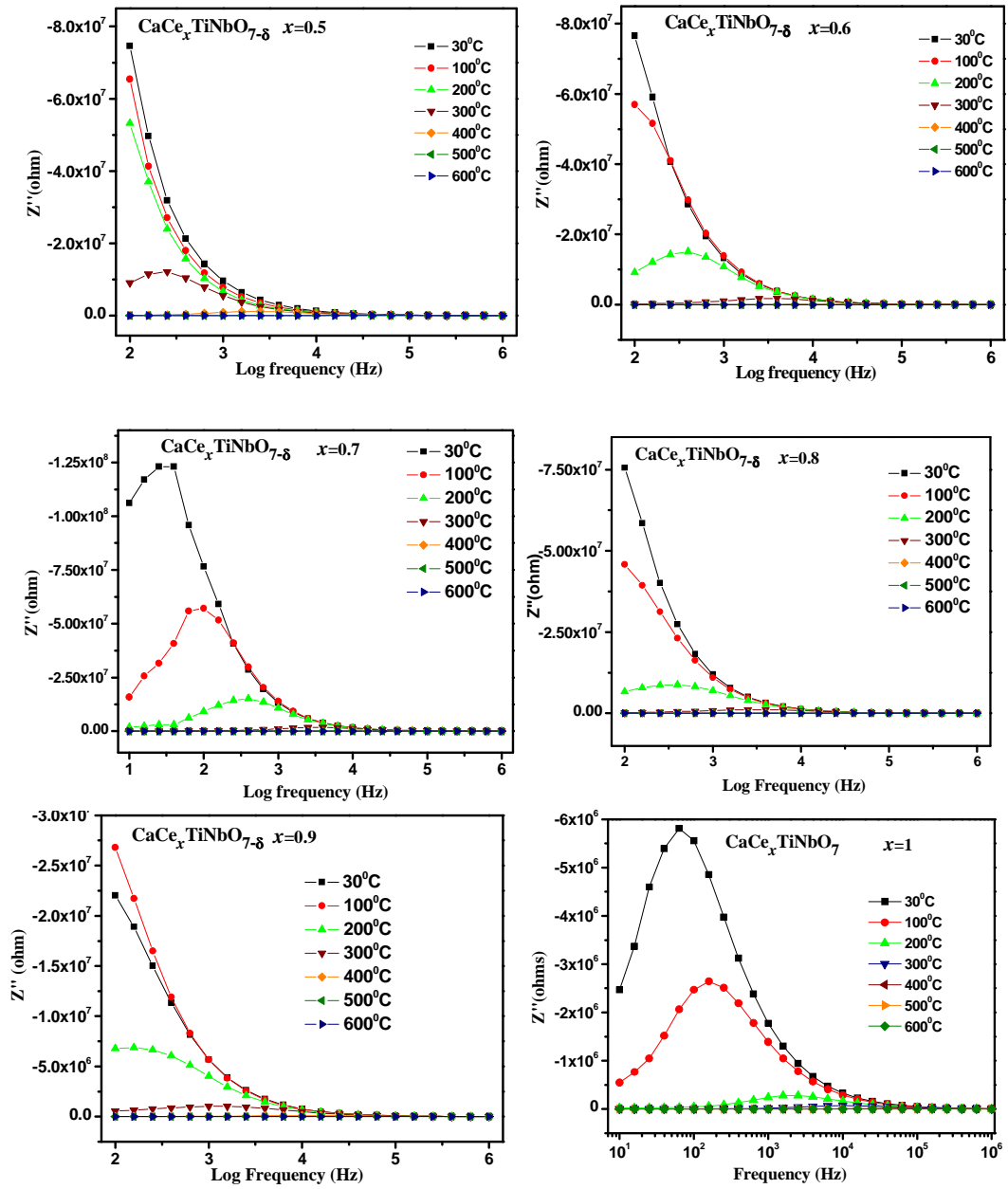
Fig. 3.6 Impedance curves of imaginary (Z'') component as a function of log frequency at various temperatures for $CaCe_xTiNbO_{7-\delta}$ (where $x = 0.5$, 0.6, 0.7, 0.8, 0.9 and 1)
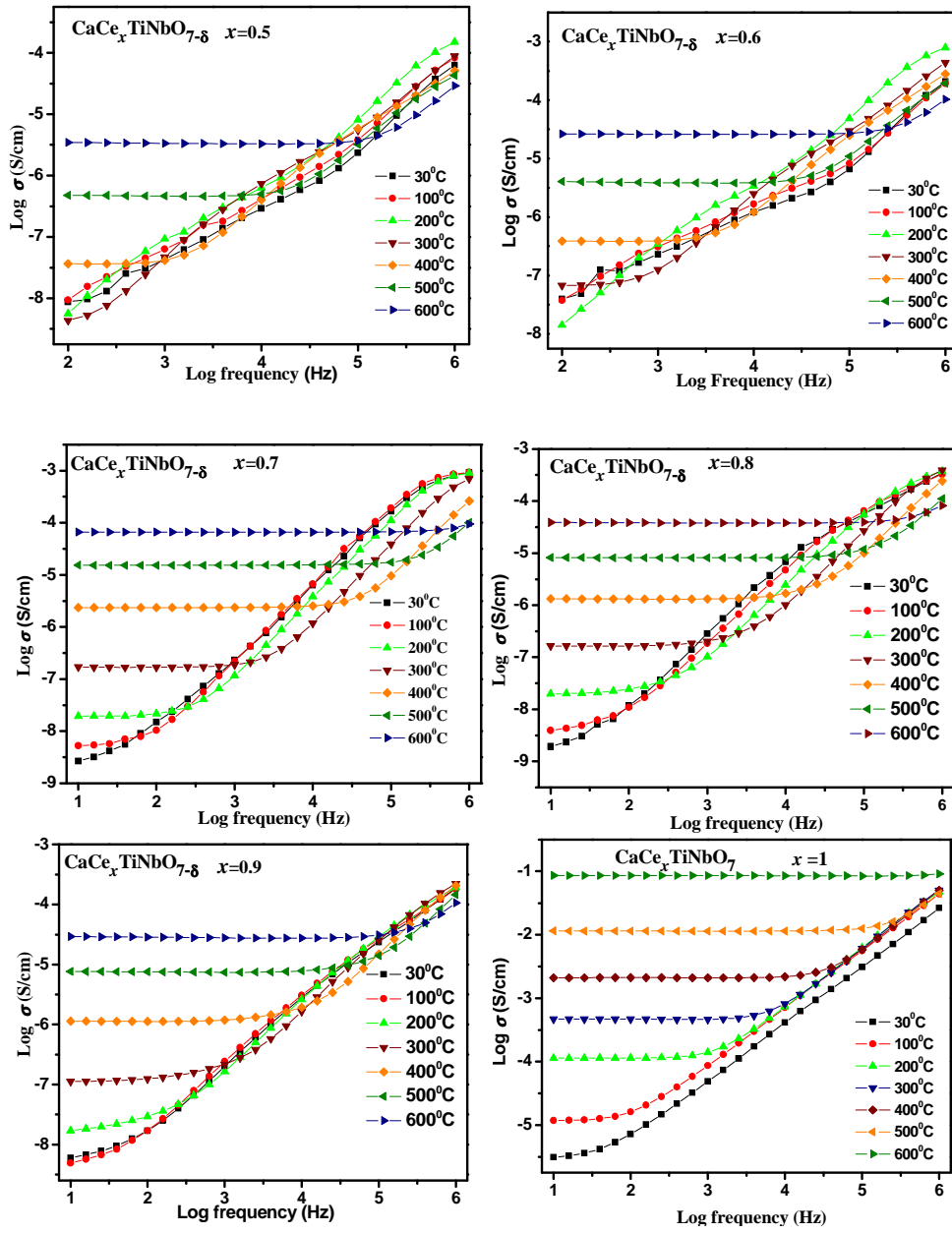
Fig. 3.7 Impedance curves of log ac conductivity as a function of log frequency at various temperatures for $CaCe_xTiNbO_{7-\delta}$ (where x =0.5, 0.6, 0.7, 0.8, 0.9 and 1)
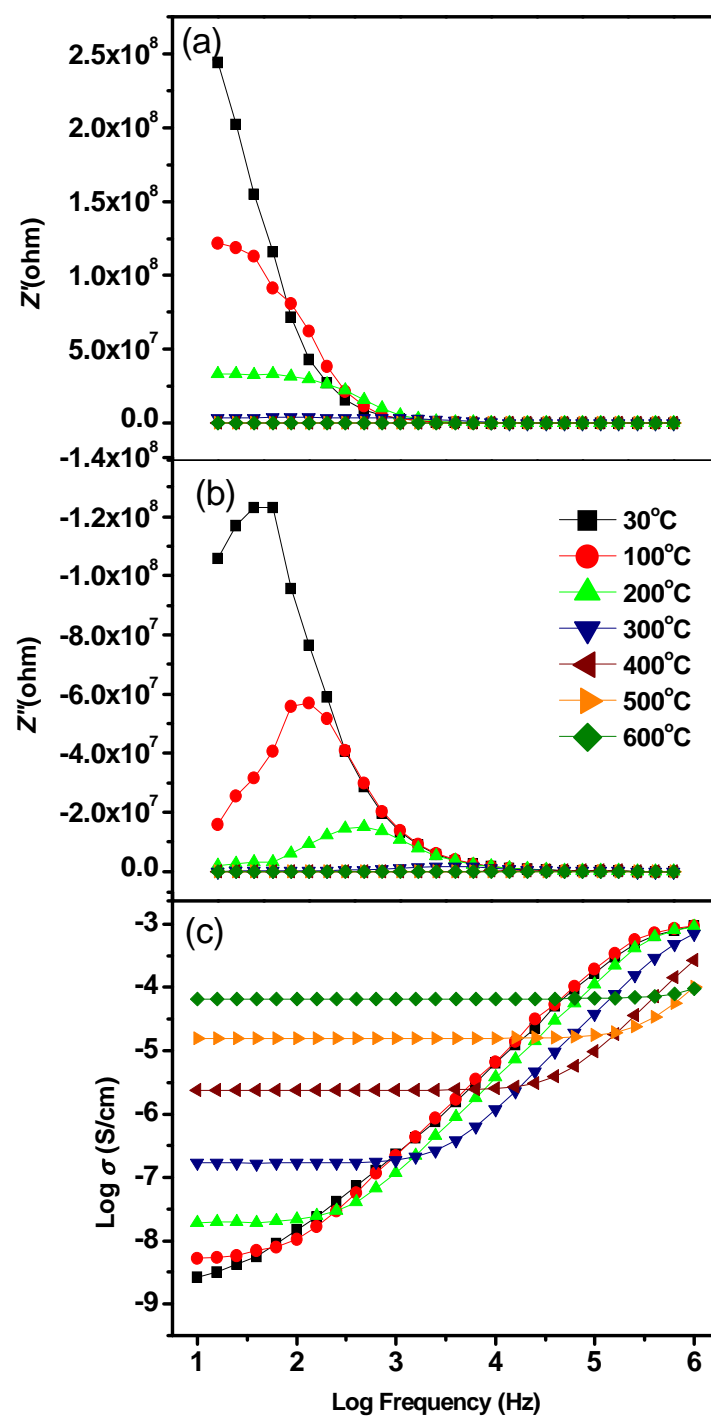
Fig. 3.8 Impedance curves of (a) real (Z') and (b) imaginary (Z")
components and (c) log ac conductivity as a function of log frequency at
various temperatures for $CaCe_{0.7}TiNbO_{6.55}$.

Fig. 3.8 shows the variation of the real part of impedance (Z'), imaginary part of impedance (Z''), and log conductivity against log frequency for the $CaCe_{0.7}TiNbO_{6.55}$ composition. The resistance is strongly affected by the variation of temperature (Fig. 3.8a). The increase in conductivity with temperature shows the NTCR behavior of the semicoducting materials. The increase in frequency also decreases the resistance magnitude significantly. The resistance magnitudes coincide above a certain frequency irrespective of the temperature variation. Fig. 3.8b shows the variation of imaginary part of impedance with log frequency from 30 to 600 ^{o}C. The Z'' value deceases with increase in temperature and it reaches a maximum value at a particular frequency for every temperature indicating a relaxation mechanism in the compound. This peak value shifts from low frequency region to high frequency region with increase of temperature. Peak broadening is also seen in this material confirming the presence of space charges with increase of temperature. And due to the accumulation of space charges, Z'' magnitude merges to a single value at high frequency region. The effect of temperature and frequency on the ac conductivity of the sample is given in Fig. 3.8c. It can be observed that the frequency dependence of conductivity shows two distinct regions, within the measured frequency range 10 Hz-1MHz, they are (a) the low frequency plateau region and (b) high frequency dispersion region. The low frequency plateau region corresponds to the frequency independent conductivity, σ_{dc}.

The plateau region of conductivity increases with increase in temperature and the value of plateau region conductivity also increase with temperature. At high temperatures and low frequencies, this contribution is nearly frequency independent and thus can be assumed to reflect the dc conductivity. This type of conductivity is attributed to the long range transport of mobile electrons in response to the temperature and field. At very high frequencies, the conductivity is found to be linearly dependent on frequency due to hopping transport of localized charge carriers [Elliott S.R 1987]. The ac conductivity of most of the materials is explained by the Jonscher's power law equation [Jonscher A.K 1977].

$$\sigma(\omega) = \sigma_{dc} + A\omega^{n} \qquad (3.1)$$

where $\sigma(\omega)$ is the frequency dependent conductivity at frequency ω, σ_{dc} is the dc term associated to the mobile charge, A is a frequency independent and temperature-dependent parameter and n is the slope of high frequency dispersion data (n assumes a value between 0 and 1). It is very clear from Fig. 3.8c that the conductivity behavior exhibited by the compound does not fit this simple equation. As mentioned in the earlier text there is a visible change in the slopes as we go from lower frequency region to the higher frequency region. Hence in this system two slopes can be drawn one in the low plateau region and other in the dispersion region. Therefore the frequency dependent ac conductivity can be characterized using the two term power relation

$$\sigma(\omega) = \sigma_0 + A_1\omega^{n_1} + A_2\omega^{n_2} \qquad (3.2)$$

Again A_1 and A_2 are frequency independent and temperature dependent constants. The slopes n_1 and n_2 will be, n_1 can be $0 \leq n_1 \leq 1$ and n_2 can be $0 \leq n_2 \leq 2$. The term σ_0 corresponding to the translational hopping gives the long range electrical transport (i.e dc conductivity) in the long time. The second term, $A_1\omega^{n_1}$ characterizes the low frequency region and corresponds to the translational hopping motion (short range hopping), whereas the one at high frequencies $A_2\omega^{n_2}$ corresponds to a localized or reorientational hopping or hopping of electron back and forth between two charged defects [Funke K 1993].

The ac conductivity behavior of $CaCe_{0.7}TiNbO_{6.55}$ fitted with the double power law by nonlinear regression analysis at different temperatures. The values of n_1 and n_2 are obtained from the slopes of the low frequency plateau and high frequency regions of the conductivity plots and are found to vary between 0.02-0.8 and 0.2-1.3 respectively. Fig. 3.9 shows the variation of n_1 and n_2 as a function of temperature. In the investigated temperature range, n_1 decrease with temperature and shows a trend to zero. This implies that the translational hopping gives the long range electrical transport (dc conductivity) in the limit of very long times as the temperature increases and frequency decreases as observed in the conductivity plots. This indicates that d.c conductivity dominates at higher temperatures in the low frequency region, where as n_2 increases first up to

300°C and then decreases with further increase of temperature. The increase of slope is attributed to the localized orientation hopping or hopping of electron back and forth two charged species. In the present system, the high frequency localized orientation hopping at the low temperature range (<300 °C) may be attributed to the formation of dipoles, Nb^{3+} - V_o and Ti^{3+} - V_o. (This can happen when Nb^{5+} and Ti^{4+} can capture electrons which are left behind in the lattice from cerium as explained in the next part of the discussion.) assisted by small polaron mechanism [Polaiz-Barramco A *et al* 1998]. While for the temperatures above 300 °C, the charge carriers trapped at the defect sites may form large polarons and conduction occurs as a result of thermally activated large polarons. These results are consistent with the trends of temperature dependence of n_1 and n_2 in the investigated temperature range.

From Fig. 3.8(c), the frequency at which the dispersion region diverged from the dc conductivity is defined as the characteristic frequency (ω_o) and it is termed as hopping frequency. It can be observed that at the hopping frequency ω_o, the relaxation effects begin to appear, moves toward higher frequency with increasing temperature.
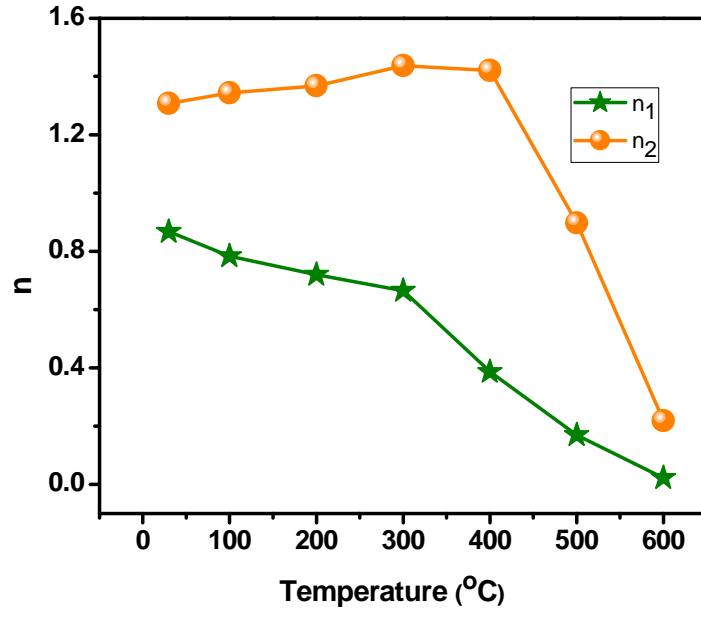
Fig. 3.9 Variation of double power exponents (n_1 and n_2) as a function of temperature of $CaCe_{0.7}TiNbO_{6.55}$
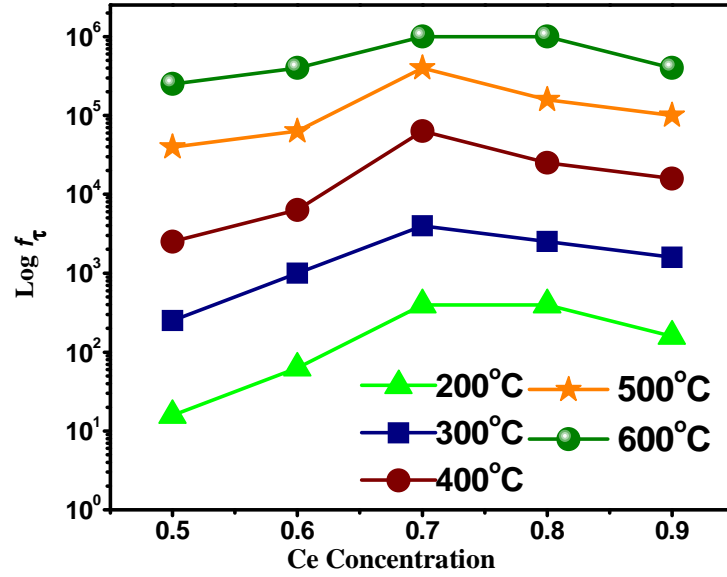
Fig. 3.10 Hopping frequency ($\log f_\tau$) vs Ce concentration.

Fig. 3.9 shows the variation of hopping frequency as a function of Ce concentration for different temperatures. It can be observed that the hopping frequency reaches a maximum value for the $CaCe_{0.7}TiNbO_{6.55}$ composition.

This can be explained like this: As seen by the XRD results, $CaCe_{0.7}TiNbO_{6.55}$ composition gives a phase pure compound and the other compositions have secondary phases, thereby indicating that the maximum amount of Ce is present in Ce^{3+} state only in this particular composition. As explained above, the release of more electrons from cerium creates more localized hopping by creating defect states in the lattice. Thus, hopping frequency is dependent on cerium concentration and indicates the degree of disorder in the system.

3.3.5 Electrical conductivity studies

The authors have already reported pyrochlore structured compounds in Ca-RE-Nb-Ti-O (RE = Y, La, Nd, Sm or Bi) which show very good dielectric properties [Prabhakar Rao P *et al* 2006] But when the rare-earth used is cerium, the compound has become black and semiconducting. This may be due to the variable valency of cerium. Here the structure will be stable only if cerium remains in the Ce^{3+} state in order to satisfy the oxygen stoichiometry of the compound instead of its stable valency as Ce^{4+}. The excess oxygen coming from CeO_2 will be released to the atmosphere leaving behind an electron in the lattice and this electron will be responsible for the semiconductivity of the compound [Prabhakar Rao P *et al* 2003].
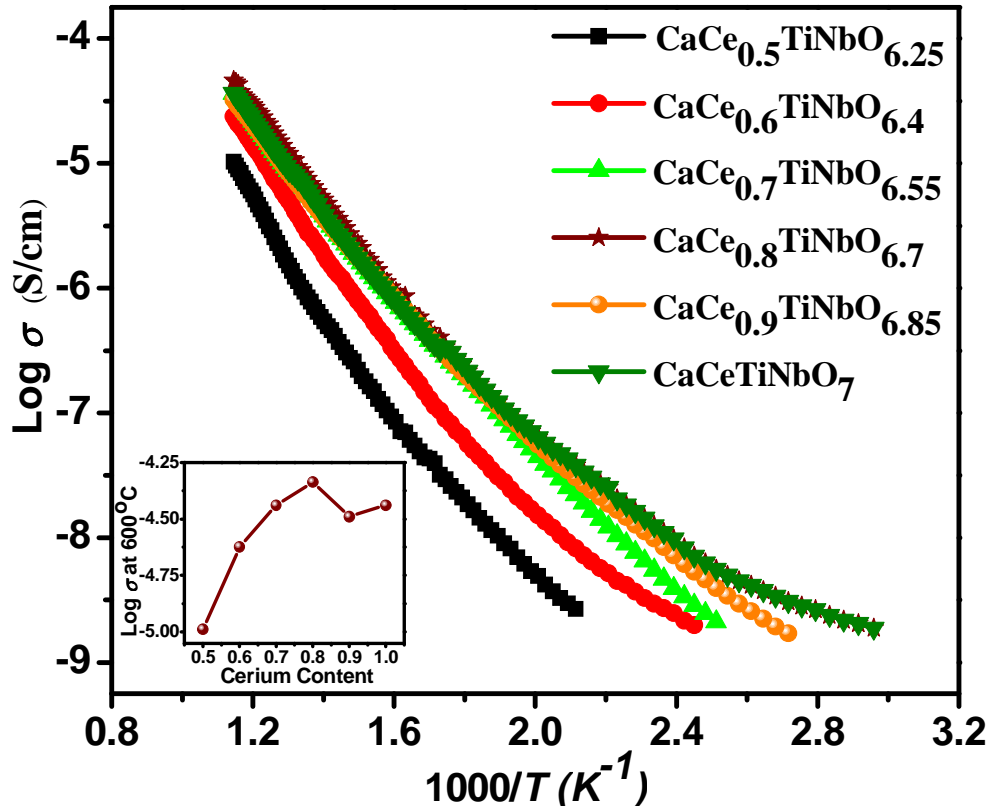
Fig. 3.11 Variation of log σ vs. 1000/T of CaCe$_x$TiNbO$_{7-\delta}$ system and the variation of conductivity with Ce concentration at 600°C in inset

Fig.3.10 shows the electrical conductivity (log σ) as a function of absolute temperature (1000/T). The electrical conductivity data of the above compounds reveals that they are semiconducting in nature. The nature of variation obeys the Arrhenius equation $\sigma = \sigma_0 \exp(-Ea/K_B T)$ where Ea is the activation energy, T is the absolute temperature and σ_0 is the pre-exponential factor. Activation energy, Ea of the carriers of the conduction process is calculated using the above equation and are listed in Table 3.1. It is observed that the conductivity comes to a maximum for the composition CaCe$_{0.8}$TiNbO$_{6.7}$ and thereafter a decrease is observed for CaCe$_{0.9}$TiNbO$_{6.85}$

and CaCeTiNbO$_7$. This may be due to the formation of large amount of Ce rich secondary phase around the grains (as indicated in the EDS analysis) which acts as a less conductive path for the electrons. Fig. 3.10 shows the electrical conductivity of the compounds as a function of Ce concentration at 600°C. It can be seen that the electrical conductivity increases with increase of cerium content up to Ce = 0.8. The increase in conductivity is attributed to change in carrier concentration (conduction electrons) in the lattice, which arises from Ce^{3+} with increase of cerium content. Thus, conductivity of CaCe$_{0.8}$TiNbO$_{6.7}$ at 600 °C is 4.61x10^{-5} S/cm whereas the conductivity of CaCe$_{0.5}$TiNbO$_{6.25}$ is 1.03 x10^{-5} S/cm.

3.3.6 Conclusions

In conclusion, nonstoichiomeric misplaced displacive pyrochlores in Ca-Ce-Ti-Nb-O system have been synthesized by the conventional solid state route. The XRD results reveal that the ionic radius ratio, (r_A/r_B) precludes the formation of phase pure pyrochlores for the stoichiometric composition CaCeTiNbO$_7$, whereas non-stoichiometric composition CaCe$_{0.7}$TiNbO$_{6.55}$, crystallizes in a cubic pyrochlore structure by displacement of the A and O' ions from their ideal positions. The impedance analysis indicates relaxor behavior of these compounds due to disorder in the system.

CHAPTER 4

PYROCHLORE TYPE CERAMIC SEMICONDUCTING OXIDES IN
Ca – Ce – Ti – M – O (M = Nb OR Ta) SYSTEM

PART   I

EFFECT OF CERIUM CONCENTRATION ON STRUCTURE AND ELECTRICAL PROPERTIES OF
Ca – Ce – Ti – M – O (M=Nb OR Ta) SYSTEM

4.1.1 Introduction

Complex oxides containing rare earth and transition metals having different valence states exhibit interesting transport properties. The crystal structure and the constituent elements play an important role in these properties, which include superconductivity [Schilling A. *et al* 1996], semiconductivity [Zheng W. P *et al* 2001] and semiconductivity to metal transition [Gupta A *et al* 2009]. Among the above, semiconducting oxides have been widely used in electronic industries because of their unique and useful electrical characteristics. Semiconducting ceramics find several applications as in thermistors, PTCR materials, gas sensors, catalysts and photoelectrolysis of water [Csete de Györgyfalva *et al* 1999; Tian Z.R *et al* 1997]. Some useful semiconducting oxides have been developed in different structural families such as spinels, perovskites, and pyrochlores [Basu. A et *al* 2001; Nobre M.A.L. and Lanfredi S. 2001] for temperature measurement. The spinel-structured semiconducting ceramics are the most common known materials for negative temperature coefficient of resistance (NTC) thermistors manufacturing. However, the application of these materials is limited to temperatures below 300°C due to their instability and changing electrical characteristics. Therefore, there is a need for the development of new materials which have good electrical characteristics at high temperatures.

Pyrochlore structured materials have a wide range of important physical and chemical properties such as electrical, magnetic, dielectric, optical and catalytic properties, since its lattice allows a wide variety of aliovalent cations substitution. Pyrochlore structure has a general formula $A_2B_2O_7$ with eight molecules (Z = 8) per unit cell. The larger A^{3+} cations in 8 fold coordination with O^{2-} ions and smaller B^{4+} cations in 6 fold coordination with O^{2-} ions are ordered in alternatively <110> direction [Subrahmanian M.A *et al* 1983]. Recently, during our investigation we reported a new family of dielectric materials in the quaternary oxide system, $CaO-RE_2O_3-TiO_2-Nb_2O_5$ (RE = Y, Sm, Gd, Dy) and all these compounds having pyrochlore type structure are insulators and also colorless. But when we replace Ce in place of other rare earths, the compound becomes black and semiconducting [Prabhakar Rao P *et al* 2004, 2003] . The semiconducting nature of the compound is probably due to conversion of Ce^{4+} to Ce^{3+} in the lattice to reduce the number of oxygen atoms to maintain the oxygen stoichiometry (4:7) in the pyrochlore type structure. In this chapter, a new series of pyrochlore type semiconducting ceramic oxides in a Ca – Ce – Ti – M – O (M = Nb or Ta) system were prepared in different stoichiometric compositions to investigate the effect of Ce content on the structure, microstructure and semiconductivity. The NTC characteristics have also been studied for these compounds.

4.1.2. Experimental

4.1.2.1 Preparation of samples

A new series of pyrochlore type semiconducting ceramic oxides in different stoichiometric compostions: $(Ca_{1.5}Ce_{0.25}Ti_{0.25})(Ti_{0.75}M_{1.25})O_7$, $(Ca_{1.25}Ce_{0.5}Ti_{0.25})(TiM)O_7$, $(CaCe_{0.75}Ti_{0.25})(Ti_{1.25}M_{0.75})O_7$, and $(Ca_{0.75}CeTi_{0.25})(Ti_{1.5}M_{0.5})O_7$ (M = Nb or Ta) were prepared by the conventional ceramic route using $CaCO_3$, TiO_2, Nb_2O_5 and Ta_2O_5 (99.9%, Acros Organics, Geel, Belgium) and CeO_2 (99.9%, Aldrich Chemicals, Milwaukee, WI) as starting materials. Stoichiometric amounts of the chemicals were weighed and then thoroughly wet mixed in an agate mortar with acetone as the wetting medium and dried by keeping in a hot air oven at 100^oC. The process of mixing and drying was repeated thrice to attain a homogeneous mixture. The mixed product was calcined at 1300^oC for 3hrs in air. The calcination was repeated twice with intermittent grinding. The calcined powder was then mixed with 4 wt. % of polyvinyl alcohol (PVA; hydrolysis level 85-88%) solution. PVA acts as a binder and provides mechanical strength to the pressed samples. The powder was pelletized into cylindrical pellets with a diameter of 10 mm and a thickness around 1-2 mm using a hydraulic press by applying a pressure of 250 MPa. The green compacts were heated at 600^oC for 1h to burn off the PVA and were then sintered at 1350^oC for 9 h in air. The density of the

sintered pellets was estimated from their geometrical dimensions and the experimental density was obtained in the range of 85 to 93% of theoretical density.

4.1.2.2 Characterization techniques

The phase purity of the sintered samples were characterized by using a Phillips X'Pert-Pro diffractometer (Eindhoven, The Netherlands), under the following conditions: Ni filtered Cu-Kα radiation, tube power 40kV, 30mA receiving slit 0.2mm, and using graphite monochromator. The powder patterns were recorded at room temperature in the angular 2θ range from 10 to 90°. The structure was further confirmed using Raman Spectroscopy. Raman spectra analysis was conducted on the samples from 200 to 800cm^{-1} using a spectrometer (Bruker RFS 100/S) and an Nd: YAG laser operating at 1064 nm and incident power of 150 mW with a Ge detector. Excitation and emission spectra were recorded using a Spex-Fluorolog DM3000F spectrofluorimeter and a 450 W Xenon flash lamp as the exciting source. The XPS analysis was performed on the pellets in an ultrahigh vacuum using PHI Versa probe scanning XPS Microprobe with monochromatic X-ray source of Al Kα (hν =1486.6 eV). The polished and thermally etched (1325°C /30min) pellets were coated with a thin layer of gold by sputter coater (JEOL JFC-1200 fine coater) so as to make the surface of the pellet conducting. The surface morphology of

the pellets was studied using a scanning electron microscope (SEM) (JEOL, JSM 5600LV). To measure the electrical properties of the compounds, a high temperature curing silver paste was applied to both sides of the pellets and cured at 600^oC for 30 min in a tubular furnace. These pellets were then attached with long silver lead wires on both sides. Impedance measurements of the pellets were carried out; from 30 to 600 °C in the frequency range 10 Hz to 1 MHz using a computer controlled impedance analyzer (Solartron, SI 1260). The dc conductivity with respect to temperature was measured using a high resolution digital multimeter, (Philips, PM 2525 multimeter). The conductivity was measured in a temperature range of 30^oC to 600^oC.

4.1.3 Results and discussion

4.1.3.1 XRD and structure

The $(Ca_{1.5}Ce_{0.25}Ti_{0.25})(Ti_{0.75}M_{1.25})O_7$, $(Ca_{1.25}Ce_{0.5}Ti_{0.25})(TiM)O_7$, $(CaCe_{0.75}Ti_{0.25})(Ti_{1.25}M_{0.75})O_7$, and $(Ca_{0.75}CeTi_{0.25})(Ti_{1.5}M_{0.5})O_7$ (M = Nb or Ta) powder compacts were well densified by sintering at 1350°C for 9 h yielding 85 to 93% of theoretical density (Table 4.1.1). The visual color of the sintered pellets varies from gray to black with increase of the cerium content in the compound.
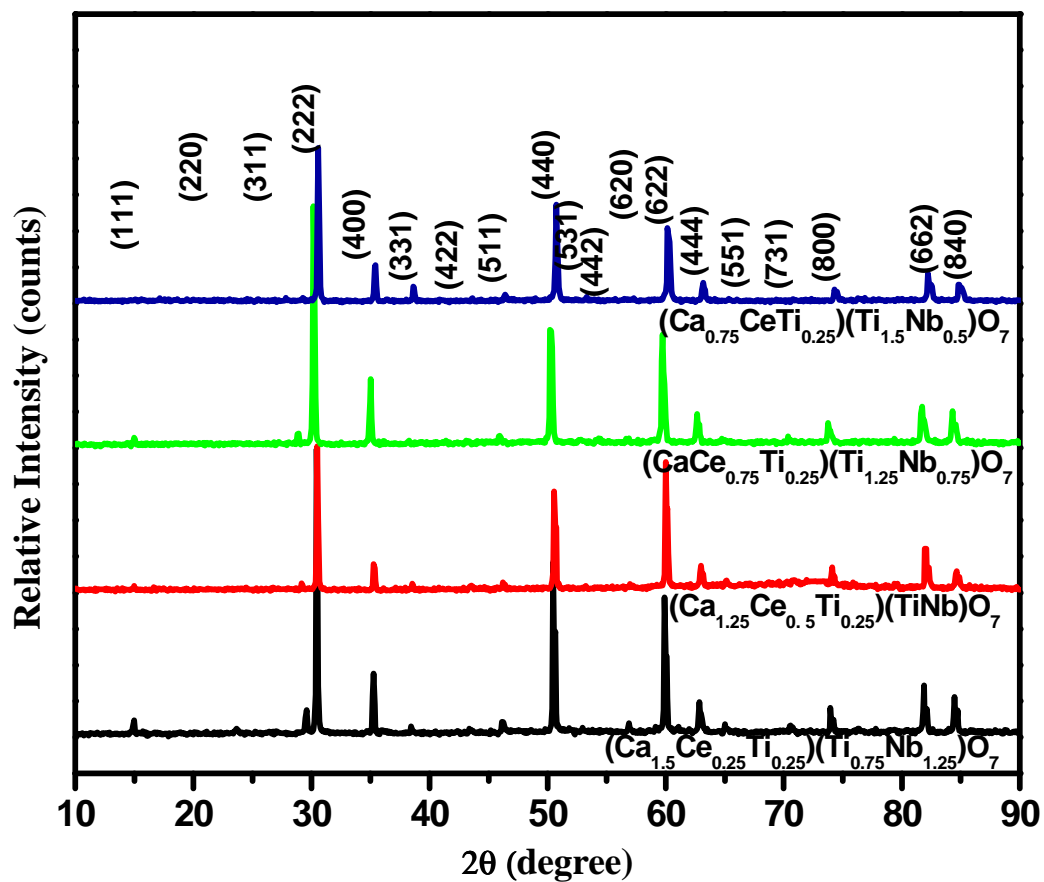
Fig. 4.1.1 Powder X-ray diffraction patterns of the sintered compounds for various stoichiometric compositions in Ca – Ce – Ti – Nb – O system

The patterns are similar to the earlier reported pyrochlore type compounds of the formula $A_2B_2O_7$ such as $CaLaNb_2O_7$ [Istomin S.Y *et al* 1997] and $Ln_2Zr_2O_7$ [Saruhan B *et al* 2004]. All the reflections are assigned to the cubic pyrochlore phase in the space group *Fd3m* (No. 227). All the reflections are typical of the cubic pyrochlore type structure, which is characterized by the presence of typical super lattice peaks at $2\theta \sim 14°$ (111), $28°$(311), $37°$(331),

45°(511) with either minor variations in their intensity or diminishing of some of these peaks with composition.
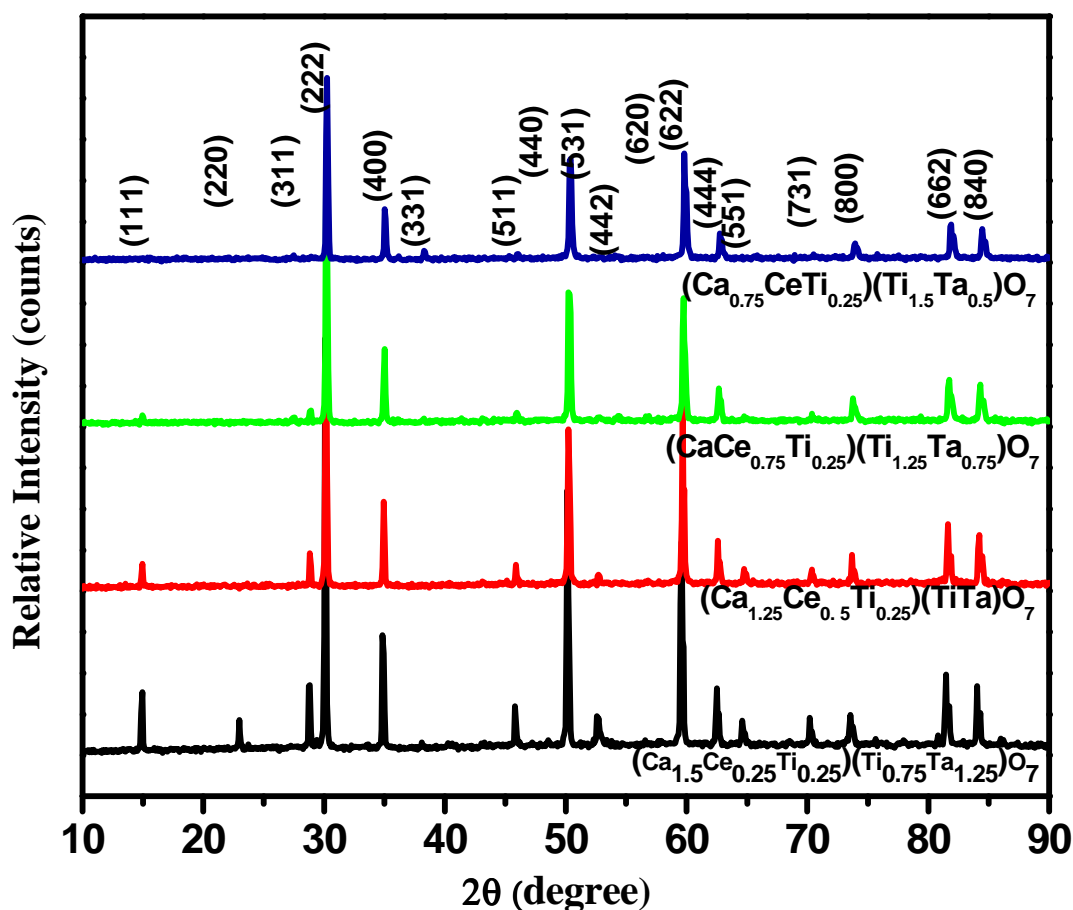
Fig.4.1.2 Powder X-ray diffraction patterns of the sintered compounds for various stoichiometric compositions in Ca – Ce – Ti –Ta – O system

An interesting observation was that the intensity of the characteristic super-structure peaks (111), (311), (511) systematically diminishes and that of (331) increases on going from $(Ca_{1.5}Ce_{0.25}Ti_{0.25})(Ti_{0.75}M_{1.25})O_7$ to

$(Ca_{0.75}CeTi_{0.25})(Ti_{1.5}M_{0.5})O_7$. Further, the intensity of the super lattice peaks is more intense in the tantalum compounds than that of the niobium compounds. This can be explained based on the relative ionic sizes of the cations occupying the lattice sites in the pyrochlore structure. Pyrochlore structure has a general formula, $A_2B_2O_7$, in which there are two types of cation sites, A and B. The occupancy of these two sites is mainly decided by the ionic radii of different metal ions at A and B to keep the ratio of the ionic radius of the cations at the A site to that at the B site within the tolerance range 1.46 to 1.80 [Subramanian M.A $et\ al$, 1983]. The ionic radii of Ca^{2+} and Ce^{3+} in eight fold coordination are 1.12 and 1.143 Å respectively and that of Ti^{4+} and Nb^{5+} or Ta^{5+} in six fold coordination are 0.60 and 0.64 Å respectively [Shannon R.D 1976]. The Ca and Ce ions (which are bigger) occupy the A sites and the transition metals Ti^{4+} and Nb^{5+} or Ta^{5+} ions occupy the B sites. Also since the total number of Ti and Ta or Nb ions at the B sites is more than total number of Ca and Ce ions at the A sites, some of the Ti ions might be occupying the A sites. However, it is to be mentioned here that Ti is too small to occupy the large 8-fold coordinated environment in pyrochlores. But, recent studies of the pyrochlores in $(Ca_{1.5}Ti_{0.5})NbTi)O_7$ [Nguyen B $et\ al$ 2008] and $CaO\text{-}TiO_2\text{-}(Nb,Ta)_2O_5$ [Roth R S $et\ al$ 2008] indicated that Ti^{4+} ions (up to 25% of the large A-sites) mixes with the much larger Ca^{2+} ions on the A-sites by displacing from the ideal 8-

coordinated position to achieve satisfactory coordination environment. Such pyrochlores are termed as misplaced-displacive cubic pyrochlores. Their XRD patterns exhibit weak forbidden reflections (e.g., 442) and also they show relaxor behavior at low temperatures. The weak characteristic reflection (442) of displaced pyrochlores is observed in both the Ti rich niobate and tantalate powder XRD patterns.

Composition	Theoretical density (g/cc)	Experimental density (g/cc)	Relative density (%)	σ at 600^oC, (S/cm)	Ea (eV)	Lattice parameter, a (Å)
$(Ca_{1.5}Ce_{0.25}Ti_{0.25})(Ti_{0.75}Nb_{1.25})O_7$	4.54	4.21	93	2.35×10^{-7}	1.60	10.2853(6)
$(Ca_{1.25}Ce_{0.5}Ti_{0.25})(TiNb)O_7$	4.73	4.30	91	2.20×10^{-5}	1.13	10.2712(6)
$(CaCe_{0.75}Ti_{0.25})(Ti_{1.25}Nb_{0.75})O_7$	4.92	4.56	93	4.86×10^{-4}	0.62	10.2545(7)
$(Ca_{0.75}CeTi_{0.25})(Ti_{1.5}Nb_{0.5})O_7$	5.11	4.63	91	1.20×10^{-3}	0.54	10.2472(7)
$(Ca_{1.5}Ce_{0.25}Ti_{0.25})(Ti_{0.75}Ta_{1.25})O_7$	5.87	4.98	85	3.39×10^{-7}	1.31	10.2942(5)
$(Ca_{1.25}Ce_{0.5}Ti_{0.25})(TiTa)O_7$	5.80	5.05	87	3.07×10^{-6}	1.06	10.2798(5)
$(CaCe_{0.75}Ti_{0.25})(Ti_{1.25}Ta_{0.75})O_7$	5.72	5.18	91	2.23×10^{-4}	0.62	10.2735(6)
$(Ca_{0.75}CeTi_{0.25})(Ti_{1.5}Ta_{0.5})O_7$	5.64	5.18	92	8.74×10^{-4}	0.53	10.2554(7)

Table.4.1.1 Density, electrical conductivity data and lattice parameter for various compositions in a Ca–Ce–Ti–M–O (M = Nb or Ta) system.

Based on these results, it is easy to assume that the present pyrochlore oxides involve mixing of three cations (Ca, Ce and Ti) on the A sites and two types of cations (Ti and Nb or Ta) on the B sites. The radius ratios were estimated accordingly. The ratio of r_A/r_B (r_A and r_B are the average ionic radii of the A and B cations) varies from 1.68 [in $(Ca_{0.75}CeTi_{0.25})(Ti_{1.5}M_{0.5})O_7$] to

1.73 [in $(Ca_{1.5}Ce_{0.25}Ti_{0.25})(Ti_{0.75}M_{1.25})O_7$], which is within the limiting radius required for the stabilization of pyrochlore type structure. However, as the radius ratio decreases, the pyrochlore structure tends to get converted from a well ordered structure to a somewhat disorder structure, in which the super-structure peaks diminish. It is earlier reported that reducing the difference in ionic radius between the A and B cations in the pyrochlore structure favors disordering [Licia M *et al* 2000]. Disorder increases with increasing r_B and decreasing r_A. The lattice parameters '*a*' for all the compositions are given in Table 4.1.1. It can be seen that the lattice parameter of these solid solutions decreases with increase of Ce and Ti content in the Ca–Ce–Ti–M–O system. Based on the relative ionic size considerations of Ce^{3+} (1.143 Å) and Ti^{4+} (0.605 Å), one can explain the decrease in the lattice parameter of pyrochlore type structure.

4.1.3.2 Raman spectroscopic investigations

Raman spectroscopic investigation has been found to provide the short range structural differences since Raman spectroscopy is primarily sensitive to oxygen-cation vibrations and is an excellent probe for local disorder [Glerup M *et al* 2001]. Based on the crystal structure and group theory analysis of $A_2B_2O_7$ pyrochlores in the *Fd*3*m* space group (No. 227), there are only six Raman active modes for the pyrochlore structure.

$$\Gamma_{raman} = A_{1g} + E_g + 4F_{2g} \qquad (4.1.1)$$

These modes involve only motion of the oxygen atoms since the A and B cations, whose site symmetry is D_{3d}, gives rise to non active Raman phonon modes.
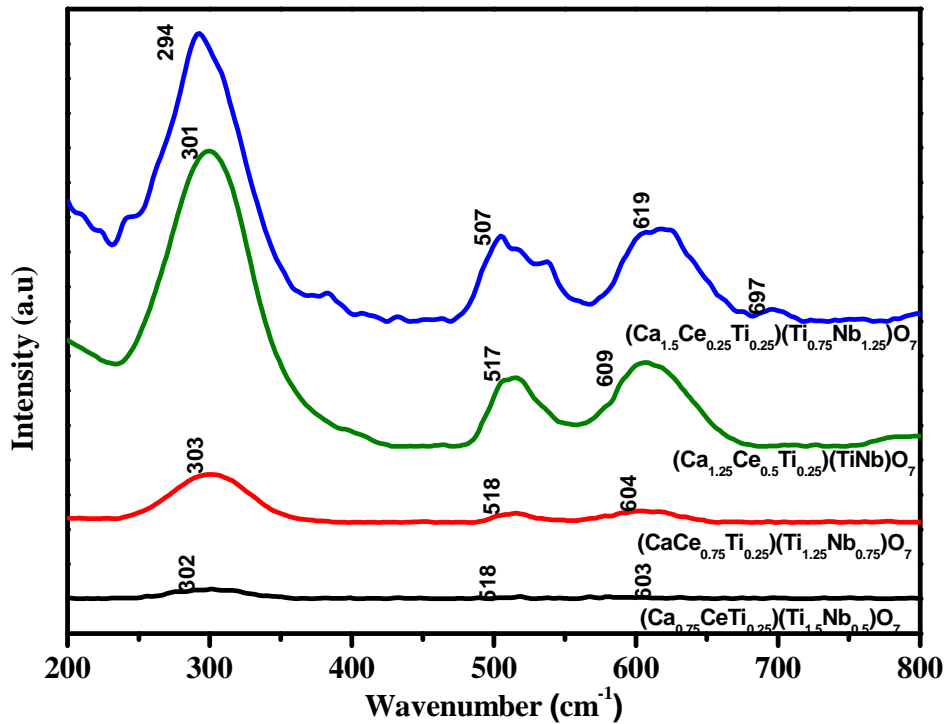
Fig.4.1.3 Raman spectra for various stoichiometries in Ca-Ce-Ti-Nb-O system

Therefore, the crystalline $(Ca_{1.5}Ce_{0.25}Ti_{0.25})(Ti_{0.75}M_{1.25})O_7$, $(Ca_{1.25}Ce_{0.5}Ti_{0.25})$ $(TiM)O_7$, $(CaCe_{0.75}Ti_{0.25})(Ti_{1.25}M_{0.75})O_7$ and $(Ca_{0.75}CeTi_{0.25})(Ti_{1.5}M_{0.5})O_7$ (M = Nb or Ta) samples were also examined by Raman spectroscopy in the frequency range 200-800 cm^{-1} to look for any structural differences. In all the spectra for both niobium and tantalum compounds, except for $(Ca_{1.5}Ce_{0.25}Ti_{0.25})$

$(Ti_{0.75}M_{1.25})$ O_7 (Fig. 4.1.3and Fig. 4.1.4), there are three intensive bands which are due to an overlap of the vibrational bands.
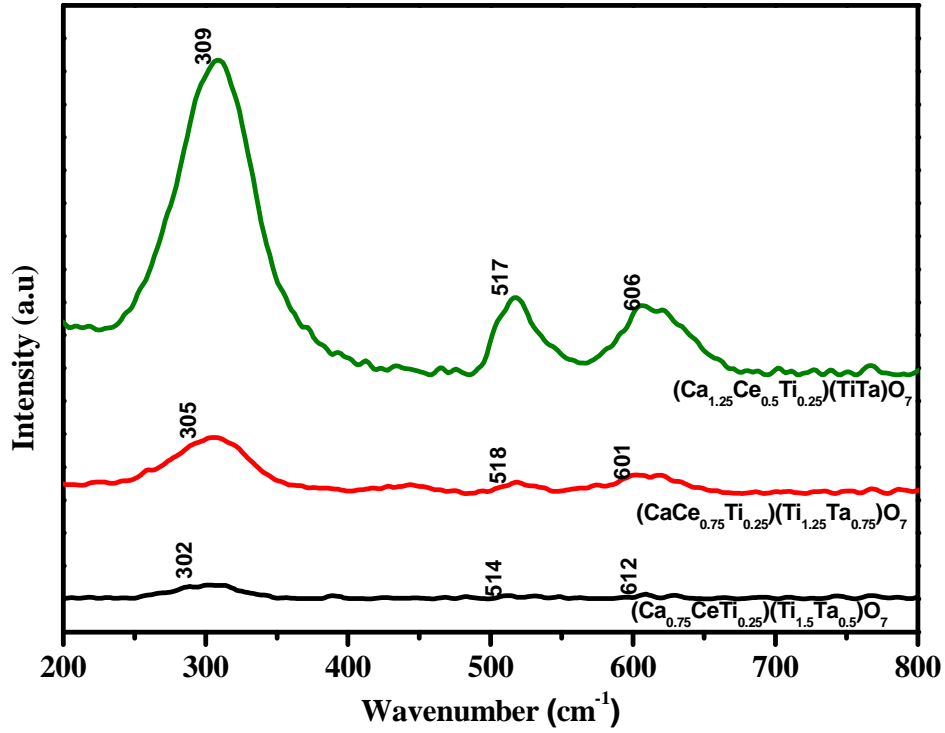
Fig.4.1.4 Raman spectra for various stoichiometries in Ca-Ce-Ti-Ta-O system

On the basis of previous literature data, the three intense bands at 600-620, 507-519, 294-310 cm^{-1} can be assigned to A_{1g}, E_g, F_{2g} modes respectively [Hess N J *et al* 2002]. The bands indicated in Fig. 4.1.3 and Fig. 4.1.4 are in agreement with the ones reported for pyrochlore type oxides [Huiling D 2004]. The location of three remaining F_{2g} modes is more difficult since the literature data are not consistent owing to their weak intensity. However, the weaker modes are observed in the calcium rich compounds where the obtained Raman

intensity is high. The mode at 697 cm^{-1} for the Nb compound (Fig. 4.1.3) is assigned to one of the three F_{2g} modes. The most notable difference in the Raman spectra between the various pyrochlores is the significant decrease in overall Raman intensity, when Nb^{5+} is replaced by Ta^{5+}. Small distortions of the atomic positions caused by B cation species in pyrochlore structure compounds affect the force constant of vibrational mode resulting small shift in vibrational frequency. Thus, the full width at half maximum (FWHM) of a vibrational mode provides a measure of the level of localized short range structural disorder in the materials. In both the tantalate and niobate compounds, considerable increase in FWHM of the vibrational modes combined with the decrease of Raman intensity suggest that the progressive incorporation of Ti^{4+} in B site induce the A site cations array significantly more disordered and the extent of disorder is more in the niobates than that of tantalates. These results are in concurrent with the XRD analysis. This suggests that despite their long range pyrochlore structure, the short range structure exhibits an increasing level of localized A-site cation mixing or disorder with the increase of Ti content in the compound.
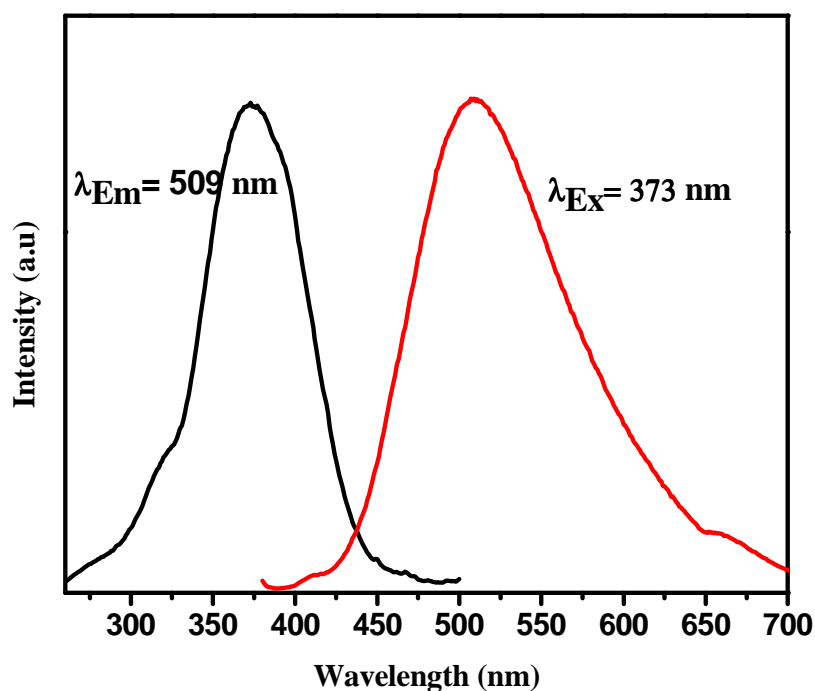
Fig. 4.1.5 Excitation and emission spectra of $(Ca_{1.5}Ce_{0.25}Ti_{0.25})(Ti_{0.75}Ta_{1.25})O_7$ sample.

In order to corroborate the presence of Ce^{3+} ions and also the absence of Raman modes for $(Ca_{1.5}Ce_{0.25}Ti_{0.25})(Ti_{0.75}Ta_{1.25})O_7$, the fluorescence was performed. The fluorescence properties of this particular compound indicates that it gives intense broad emission spectra in the wavelength range of 400-700 nm for the excitation of the 373 nm wavelength with maxima at about 509 nm (Fig. 4.1.5). The excitation band in the wavelength range of 275 – 400 nm with maxima at 373 nm is assigned to Ce^{3+} 4f → 5d transitions separated by crystal field splitting of the 5d state [Duan C J *et al* 2008]. This further confirms the presence of cerium in Ce^{3+} state in the compound. It is also concluded that the

vibrational modes are not observed for the $(Ca_{1.5}Ce_{0.25}Ti_{0.25})(Ti_{0.75}Ta_{1.25})O_7$ compound, because cerium induces strong fluorescence which hides weaker bands.(When cerium presents in Ce^{3+} state and also in a low concentration in the compound which acts as an activator, causes fluorescence in this compound).

4.1.3.3 X-ray photoelectron spectroscopic studies

The final state occupation of electrons in Ce 4f determines the distinct features of the spectra. The Ce 3d spectrum of Ce^{3+}consists of two pairs of doublets namely u_0/v_0 and u'/v', these doublets correspond to a mixture of the Ce $3d^9$ O $2p^6$Ce$4f^1$ and Ce $3d^9$ O $2p^5$ Ce $4f^2$ final states [Mullins D R *et al* 1998]. The XPS Ce $3d_{5/2}$ and $3d_{3/2}$doublets are commonly denoted by u and v and extend in the energy range of 880-920 eV. The peaks labeled u are due to $3d_{3/2}$ spin orbit states and those labeled v are the corresponding $3d_{5/2}$ spin-orbit states. The u'/v' doublet is due to the photoemission from the Ce(III) cations [Reddy B M *et al* 2003]. The Ce 3d spectrum of $(Ca_{0.75}CeTi_{0.25})(Ti_{1.5}Nb_{0.5})O_7$ contains only the completely reduced Ce^{3+} cation. Another doublet observed in the spectrum is labeled as u_o and v_o. These peaks are a shakedown feature resulting from the transfer of one electron from a filled O 2p orbital to a Ce 4f orbital during photoemission from Ce^{3+} cations. The presence of u_o/v_o and v'/u'

doublet peaks in the spectra indicates that the $(Ca_{0.75}CeTi_{0.25})(Ti_{1.5}M_{0.5})O_7$ (M=Ta or Nb) sample contains the reduced cerium i.e. Ce^{3+}.
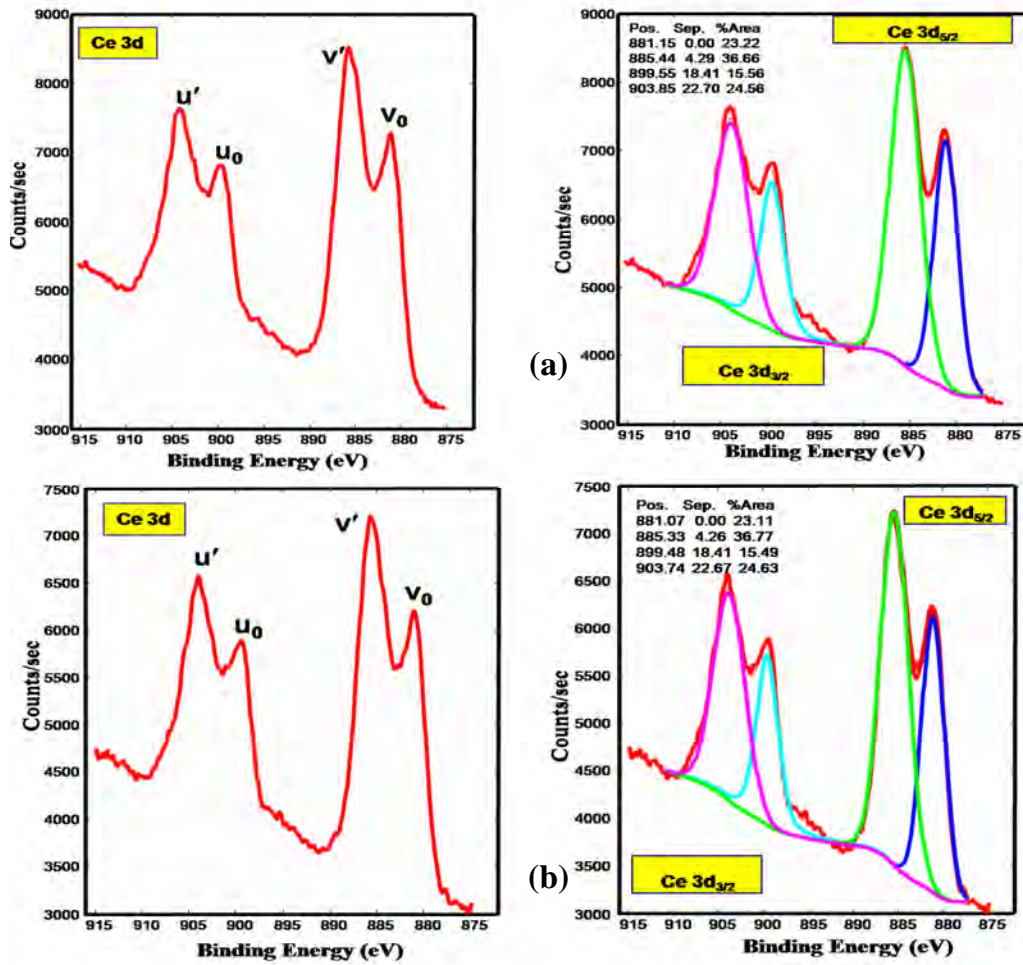
Fig 4.1.6 Ce 3d XP spectra and the curve fitting example of Ce 3d XPS peaks of $(Ca_{0.75}CeTi_{0.25})(Ti_{1.5}Nb_{0.5})O_7$ and $(Ca_{0.75}CeTi_{0.25})(Ti_{1.5}Ta_{0.5})O_7$

4.1.3.4 Scanning electron microscopy and microstructure
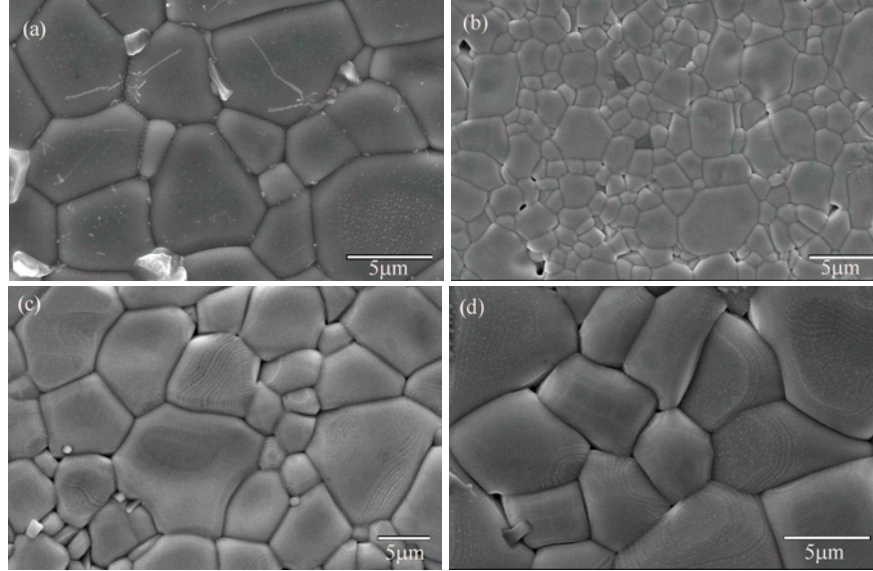
Fig.4.1.7 Typical scanning electron micrographs of

(a)$(Ca_{1.5}Ce_{0.25}Ti_{0.25})(Ti_{0.75}Nb_{1.25})O_7(b)(Ca_{1.25}Ce_{0.5}Ti_{0.25})(TiNb)O_7$

(c)$(CaCe_{0.75}Ti_{0.25})(Ti_{1.25}Nb_{0.75})O_7$(d) $(Ca_{0.75}CeTi_{0.25})(Ti_{1.5}Nb_{0.5})O_7$
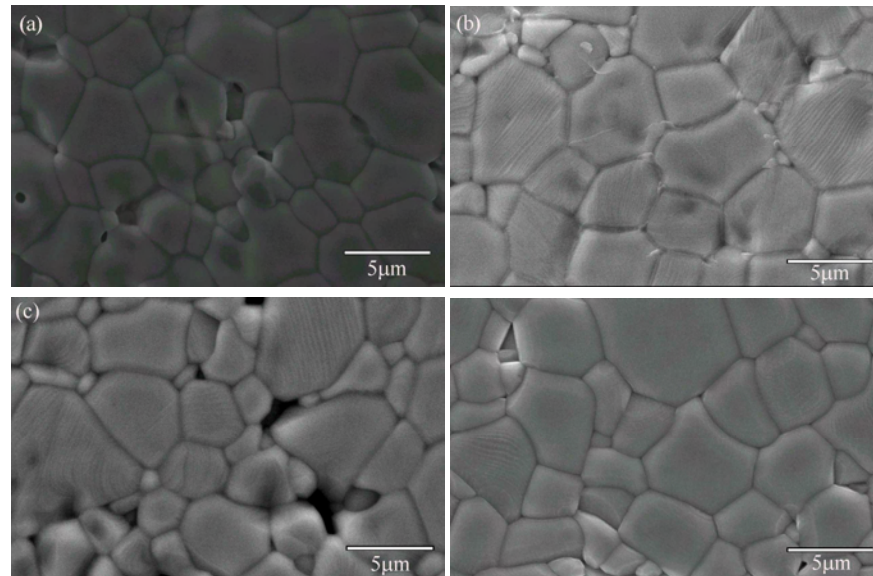
Fig. 4.1.8 Typical scanning electron micrographs of

(a) $(Ca_{1.5}Ce_{0.25}Ti_{0.25})(Ti_{0.75}Ta_{1.25})O_7$(b) $(Ca_{1.25}Ce_{0.5}Ti_{0.25})(TiTa)O_7$

(c) $(CaCe_{0.75}Ti_{0.25})(Ti_{1.25}Ta_{0.75})O_7$ (d)$(Ca_{0.75}CeTi_{0.25})(Ti_{1.5}Ta_{0.5})O_7$

The SEM micrographs recorded from thermally etched surface (1325^oC/30 min) of the sintered pellets are shown in Figs. 4.1.7 and 4.1.8. The microstructure of all the sintered compounds reveals well-grown grains with less porosity. It is observed that denser microstructure is observed and grains are more uniform in size with the increase of Ce and Ti content in the Ca–Ce–Ti–M–O system.

4.1.3.5 Impedance spectral measurements

Impedance spectroscopy has been employed to evaluate the electronic and ionic components of the total charge transport. This method involves the employment and proper interpretation of low amplitude variable frequency ac measurements. Impedance spectra of all the materials were studied in the temperature range 30-600°C and in the frequency range $10-10^6$ Hz.

Figs. 4.1.9 and 4.1.10 show typical impedance curves for real (Z') and imaginary (Z") components and log ac conductivity at various temperatures as a function of log frequency for selected compositions: $(Ca_{0.75}CeTi_{0.25})$ $(Ti_{1.5}M_{0.5})$ O_7 (M = Nb or Ta). The observed impedance plots are similar for both niobium and tantalum compounds in the measured temperature range. The variation of imaginary part of impedance with frequency at different temperatures provides information about the relaxation frequency of the resistive component. The peak occurs at 30°C and shifts to higher frequencies

with more broadness on increasing temperature up to 100 °C. The peak broadening suggests the presence of immobile species at low temperature. This type of low temperature relaxor behavior is also a characteristic of misplaced-displacive cubic pyrochlores [Roth R.S *et al* 2008]. The real part of impedance decreases with rise in frequency up to 100°C and meets at higher frequencies which indicate a possible release of space charge [Plcharski J and Weiczorek W 1988].
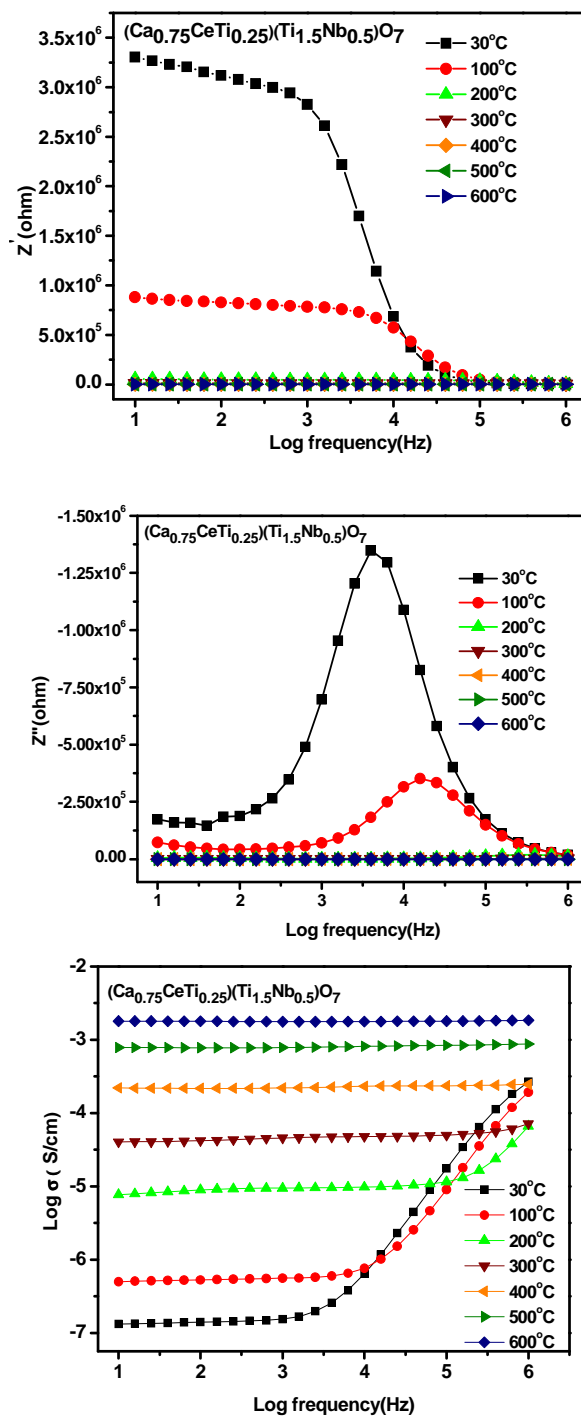
Fig. 4.1.9 Typical impedance curves of real (Z') and imaginary (Z")
components and log ac conductivity as a function of log frequency at various
temperatures for $(Ca_{0.75}CeTi_{0.25})(Ti_{1.5}Nb_{0.5})O_7$.
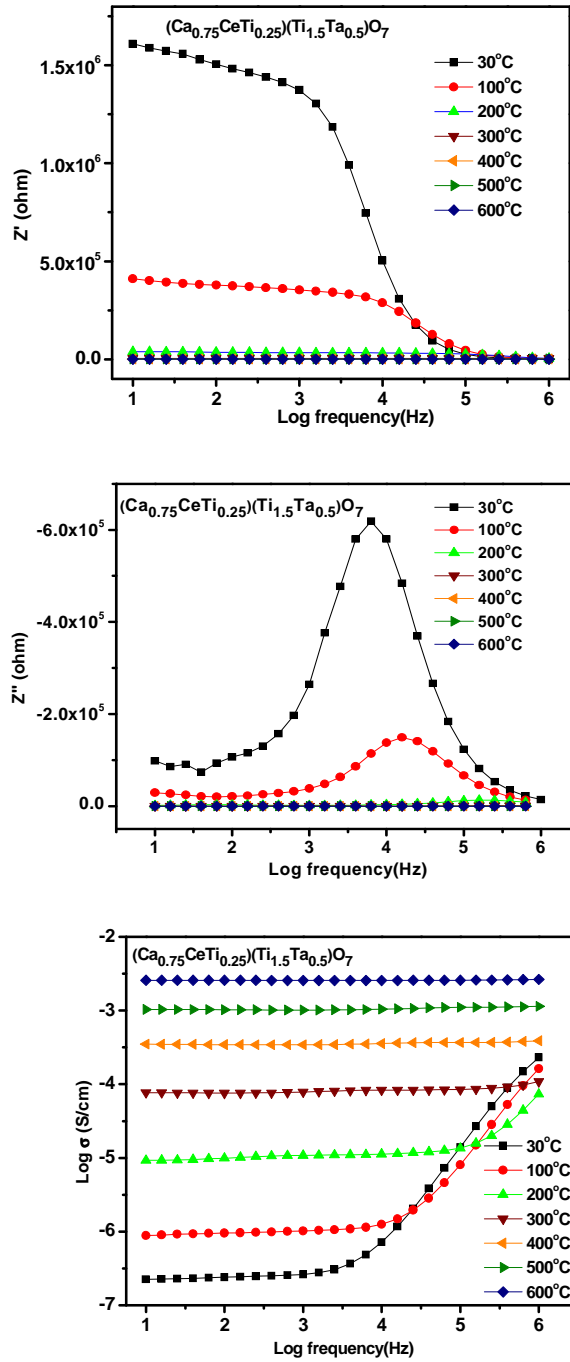
Fig. 4.1.10 Typical impedance curves of real (Z') and imaginary (Z'') components and log ac conductivity as a function of log frequency at various temperatures for $(Ca_{0.75}CeTi_{0.25})(Ti_{1.5}Ta_{0.5})O_7$.

From the curves, it is very clear that no relaxation behavior associated with oxide ion motion is observed beyond 100°C [Takai S 2006]. Figs. 4.1.9-4.1.10 show the ac conductivity plots (log σ) versus log f over a wide range of temperatures. All the curves show frequency – independent plateau corresponding to dc conductivity effects. It is known that ac conductivity is dependent on frequency in fast ionic conductors. The conductivity is governed by the Jonscher's universal power law [Jonscher A K 1977].

$$\sigma_{a.c.}(\omega) = \sigma_o + A\omega^n \qquad (4.1.2)$$

Where $\sigma_{a.c}(\omega)$ is the conductivity at frequency ω, σ_o is the dc term associated to the mobile charge, A is a frequency independent and temperature-dependent parameter and n is the slope of high frequency dispersion data (n assumes a value between 0 and 1). It is very clear from Fig. 4.1.10 and Fig.4.1.11 that the conductivity behavior exhibited by the compounds do not fit this simple equation. There is a visible change in the slopes as we go from lower frequency region to the higher frequency region at low temperature. Hence in this system two slopes can be drawn one in the low plateau region and other in the dispersion region.

Therefore the frequency dependent ac conductivity can be characterized using the two term power relation

$$\sigma(\omega) = \sigma_0 + A_1\omega^{n_1} + A_2\omega^{n_2} \qquad (4.1.3)$$

Again A_1 and A_2 are frequency independent and temperature dependent constants. The slopes n_1 and n_2 will be, n_1 can be $0 \leq n_1 \leq 1$ and n_2 can be $0 \leq n_2 \leq 2$. The term σ_0 corresponding to the translational hopping gives the long range electrical transport (i.e dc conductivity) in the long time. The second term, $A_1 \omega^{n_1}$ characterizes the low frequency region and corresponds to the translational hopping motion (short range hopping), whereas the one at high frequencies $A_2 \omega^{n_2}$ corresponds to a localized or reorientational hopping or hopping of electron back and forth between two charged defects [Funke K 1993]. The detailed description of the conductivity is given chapter 3 (section 3.3.4).

4.1.3.6 Electrical Conductivity

Earlier the authors reported the compounds of the pyrochlore type $Ca_3RE_3Ti_7Nb_2O_{26.5}$ and tetragonal tungsten bronze type $Ba_3RE_3Ti_5Nb_5O_{30}$ (RE = rare earth) which are electrical insulators and colorless, except when rare earth is not cerium [Prabhakr Rao P *et al* 2006, 2004, 2001]. However, when CeO_2 is used in place of other rare earth oxide, it has become black and semiconducting [Prabhakar Rao P *et al* 2003]. Though the stable valence state of cerium is Ce^{4+}, the oxygen stoichiometry in the above compounds would tally with the structure only if Ce remains in Ce^{3+} state. The excess oxygen coming from CeO_2 will be released to the atmosphere leaving behind an

electron in the lattice and this electron will be responsible for the semiconductivity of the compound.

$$2Ce^{4+} + 4O^{2-} \text{ (lattice)} \implies 2Ce^{3+} + 3O^{2-} + \tfrac{1}{2}O_2$$
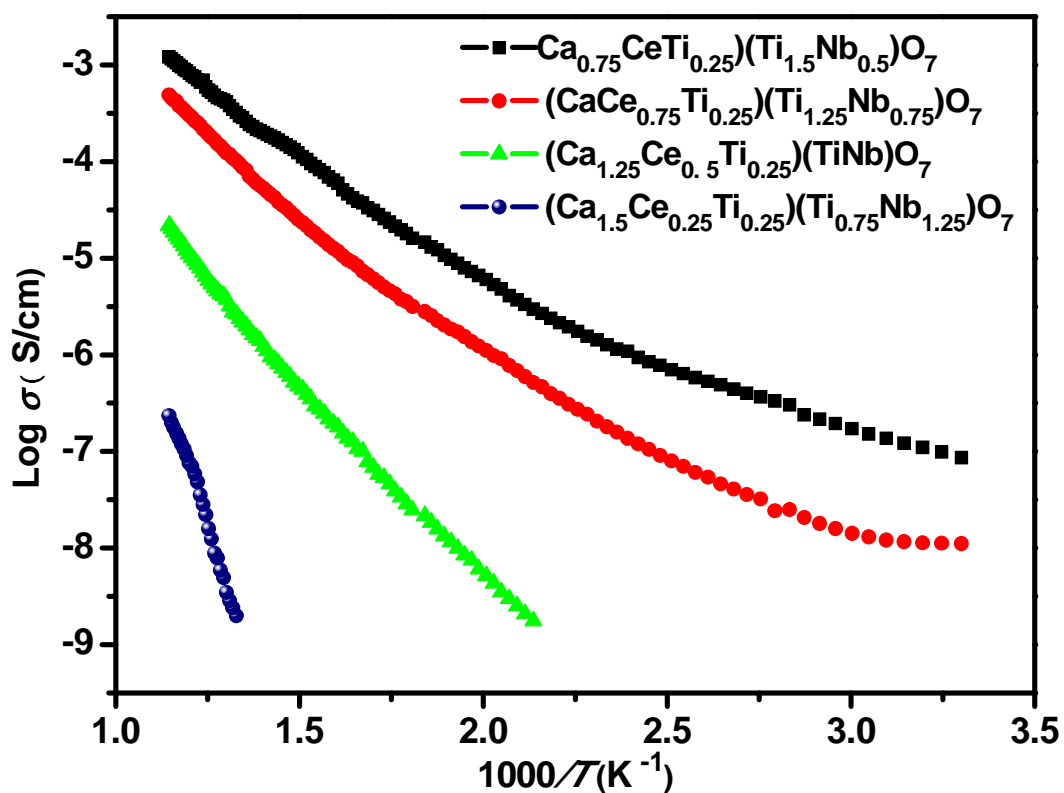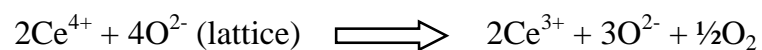
Fig.4.1.11 (a) Variation of log conductivity (σ) vs. reciprocal of temperature for Niobates
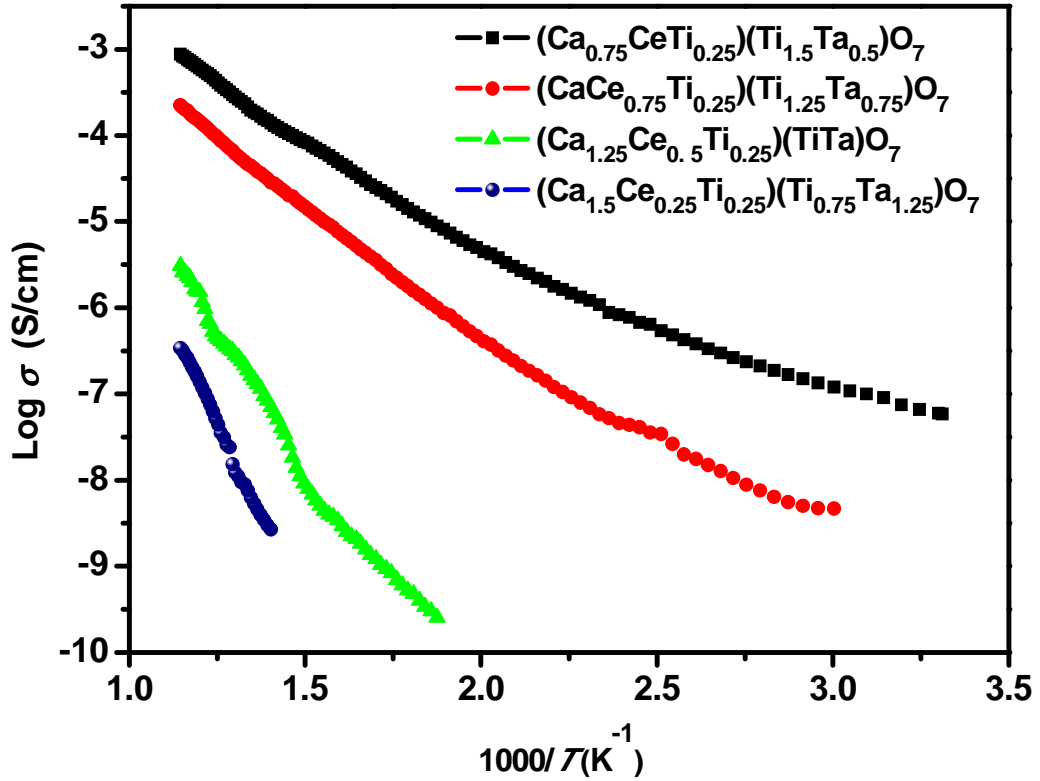
Fig. 4.1.11 (b) Variation of log conductivity (σ) vs. reciprocal of temperature for Tantalates

Fig. 4.1.11(a) and (b) shows the electrical conductivity (log σ) as a function of absolute temperature (1000/T) for all the compounds. The nature of variation is almost linear at higher temperatures, typically for 1000/T < 2 and it obeys the Arrhenius equation, $\sigma = \sigma_0 exp\ (-Ea/K_BT)$ where Ea is the activation energy, K_B Boltzman constant, T is the absolute temperature and σ_0 is the pre exponential factor. It is clear from the plot that the conductivity increases with the increase in temperature, which indicates the NTC behavior of the samples.

The activation energy of the carriers of the conduction process in the compounds is calculated using the above equation and the activation energy and the electrical conductivity at 600 °C for all the samples is given in the Table 4.1.1.
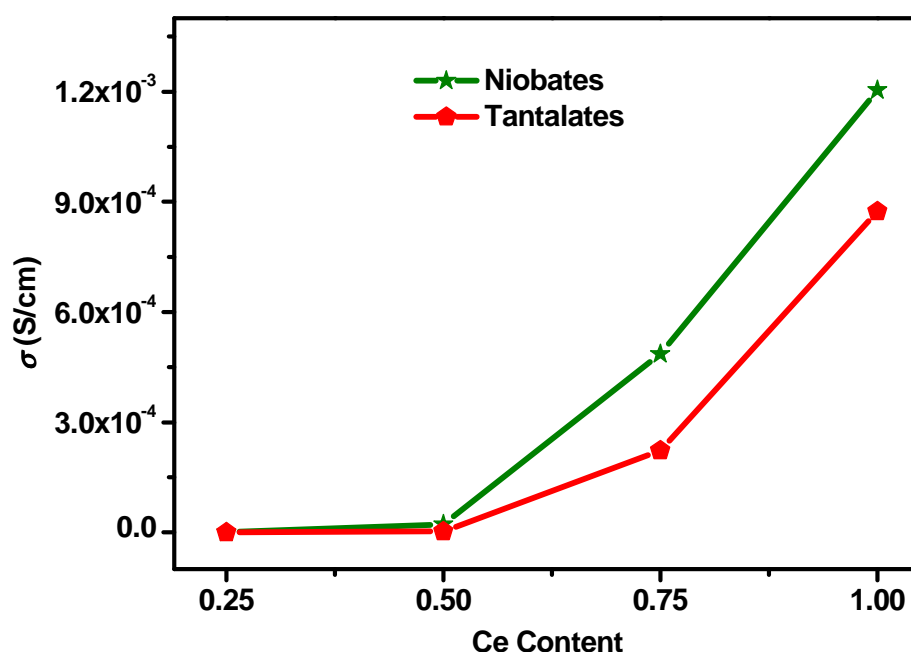
Fig. 4.1.12 Variation of conductivity at 600°C as a function of Ce concentration in Niobates and Tantalates.

Fig. 4.1.12 shows the electrical conductivity of the compounds as a function of Ce concentration at 600°C. It is very clear from the data and the Fig. 4.1.11 that the conductivity increases and the activation energy decreases with the increase of cerium concentration in the compounds. This observation can be explained based on the above discussion as follows: As the number of conduction electrons probably arise from Ce^{3+} in the lattice would increase

with the progressive substitution of Ce in the compound. This would increase the number of current carriers in the conduction band and consequently lower the conduction band energy level. Therefore, the activation energy of carriers will decrease with increase of Ce content in the compound. It is also observed that the conductivity is fairly same for both the niobium and tantalum compounds having low concentrations of cerium. Further, the conductivity does not show any linear relationship with the Ce content. As discussed above in the XRD part, these compounds are changing gradually from ordered pyrochlore lattice to somewhat disordered pyrochlore lattice with increase of Ce content and the niobates are more disordered pyrochlore structure than the tantalates. As reported earlier that variations in the electronic and ionic conductivity of pyrochlore compounds, $A_2B_2O_7$ are related to disordering of the A- and B-site cations [Lian J *et al* 2001]. It may be possible to explain that the sudden increase in conductivity in these compounds can be attributed to the disorder structure with the increase of Ce concentration. Thus, the conductivity for cerium rich oxides, $(Ca_{0.75}CeTi_{0.25})(Ti_{1.5}Nb_{0.5})O_7$ and $(Ca_{0.75}CeTi_{0.25})(Ti_{1.5}Ta_{0.5})O_7$ at 600 °C is 1.20×10^{-3} S/cm and 8.74×10^{-4} S/cm respectively, and for the oxides having less cerium $(Ca_{1.5}Ce_{0.25}Ti_{0.25})(Ti_{0.75}Nb_{1.25})O_7$ and $(Ca_{1.5}Ce_{0.25}Ti_{0.25})(Ti_{0.75}Ta_{1.25})O_7$, the conductivity is observed to be 2.35×10^{-7} S/cm and 3.9×10^{-7} S/cm respectively.

4.1.3.7 NTC thermistor characteristics

The NTC thermistor is a thermal sensitive resistor, in which, as a semiconductor, the resistance decreases with increase in temperature. Electrical resistance of NTC thermistors can be described by the following equation:

$$R = R_0 \exp(\beta / T) \qquad (4.1.4) \qquad \text{and} \qquad \beta = \frac{E_a}{K_B} \qquad (4.1.5)$$

where R_0 is a prefactor, E_a is the activation energy, and k_B is the Boltzmann constant. The activation energy is controlled by the conduction mechanism that can be either excitation in a band structure or hopping transport between multivalent transition metal cations.

The relation between resistance and temperature for a negative temperature coefficient thermistor is expressed by the following equation [Justin M. Varghese *et al* 2008].

$$R_T = R_N \exp\left[\beta\left(\frac{T_N - T}{TT_N}\right)\right] \qquad (4.1.6)$$

where R_T is the resistance at temperature T, R_N is the resistance at temperature T_N known, and β is a thermistor characteristic parameter. Rewriting and rearranging the terms of equation (4.1.6), β can be derived as follows:

$$\beta = \left[\frac{TT_N}{T_N - T}\right] \ln\left(\frac{R_T}{R_N}\right) \qquad (4.1.7)$$

The thermistor sensitivity is defined by the temperature coefficient of resistance α, which can be expressed as a function of the β parameter, in according to following equation:

$$\alpha = \left(1/R\right)\left[d(R)/dT\right] = -\beta/T^2 \tag{4.1.8}$$

Composition	β (K) [300°C to 600°C]	Sensitivity α (K^{-1})		Activation energy (eV)
		300°C	600°C	
$(Ca_{1.5}Ce_{0.25}Ti_{0.25})(Ti_{0.75}Nb_{1.25})O_7$	*11586	-0.0194	-0.01520	1.60
$(Ca_{1.25}Ce_{0.5}Ti_{0.25})(TiNb)O_7$	10282	-0.0313	-0.01349	1.13
$(CaCe_{0.75}Ti_{0.25})(Ti_{1.25}Nb_{0.75})O_7$	7767	-0.0311	-0.00776	0.62
$(Ca_{0.75}CeTi_{0.25})(Ti_{1.5}Nb_{0.5})O_7$	6546	-0.0262	-0.00654	0.54
$(Ca_{1.5}Ce_{0.25}Ti_{0.25})(Ti_{0.75}Ta_{1.25})O_7$	*9320	-0.0156	-0.01222	1.31
$(Ca_{1.25}Ce_{0.5}Ti_{0.25})(TiTa)O_7$	11556	-0.0352	-0.01516	1.06
$(CaCe_{0.75}Ti_{0.25})(Ti_{1.25}Ta_{0.75})O_7$	7507	-0.0229	-0.00985	0.62
$(Ca_{0.75}CeTi_{0.25})(Ti_{1.5}Ta_{0.5})O_7$	6376	-0.1942	-0.00837	0.53

* Temperature range 500°C to 600°C

Table 4.1.2. β Constant, α and Activation energy for Various Compositions in a Ca-Ce-Ti-M -O system (where M=Nb or Ta)

Considering Arrhenius plot Fig.4.1.11 (a) and (b), α and β parameters were calculated by the above equations. The values are calculated in the temperature range from 300 to 600°C and depicted in Table 4.1.2. The β value

of the different compositions lie in the range of 6000-12000K. The results indicate that the thermistor characteristics can be tuned to the desired value by changing the cerium concentration in the compound. It is observed that these values are in the desirable range of high temperature thermistors [Feltz A. 2000].

4.1.4 Conclusions

In conclusion, we prepared a new series of semiconducting oxides in Ca – Ce – Ti – M – O (M = Nb or Ta) system and its structural, microstructural and electrical conductivity properties were investigated. The powder X-ray diffraction and Raman spectroscopy analyses showed that all these compounds belong to a cubic pyrochlore type structure in the space group *Fd3m*. The semiconductivity in these compounds is due to the presence of Ce^{3+}, which remains in the reduced state without being oxidized to Ce^{4+} by structural stabilization. The presence of Ce^{3+} is further confirmed by the X-ray photoelectron spectroscopy investigations. Impedance spectral studies suggest that the conduction in these compounds is mainly due to electronic contribution. Among the prepared compounds, $(Ca_{0.75}CeTi_{0.25})$ $(Ti_{1.5}M_{0.5})O_7$ (M = Nb or Ta) possesses good NTC behavior over a wide temperature range. Therefore, these semiconducting ceramic oxides may find potential applications in devices like NTC thermistors.

PART II

INFLUENCE OF SINTERING TEMPERATURE ON MICROSTRUCTURE AND ELECTRICAL PROPERTIES OF $(CaCe_{0.75}Ti_{0.25})$ $(Ti_{1.25}M_{0.75})O_7$ AND $(Ca_{0.75}CeTi_{0.25})(Ti_{1.5}M_{0.5})O_7$ (M = Nb or Ta) CERAMICS

4.2.1 Introduction

Microstructure is an important contributing factor to the transport properties of mixed conducting materials [Kharton V.V *et al* 2002]. As well known, the microstructure of ceramic materials, to a great extent, relies on sintering conditions. Thus, the influence of sintering temperature on the microstructure and electrical conducting properties of the ceramics is an intriguing subject of significant importance. Up to date, the research on this topic is comparatively limited. In this work, the microstructure and electrical conducting properties of $(CaCe_{0.75}Ti_{0.25})(Ti_{1.25}M_{0.75})O_7$, and $(Ca_{0.75}CeTi_{0.25})(Ti_{1.5}M_{0.5})O_7$ (where M = Nb or Ta) ceramics were investigated in the sintering temperature interval of 1300–1400°C. Moreover, the microstructural dependence of the electrical properties has also been examined.

4.2.2 Experimental

$(CaCe_{0.75}Ti_{0.25})(Ti_{1.25}M_{0.75})O_7$ and $(Ca_{0.75}CeTi_{0.25})(Ti_{1.5}M_{0.5})O_7$ (where M = Nb or Ta) samples were fabricated by solid-state reaction. The starting powders used are commercially available fine high-purity powders of $CaCO_3$, CeO_2, TiO_2, Nb_2O_5 and Ta_2O_5. Weighed powders were mixed in an agate mortar with acetone as mixing medium. The mixed slurries were dried in an oven at 100°C for 2 h. The powders were calcined in a platinum crucible at 1300°C for 3 h. The calcination was repeated twice with intermittent grinding.

Polyvinyl alcohol (PVA) was then added into the calcined powders and the mixtures were ground in mortar. Subsequently, the mixed powders were pressed at a pressure of 250 MPa to prepare pellets of 2mm thick and 10mm in diameter. The green compacts were heated in air to 600°C and were kept at that temperature for 1 h to remove the organic binder. Then, they were sintered at 1300°C, 1350°C or 1400°C for 9h.

The crystal structure of as-sintered samples $(CaCe_{0.75}Ti_{0.25})(Ti_{1.25}M_{0.75})O_7$ and $(Ca_{0.75}CeTi_{0.25})(Ti_{1.5}M_{0.5})O_7$ (where M = Nb or Ta) was analyzed with a Phillips X'pert Diffractometer (Eindhoven, The Netherlands) using Cu Kα radiation at 40 kV and 25mA. The microstructure of the samples was investigated using a scanning electron microscope JEOL JSM 5600 (Tokyo, Japan). Silver (Ag) paste was spread on opposite-side surfaces of the sintered samples. After the pastes were dried at room temperature, the samples were heated at 600°C for 30 min. Three samples of each composition with different sintering temperatures were prepared for measuring electrical resistance. The samples were electroded by attaching silver wires to silvered surfaces. The conductivity was measured in a temperature range of 45 to 600°C using a high resolution digital multimeter (Philips, PM 2525 multimeter). The readings were recorded with a slow heating after equilibrating the pellet for 2 min at each measuring temperature.

4.2.3 Results and discussion

4.2.3.1 XRD and structure

The crystal structure of the $(CaCe_{0.75}Ti_{0.25})(Ti_{1.25}M_{0.75})O_7$ and $(Ca_{0.75}CeTi_{0.25})(Ti_{1.5}M_{0.5})O_7$ (where M = Nb or Ta) samples sintered at 1300°C/9h, 1350°C/9h, 1400°C/9h were analyzed by XRD. The XRD patterns of the compositions are shown in Fig. 4.2.1 and Fig.4.2.2.

The powder diffraction pattern confirms that phase present in the sintered bodies was solid solution of the constituent oxides with a cubic pyrochlore structure having the space group *Fd3m*. No phase transition or decomposition is observed with increase in sintering temperature. The diffraction peaks are becoming sharper indicating high crystallinity with increase in sintering temperature from 1300°C to 1400°C.
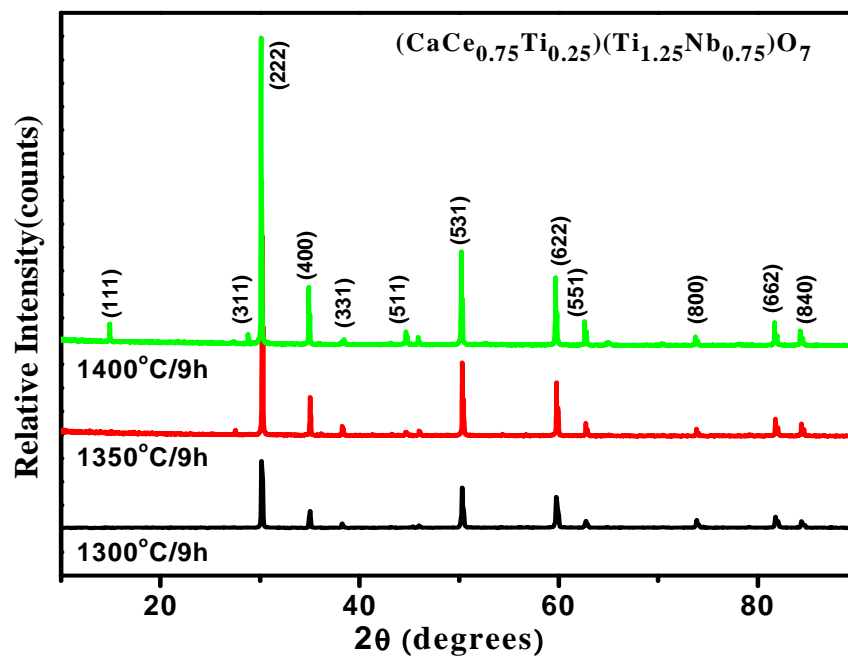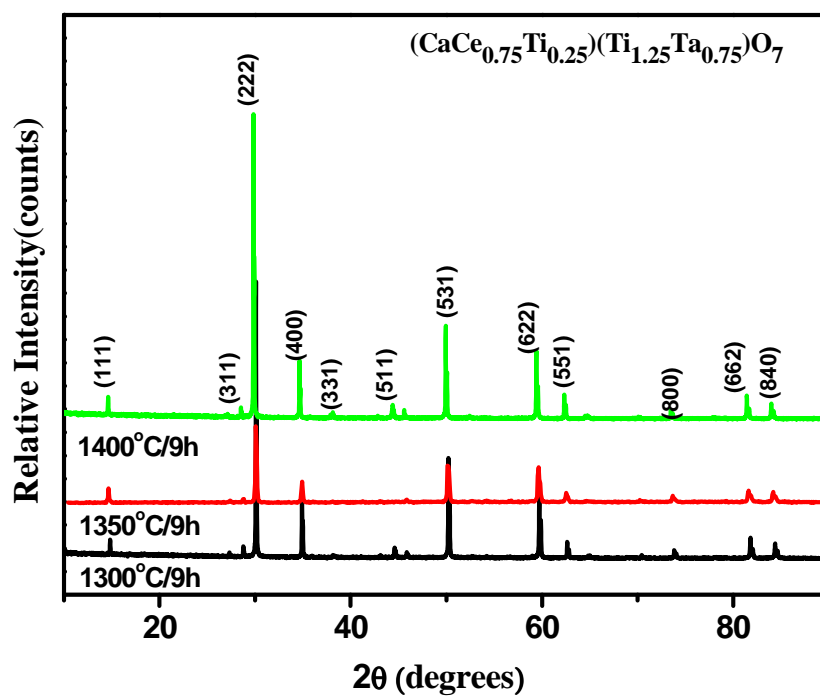
Fig. 4.2.1 Powder X-ray diffraction patterns for (a) $(CaCe_{0.75}Ti_{0.25})(Ti_{1.25}Nb_{0.75})O_7$ (b) $(CaCe_{0.75}Ti_{0.25})(Ti_{1.25}Ta_{0.75})O_7$.
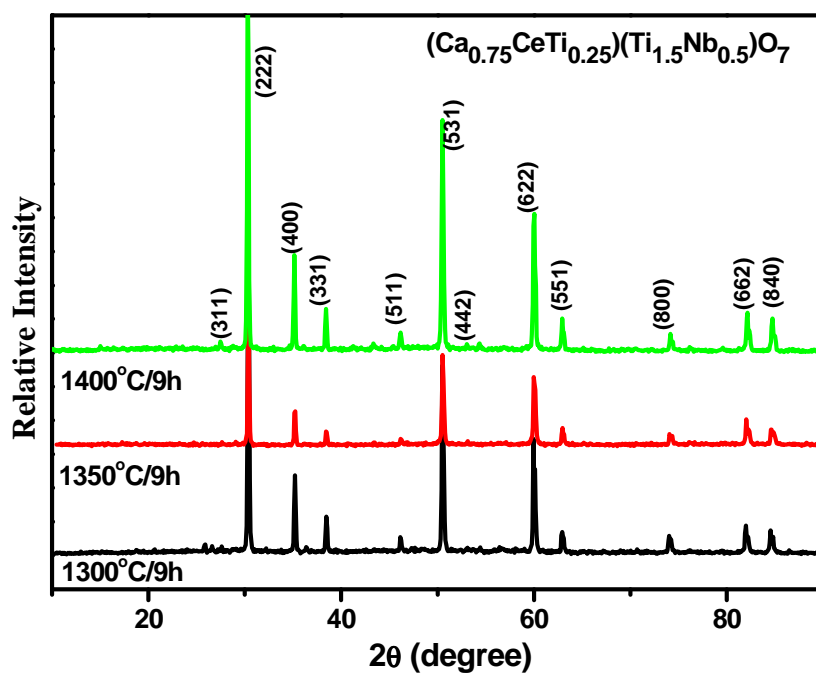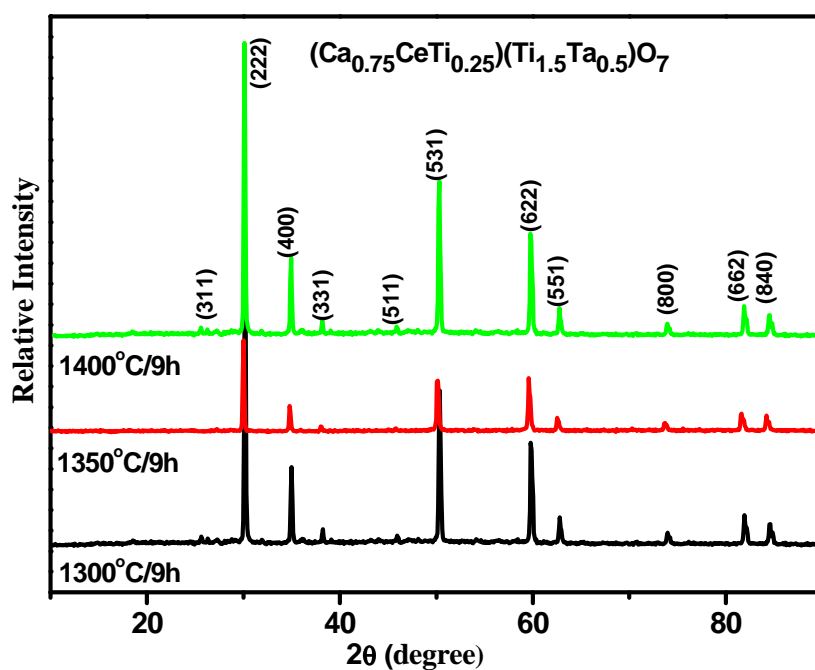
Fig. 4.2.2 Powder X-ray diffraction patterns for (a)
$(Ca_{0.75}CeTi_{0.25})(Ti_{1.5}Nb_{0.5})O_7$ (b)$(Ca_{0.75}CeTi_{0.25})(Ti_{1.5}Ta_{0.5})O_7$.

4.2.3.2 Scanning electron microscopy and microstructure

The SEM images obtained from the surface of the sintered pellets at three different temperatures: 1300°C/9h, 1350°C/9h, 1400°C/9h of the $(CaCe_{0.75}Ti_{0.25})(Ti_{1.25}M_{0.75})O_7$ and $(Ca_{0.75}CeTi_{0.25})(Ti_{1.5}M_{0.5})O_7$ (where M=Nb or Ta) samples are shown in Figures 4.2.3 - 4.2.6. The samples were microscopically homogeneous and highly dense. The density of the samples found to be dependent on sintering temperature. The density of the compositions improved with increase in sintering temperature. A dense microstructure is necessary to consistently reproduce the electrical characteristics of the ceramics.
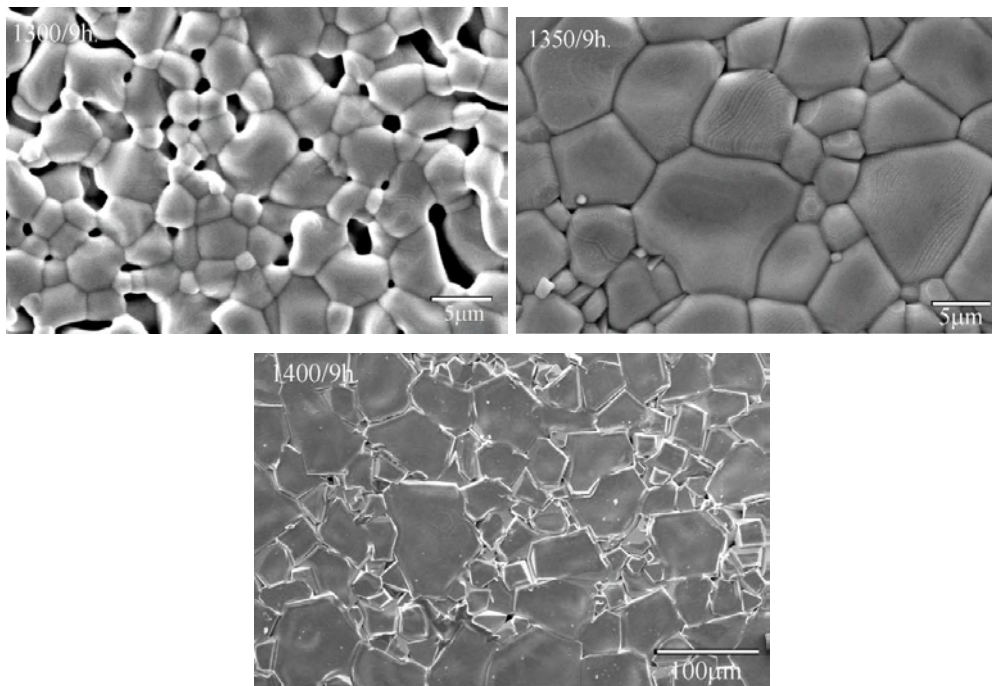
Fig. 4.2.3 Scanning electron micrographs of $(CaCe_{0.75}Ti_{0.25})(Ti_{1.25}Nb_{0.75})O_7$ at different sintering temperatures.

On close observation of the micrographs we can see that in $(CaCe_{0.75}Ti_{0.25})(Ti_{1.25}Nb_{0.75})O_7$ composition for 1300°C/9h sintering results in a porous microstructure with an average grain size of 3-4μm. The grain growth increases with increase in temperature. The 1350°C/9h sintering results in a microstructure with uniform grains having well defined grain boundaries. The average grain size is found to be 5-6μm. On further increase in sintering temperature to 1400°C/9h gives rise to very large grains and the grain size shows a large variation from 10μm to 100μm. The grains are arranged in such a manner that the big grains are surrounded by small grains.
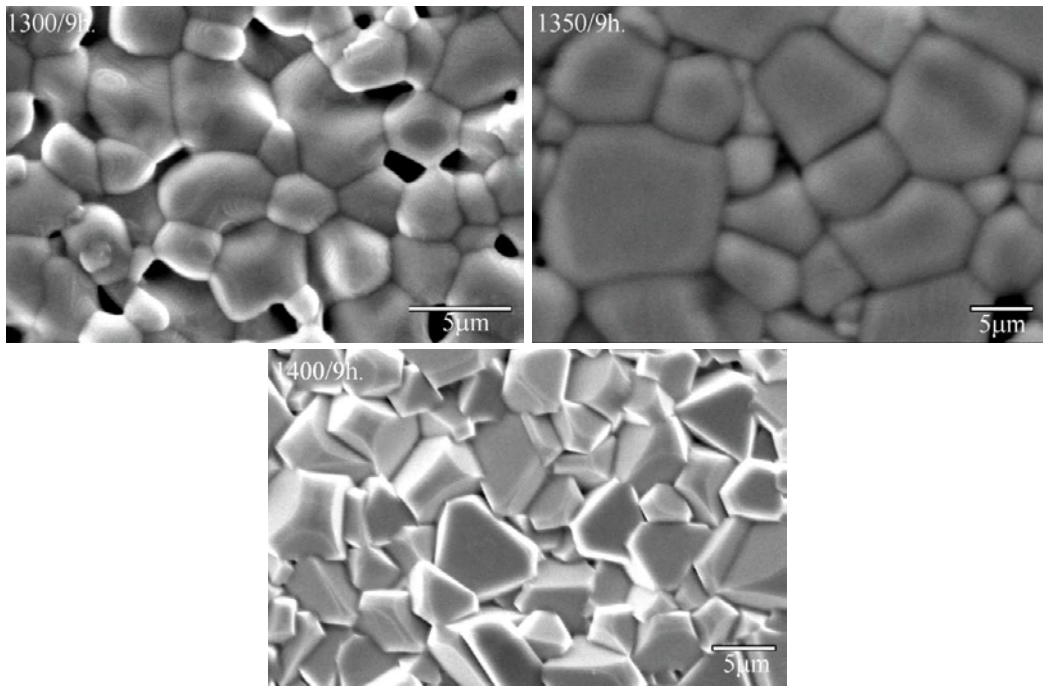
Fig. 4.2.4 Scanning electron micrographs of $(CaCe_{0.75}Ti_{0.25})(Ti_{1.25}Ta_{0.75})O_7$ at different sintering temperatures.

In $(CaCe_{0.75}Ti_{0.25})(Ti_{1.25}Ta_{0.75})O_7$ composition both 1300°C/9h and 1350°C/9h sintering results in porous microstructures. The porosity decreases with increase in sintering temperature. The 1400°/9h sintering yields a highly dense microstructure with average grain size of 4-5µm.
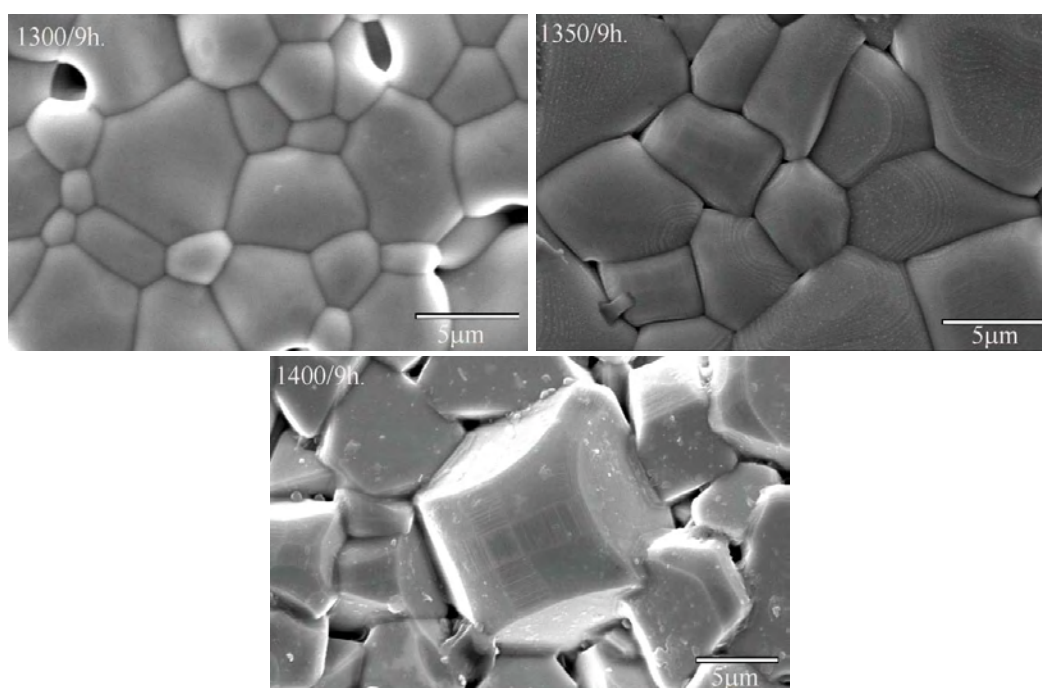
Fig.4.2.5 Scanning electron micrographs of $(Ca_{0.75}CeTi_{0.25})(Ti_{1.5}Nb_{0.5})O_7$ at different sintering temperatures.

The $(Ca_{0.75}CeTi_{0.25})(Ti_{1.5}Nb_{0.5})O_7$ shows better densification in comparison with $(CaCe_{0.75}Ti_{0.25})(Ti_{1.25}Nb_{0.75})O_7$ composition. Here the 1350°C/9h sintered sample exhibits very good microstructure having uniform grains and well defined grain- grain interface. The 1300°C/9h sintered

composition exhibits a little porosity while the 1400°C/9h sintered composition contains sharp edged grains with different size and shape.
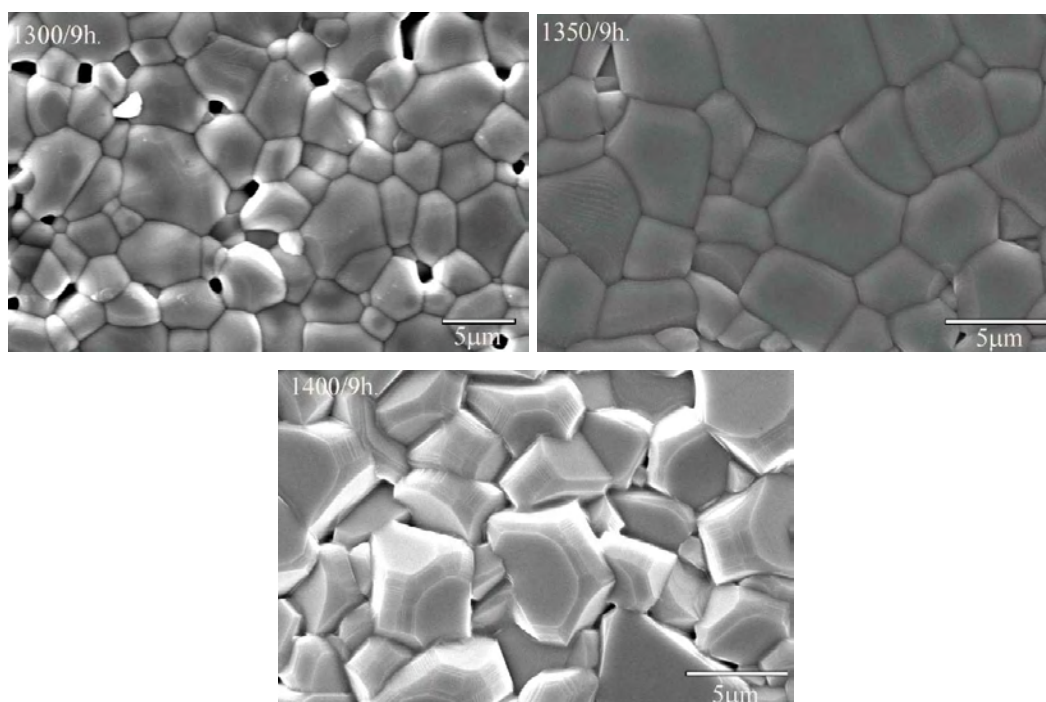
Fig.4.2.6 Scanning electron micrographs of $(Ca_{0.75}CeTi_{0.25})(Ti_{1.5}Ta_{0.5})O_7$ at different sintering temperatures.

Here the 1300°C/9h sintered tantalate gives more porous behaviour in comparison with the niobate. The compound sintered at 1350°C/9h displays well grown grains with defined grain boundaries. The 1400°C/9h sintered composition contains sharp edged grains with an average size of 5-6μm.

4.2.3.3 Electrical conductivity

The electrical conductivity data of the above compounds reveals that they are semiconducting in nature. Fig. 4.2.7 and Fig. 4.2.8 show the electrical

conductivity (log σ) as a function of absolute temperature ($1000/T$). The nature of variation obeys the Arrehnius equation $\sigma = \sigma_0 \exp(-Ea/K_B T)$ where Ea is the activation energy, K_B is the Boltzmann constant, T is the absolute temperature and σ_0 is the pre-exponential factor. The activation energies of conduction are calculated from the slopes of the plots in the temperature range of 300^oC to 600^oC and are listed in Table 4.2.1.

The electrical conductivity exhibits a strong dependency on microstructure in particularly the morphology of the grains. The conductivity data in the present work indicate an obvious sensitivity of the electrical conducting properties to sintering temperature for both $(Ca_{0.75}CeTi_{0.25})(Ti_{1.5}M_{0.5})O_7$ and $(CaCe_{0.75}Ti_{0.25})(Ti_{1.25}M_{0.75})O_7$ ceramics. This phenomenon can be qualitatively interpreted with respect to the microstructural evolution with sintering temperature. The enhancement of electrical conducting properties with sintering temperature from 1300°C to 1350°C is reasonably ascribed to the densification development of the ceramic [Hernandez T and Martın P 2007]. At higher sintering temperatures, the facilitated grain growth resulted in non uniform grain morphologies in certain compositions. This resulted in a complicated effect on the microstructure and consequently electrical conductivity.
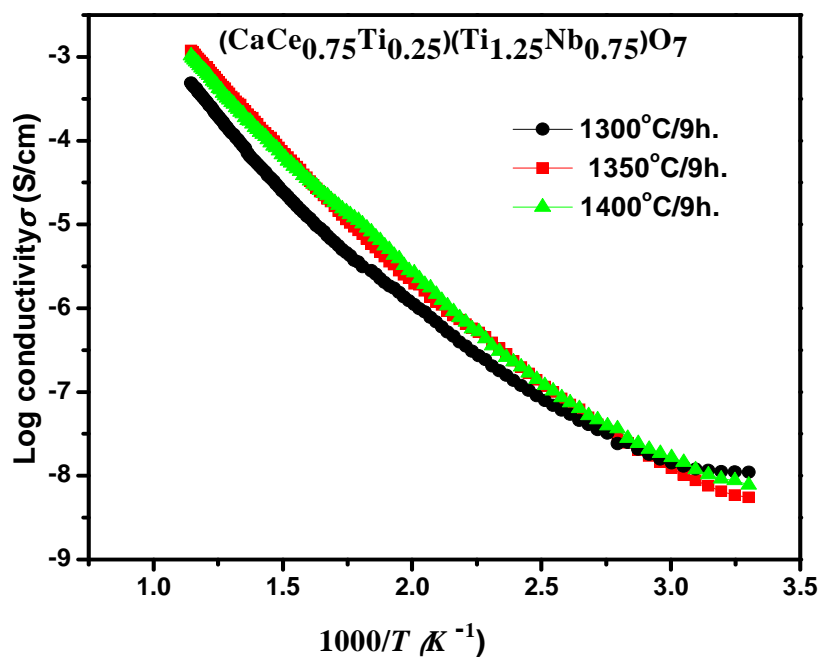
(a)
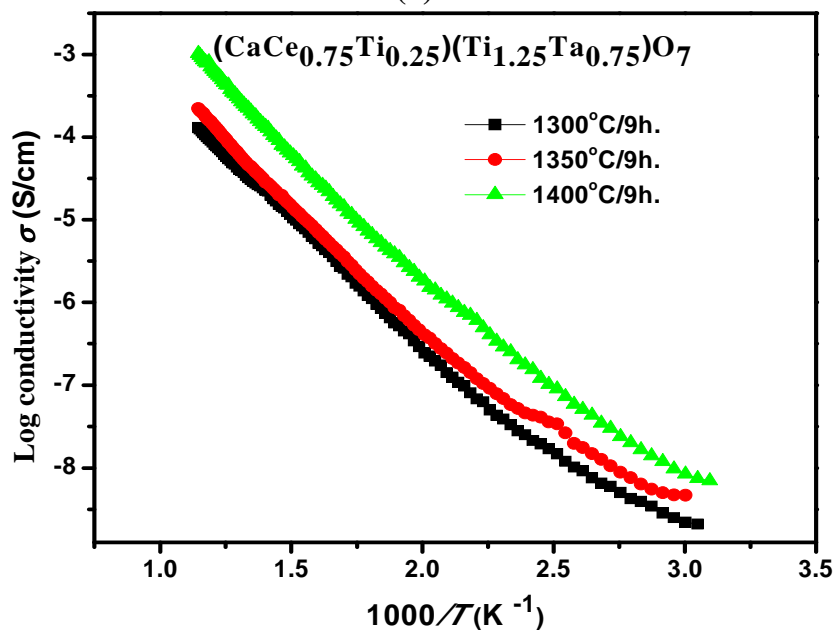
(b)

Fig. 4.2.7 Variation of log conductivity (σ) vs. reciprocal of temperature for (a) $(CaCe_{0.75}Ti_{0.25})(Ti_{1.25}Nb_{0.75})O_7$ (b) $(CaCe_{0.75}Ti_{0.25})(Ti_{1.25}Ta_{0.75})O_7$.

The variation of electrical conductivity as a function of 1000/T for (a) $CaCe_{0.75}Ti_{0.25})(Ti_{1.25}Nb_{0.75})O_7$ and (b) $(CaCe_{0.75}Ti_{0.25})(Ti_{1.25}Ta_{0.75})O_7$ is shown in Fig.4.2.7. In $(CaCe_{0.75}Ti_{0.25})(Ti_{1.25}Ta_{0.75})O_7$ composition the increase of sintering temperature promoted grain growth and microstructural densification consequently the electrical conductivity increases in the same manner. In $(CaCe_{0.75}Ti_{0.25})(Ti_{1.25}Nb_{0.75})O_7$, the grain growth increases with increase in temperature and at 1350°C/9h sintering results in a dense microstructure having uniform grain morphology. On further increase in sintering temperature gives rise to very large grains and the grain size shows a large variation from 10μm to 100μm. The grains are arranged in such a manner that the big grains are surrounded by small grains. Even though very large grains are been formed with 1400°C/9h sintering there is no increase in conductivity as observed from that of 1350°C/9h sintered composition. Hence we can conclude that the microstructure having well grown grains with uniform size and shape possessing good grain-grain interface favours the conduction of electrons.
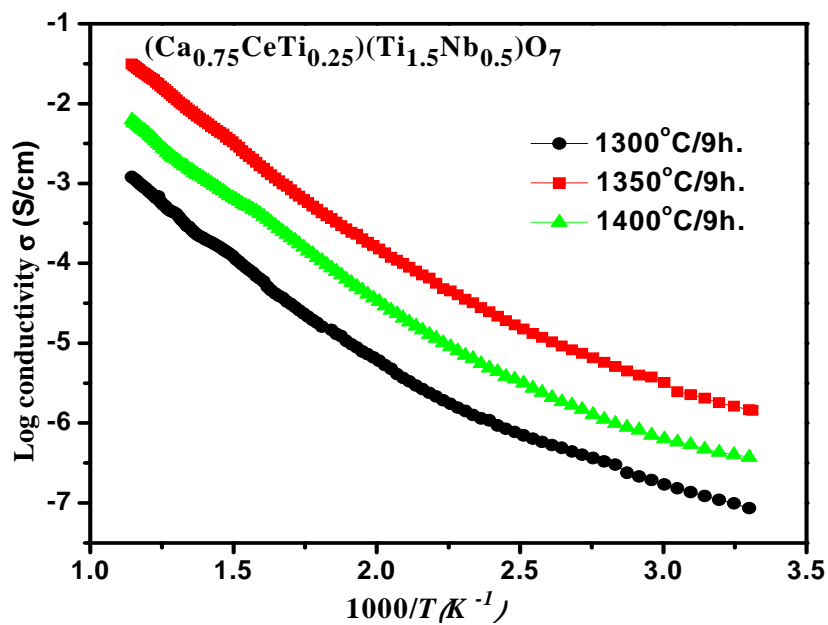
(a)
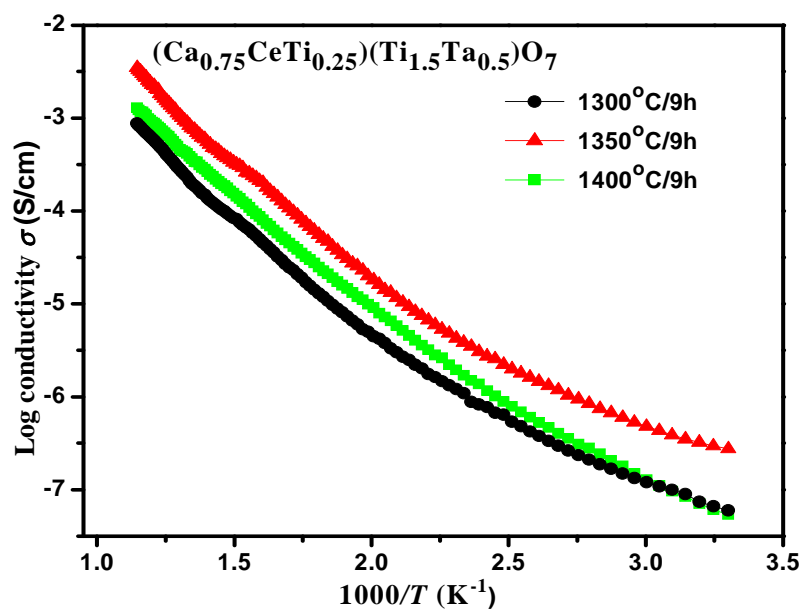
(b)

Fig. 4.2.8 Variation of log conductivity (σ) vs. reciprocal of temperature for (a) $(Ca_{0.75}CeTi_{0.25})(Ti_{1.5}Nb_{0.5})O_7$ (b) $(Ca_{0.75}CeTi_{0.25})(Ti_{1.5}Ta_{0.5})O_7$.

Fig. 4.2.8 shows the variation of electrical conductivity as a function of 1000/T for (a) $(Ca_{0.75}CeTi_{0.25})(Ti_{1.5}Nb_{0.5})O_7$ and (b) $(Ca_{0.75}CeTi_{0.25})(Ti_{1.5}Ta_{0.5})O_7$. Here 1350°C/9h sintering yields in maximum conductivity. This can be explained as follows: The increase of sintering temperature promoted grain growth and microstructural densification. The 1300°C/9h sintered composition exhibits a little porosity, which in turn affect the easy flow of electrons and hence reducing the conductivity. While the 1400°C/9h sintered composition contains sharp edged grains with much different size and shape with less connectivity among grains. The grain size and mechanical connection between grains are expected to play an important role in the electronic conduction. It is known that the resistivity is mostly influenced by the presence of grain boundary which acts as region of enhanced scattering for the conduction electrons [Lei L.W.*et al* 2006]. In effect a reduction in conductivity is observed for the 1400°C/9h sintered microstructure. The 1350°C/9h sintering is found to be the optimum sintering temperature for these compositions. The microstructure shows well grown grains with well defined grain-grain interface allowing a highly conductive path for the electron flow. It benefits the conduction of electric charge carriers and is thus responsible for the improvement of the conductivity.

Therefore, a close relation between the microstructure and electrical conducting properties can be suggested. One can conclude that it is crucial to adequately control the sintering temperature of ceramic in order to achieve desired microstructure and optimum electrical conducting properties. In terms of the electrical conducting properties, sintering at 1350°C/9h is optimum for $(Ca_{0.75}CeTi_{0.25})(Ti_{1.5}M_{0.5})O_7$ and $(CaCe_{0.75}Ti_{0.25})(Ti_{1.25}M_{0.75})O_7$ (where M = Nb or Ta) ceramic, producing a generally uniform microstructure.

4.2.3.4 NTC thermistor parameters

The main electrical characteristic of NTC thermistors is their thermistor constant or sensitivity index (β-value) and temperature coefficient of resistance (α). The thermistor constant (β-value) is calculated using the following equation:

$$\beta = \left[\frac{TT_N}{T_N - T}\right] \ln\left(\frac{R_T}{R_N}\right) \tag{4.2.1}$$

where R_T is the resistance at temperature T, R_N is the resistance at temperature T_N known, and β is a thermistor characteristic parameter.

Compound	Sintering Temperature (°C)	Relative Density	β (K)	Sensitivity α	
				300°C (K^{-1})	600°C (K^{-1})
(CaCe$_{0.75}$Ti$_{0.25}$)(Ti$_{1.25}$Nb$_{0.75}$)O$_7$	1300	85	7732	-0.0235	-0.010150
	1350	92	7767	-0.0311	-0.007764
	1400	93	7136	-0.0217	-0.009363
(CaCe$_{0.75}$Ti$_{0.25}$)(Ti$_{1.25}$Ta$_{0.75}$)O$_7$	1300	75	7229	-0.0220	-0.009485
	1350	91	7507	-0.0229	-0.009851
	1400	96	7703	-0.0235	-0.010102
(Ca$_{0.75}$CeTi$_{0.25}$)(Ti$_{1.5}$Nb$_{0.5}$)O$_7$	1300	88	6503	-0.0198	-0.008533
	1350	91	6546	-0.0199	-0.008509
	1400	92	6105	-0.0186	-0.008010
(Ca$_{0.75}$CeTi$_{0.25}$)(Ti$_{1.5}$Ta$_{0.5}$)O$_7$	1300	77	6009	-0.0183	-0.007884
	1350	90	6376	-0.0194	-0.008366
	1400	96	6271	-0.0191	-0.008228

Table 4.2.1 β Constant, Density and α for (Ca$_{0.75}$CeTi$_{0.25}$)(Ti$_{1.5}$M$_{0.5}$)O$_7$ and (CaCe$_{0.75}$Ti$_{0.25}$)(Ti$_{1.25}$M$_{0.75}$)O$_7$ (where M=Nb or Ta)

The thermistor sensitivity is defined by the temperature coefficient of resistance α, which can be expressed as a function of the β parameter, in according to following equation:

$$\alpha = \left(1/R\right)\left[d(R)/dT\right] = -\beta/T^2 \qquad (4.2.2)$$

The α and β parameters were calculated by the above equations. The results obtained for various compositions developed are summarized in Table 4.2.1. The values are calculated in the temperature range from 300 to 600°C

and depicted in Table 4.2.1. The β value of the different compositions lie in the range of 5000-7000K.

4.4 Conclusions

The microstructure and electrical conducting properties of $(CaCe_{0.75}Ti_{0.25})$ $(Ti_{1.25}M_{0.75})O_7$, $(Ca_{0.75}CeTi_{0.25})(Ti_{1.5}M_{0.5})O_7$ (where M = Nb or Ta) ceramics have been investigated in the sintering temperature range of 1300–1400°C. It has been determined that the microstructure evolution is responsible for the variation in the electrical conducting properties with sintering temperature. It is important to adequately control the sintering temperature to obtain desired microstructure and optimum electrical conducting properties. The preferred sintering temperature of these compounds was determined to be 1350°C/9h with regard to the electrical conducting properties. Compositions sintered at 1350°C/9h present generally uniform microstructure.

CHAPTER 5

ENHANCEMENT OF NTC THERMISTOR CHARACTERISTICS BY RARE EARTH (Gd, Sm AND Y) DOPING IN $(Ca_{0.75}CeTi_{0.25})(Ti_{1.5}Ta_{0.5})O_7$ PYROCHLORE

5.1 Introduction

Along with the advances in modern technology, demand for precise temperature measurement and control has been increased. Ceramic thermistors (thermally sensitive resistors) show promising potential for such applications. Thermistor materials find a variety of applications such as temperature sensors [Scarr R.W.A and Setterington R.A 1960] and infrared radiation detector sensors [Astheimer W and Wormser E.M 1959]. NTC ceramics generally made up of transition metal oxides which have specific advantages such as simpler and cost effective process, scope for tailorability of electrical properties namely electrical resistivity (ρ) and temperature coefficient of resistance (TCR) and easy adaptability to current day thin film processing techniques [Ayer Jr. W.J and Rose K. 1973]. As a result they have been attracting the attention of various investigators. Usually the applications of thermistors are limited to temperatures below 300°C due to their instability and changing electrical characteristics [Feltz A 2000]. Therefore, there is a need for the development of new materials which have good electrical characteristics at high temperatures. The present chapter deals with the synthesis and characterization of rare earth doped semiconducting ceramic oxides in $(Ca_{0.75}Ce_{1-x}RE_xTi_{0.25})(Ti_{1.5}Ta_{0.5})O_7$ (RE = Gd, Sm, Y; x = 0, 0.25, 0.5, 0.75) system partial substitutions of rare earths Gd, Sm and Y as an additional

variation is expected to extend the possibilities for selecting suitable compositions with desired values of the electrical properties. Further it is expected that the rare earth substitution may improve the thermistor parameters of $(Ca_{0.75}CeTi_{0.25})(Ti_{1.5}Ta_{0.5})O_7$ for its application as a high temperature thermistor. Therefore, variations of the Gd, Sm and Y concentration are carried out in the limits $0<x<1$.

5.2 Experimental

The compounds in $(Ca_{0.75}Ce_{1-x}RE_xTi_{0.25})(Ti_{1.5}Ta_{0.5})O_7$ (RE = Gd, Sm, Y; $x = 0, 0.25, 0.5, 0.75$) system were prepared by solid-state route. High-purity $CaCO_3$, CeO_2, TiO_2, Nb_2O_5, Sm_2O_3, Gd_2O_3 and Y_2O_3 powders were used (99.9%, Acros Organics, Geel, Belgium). In order to study the effect of composition and microstructure on the electrical properties of $Ca_{0.75}Ce_{1-x}RE_xTi_{1.75}Ta_{0.5}O_7$ (RE = Gd, Sm, Y; $x=0, 0.25, 0.5, 0.75$) NTC thermistors, various samples with different compositions were fabricated. The stoichiometric amount of the precursor oxides were weighed and thoroughly wet mixed in agate mortar with acetone as the wetting medium and dried by keeping in a hot air oven at 100^oC. The mixed product was calcined at 1300^oC for 3h in air. The calcination was repeated twice with intermittent grinding. The calcined powder was then mixed with 4 wt% of polyvinyl alcohol (PVA; hydrolysis level 85-88%) solution. PVA acts as a binder and provides

mechanical strength to the pressed samples. The powder was pelletized into cylindrical pellets with a diameter of 10 mm and thickness around 1-2 mm using a hydraulic press by applying a pressure of 250 MPa. The green compacts were heated at 600 ^{o}C for 1h to burn off the PVA and were then sintered at 1350°C for 9 h in air. The phase purity of the sintered samples was characterized using a Phillips X'Pert-Pro diffractometer (Eindhoven, The Netherlands), under the following conditions: Ni-filtered Cu-Kα radiation, tube power 40kV, 30mA receiving slit 0.2mm, and a graphite monochromator. The powder patterns were recorded at room temperature in the angular range from $2\theta = 10^o$ to 90°. The microstructure of the samples was observed on polished surfaces using JEOL (JSM 5600) scanning electron microscope. For electrical measurements the pellets were painted on both sides with silver paste and were then cured for 30 min at 600°C and electroded with silver wires. Impedance measurements of the pellets were carried out; from 30 to 800 $^\circ$C in the frequency range 10 Hz to 1 MHz using a computer controlled impedance analyzer (Solartron, SI 1260). The dc conductivity with respect to temperature was measured using a high resolution digital multimeter, (Philips, PM 2525 multimeter). The conductivity was measured in a temperature range of 30°C to 800°C in steps of 5°C

5.3. Results and discussion

5.3.1 X-ray diffraction analysis
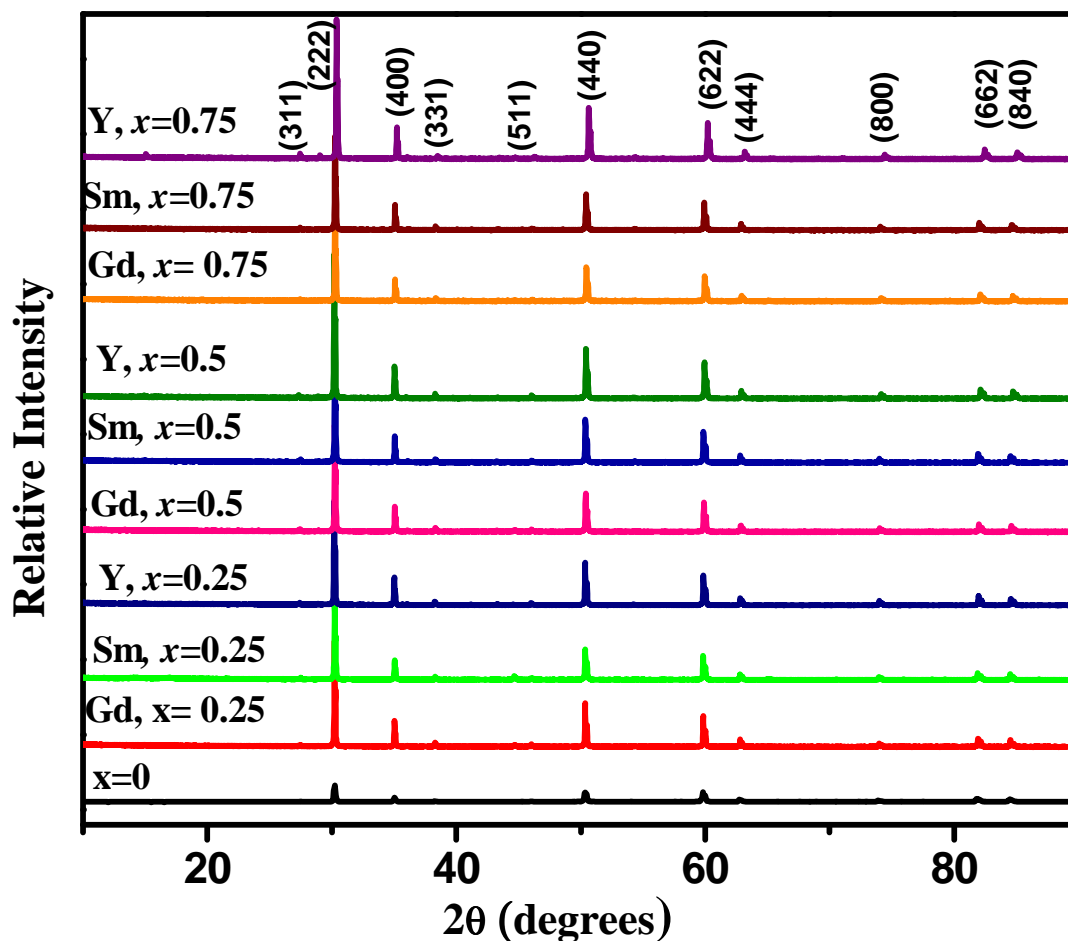
Fig. 5.1 Powder X-ray diffraction patterns of $(Ca_{0.75}Ce_{1-x}RE_xTi_{0.25})(Ti_{1.5}Ta_{0.5})O_7$ (RE = Gd, Sm, Y; x = 0, 0.25, 0.5, 0.75).

The room temperature XRD patterns of the samples sintered at 1350°C are shown in Fig 5.1. The nature of XRD patterns appears to confirm the formation of single-phase with cubic crystal structure of the compounds.

All the reflection peaks were indexed with cubic pyrochlore structure having F$d3m$ the space group. The reflections are typical of the cubic pyrochlore type structure, which is characterized by the presence of typical super-lattice peaks at 2Θ ~ 14° (111), 28° (311), 37° (331) and 45° (511). The sharp and intense peaks of the patterns indicate the crystalline nature of the samples.

5.3.2 Scanning electron microscopic studies

The SEM micrographs recorded from thermally etched surface (1325°C/30 min) of the sintered pellets are shown in Figs. 5.2, 5.3, 5.4.
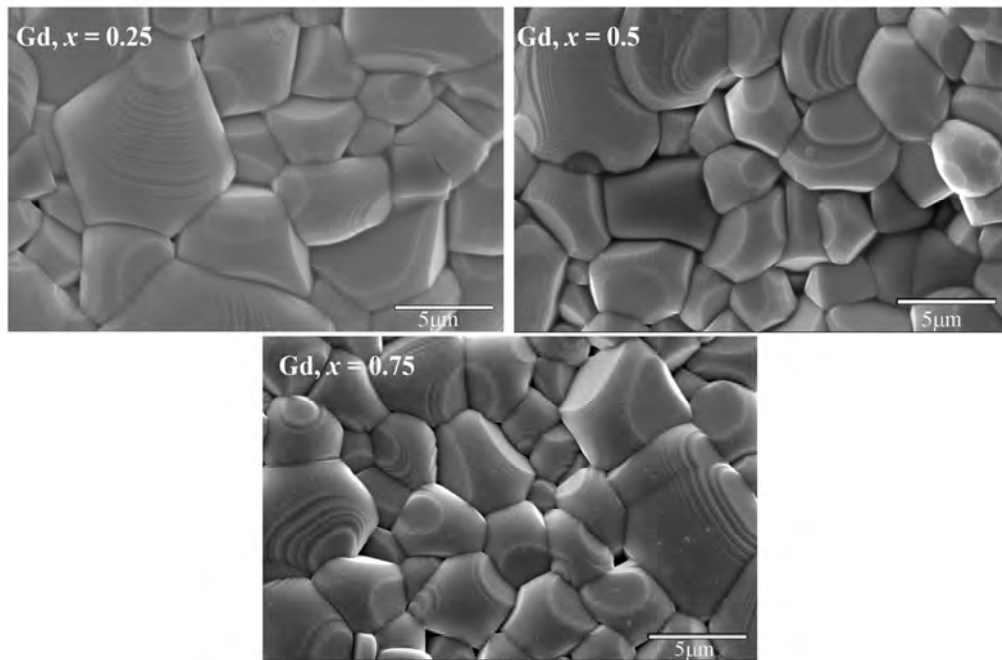
Fig. 5.2 Typical scanning electron micrographs of $(Ca_{0.75}Ce_{1-x}Gd_xTi_{0.25})(Ti_{1.5}Ta_{0.5})O_7$ ($x = 0.25, 0.5, 0.75$).
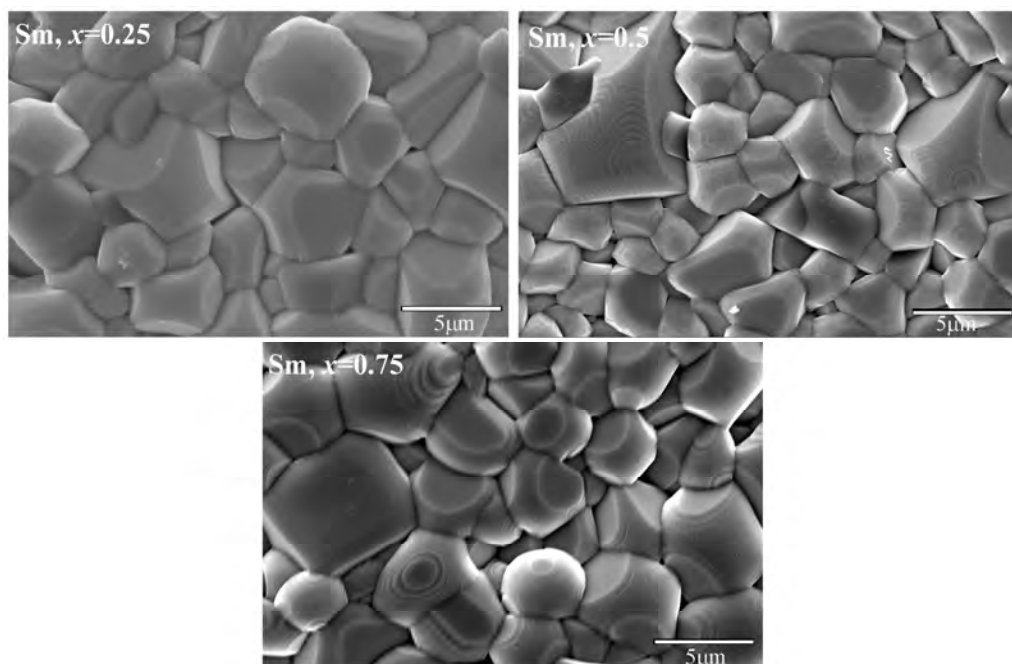
Fig. 5.3 Typical scanning electron micrographs of $(Ca_{0.75}Ce_{1-x}Sm_xTi_{0.25})(Ti_{1.5}Ta_{0.5})O_7$ ($x = 0.25$, 0.5, 0.75).
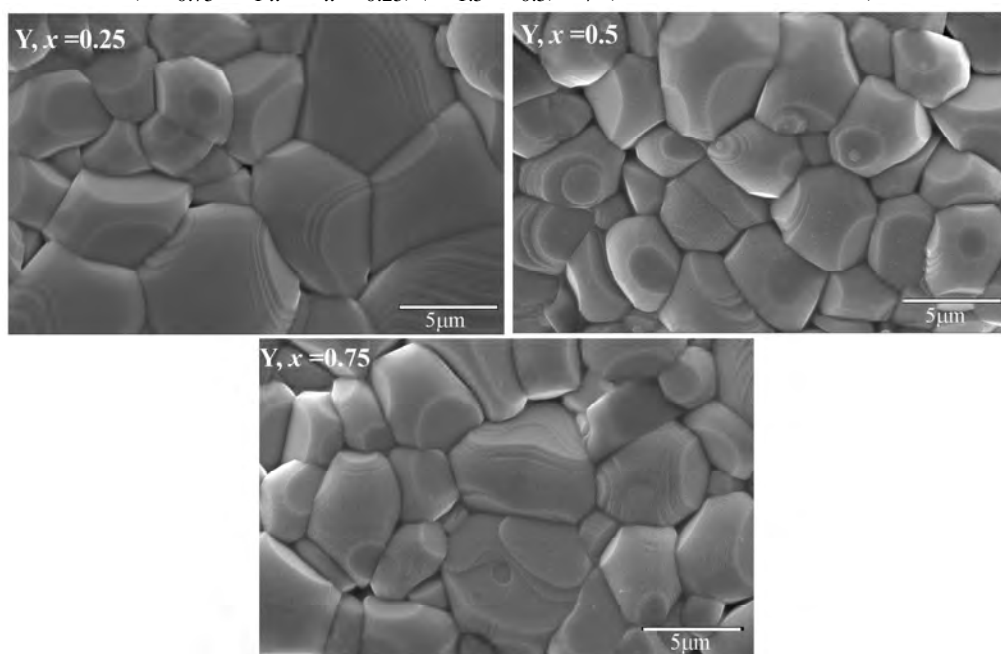
Fig. 5.4 Typical scanning electron micrographs of $(Ca_{0.75}Ce_{1-x}Y_xTi_{0.25})(Ti_{1.5}Ta_{0.5})O_7$ ($x = 0.25$, 0.5, 0.75).

All the compounds show well-sintered and well grown grains in the 1–5 μm size range with almost the same morphological appearance. The microstructure of all the sintered compounds reveals well-grown grains with less porosity. The density is observed to be in the range of 94-97%. The grain size is found to be decreasing with increase in rare earth concentration.

5.3.3 Impedance spectral measurements

Complex impedance spectroscopy (CIS) [Macdonald J.R 1987] is a technique that enables us to separate the real and imaginary component of the complex electrical parameters so as to get the true picture of material properties. It is used to characterize electrical properties of some electronic and/or ionic materials. The technique is based on analyzing the ac response of a system to a sinusoidal perturbation and subsequent of impedance as a function of frequency of perturbation. The frequency dependent properties of a material can be obtained from complex impedance (Z^*), electric modulus (M^*), complex dielectric constant (ε^*) and tangent loss (tan δ), which are related to each other. The impedance measurements were carried out for all the samples in the frequency range of 10 Hz to 1 MHz and in the temperature range of 30 to 800°C. The impedance spectra of $(Ca_{0.75}Ce_{1-x}RE_xTi_{0.25})(Ti_{1.5}Ta_{0.5})O_7$ (x = 0.25, 0.5) are only discussed since the x = 0.75

concentration exhibit very high resistance which is beyond the scope of the instrument for measurement in the temperature range of 30 to 400 °C.

The variation of Z' with log frequency at different temperatures of $(Ca_{0.75}Ce_{1-x}RE_xTi_{0.25})(Ti_{1.5}Ta_{0.5})O_7$ (RE = Gd, Sm, Y; x = 0.25, 0.5) is shown in Fig. 5.5. These figures demonstrate that the value of Z' is larger in the low frequency range and gets a monotonous decrease with rise in frequency. It may be due to the effect of polarization in the samples. Interestingly, the magnitude of Z' is found to decrease with the rise in temperature (as shown in Fig. 5.5) which suggests the typical negative temperature coefficient of resistance (NTCR) type behavior of the material, usually observed in semiconductors. In the high frequency range, all the curves merge at a very low value so that Z' appears to become independent of both the frequency and temperature. It indicates a possible release of space charge [Plocharski J *et al* 1988; Srinivas K *et al* 2003; Rangaraju M.R *et al* 2004]. The resistance is strongly affected by the variation of temperature (Fig. 5.5). The increase in frequency also decreases the resistance magnitude significantly. The resistance magnitudes coincide above a certain frequency irrespective of the temperature variation.
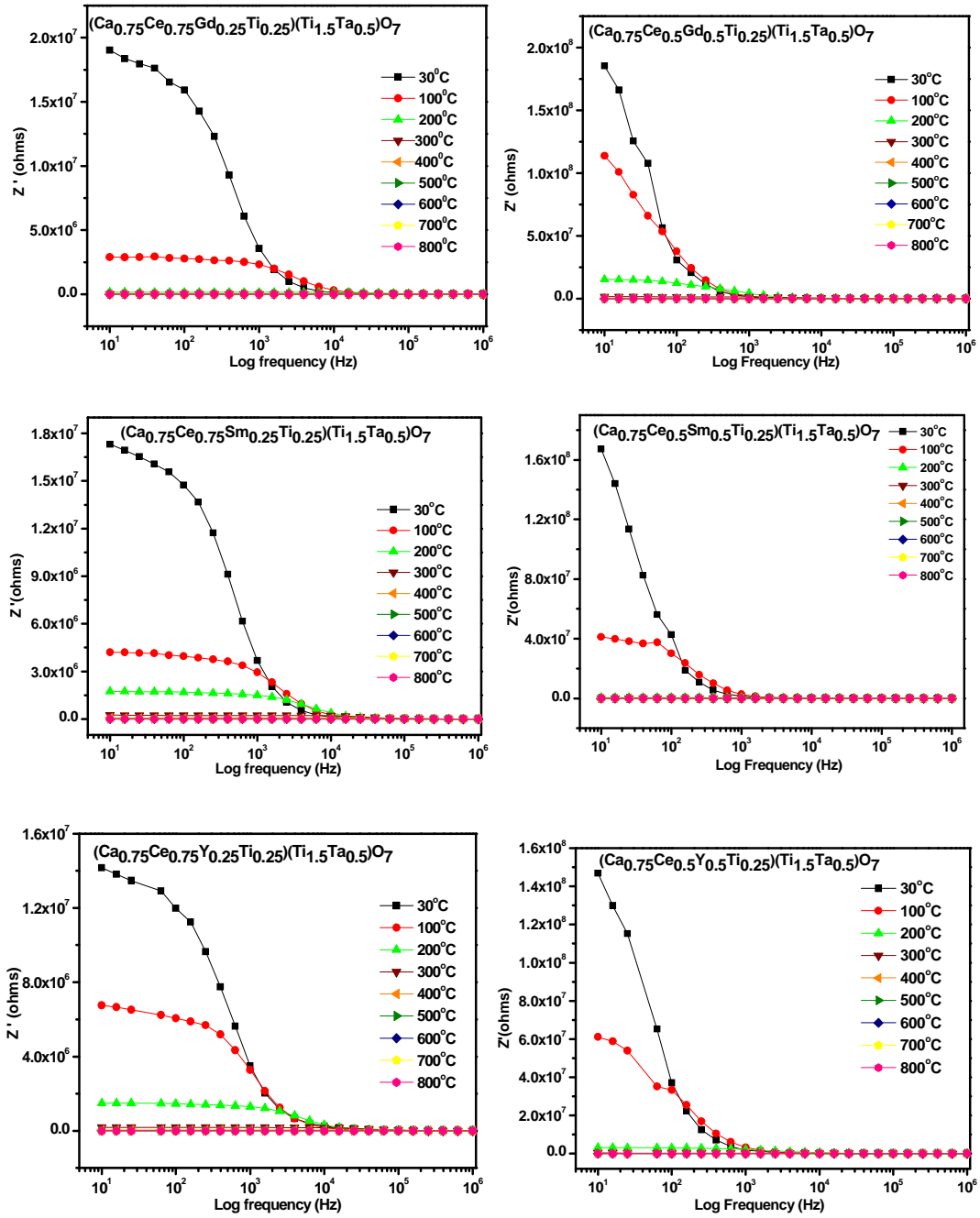
Fig. 5.5 Impedance curves of real (Z') component as a function of log frequency at various temperatures for $(Ca_{0.75}Ce_{1-x}RE_xTi_{0.25})(Ti_{1.5}Ta_{0.5})O_7$ (RE = Gd, Sm, Y; $x = 0.25, 0.5$).
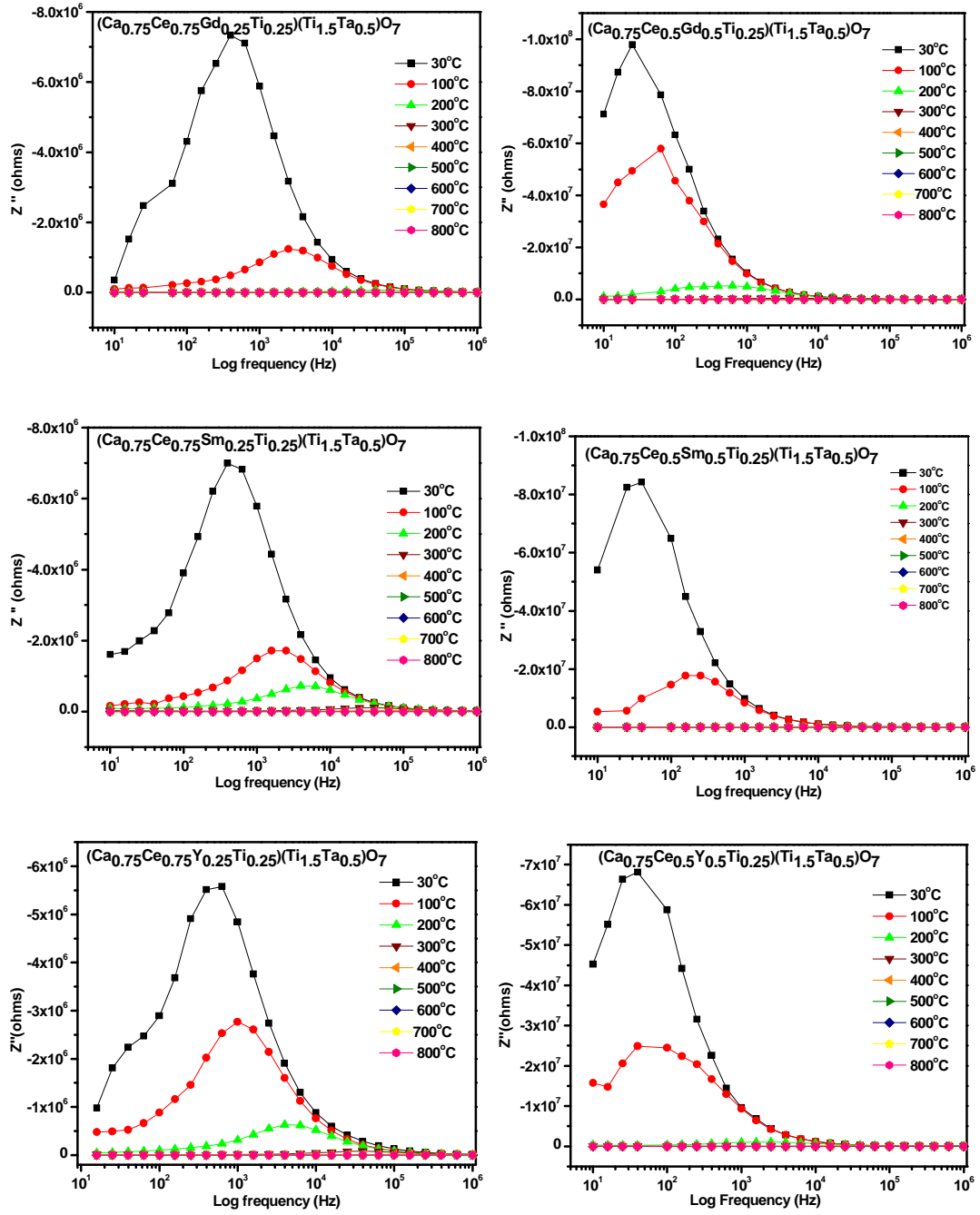
Fig. 5.6 Impedance curves of imaginary (Z″) component as a function of log frequency at various temperatures for $(Ca_{0.75}Ce_{1-x}RE_xTi_{0.25})(Ti_{1.5}Ta_{0.5})O_7$ (RE=Gd, Sm, Y; x= 0.25, 0.5).
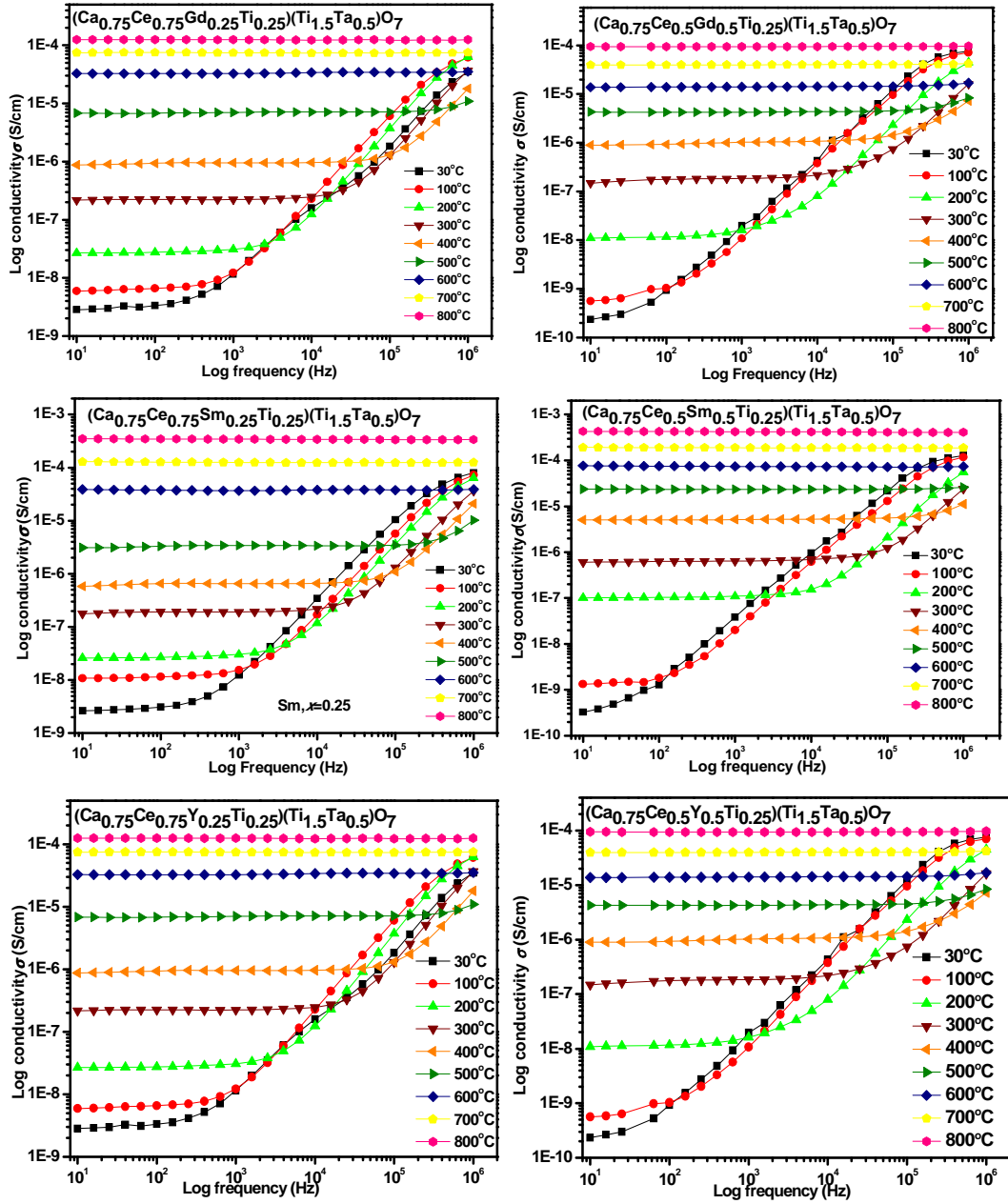
Fig. 5.7 Impedance curves of log ac conductivity as a function of log frequency at various temperatures for $(Ca_{0.75}Ce_{1-x}RE_xTi_{0.25})(Ti_{1.5}Ta_{0.5})O_7$ (RE = Gd, Sm, Y; x= 0.25, 0.5).

143

Fig. 5.6 shows the variation of imaginary part of impedance with log frequency from 30 to 800^oC. The Z'' value deceases with increase in temperature and it reaches a maximum value at a particular frequency for every temperature indicating a relaxation mechanism in the compound. This peak value shifts from low frequency region to high frequency region with increase of temperature. Peak broadening is also seen in this material confirming the presence of space charges with increase of temperature. And due to the accumulation of space charges, Z'' magnitude merges to a single value at high frequency region.

The effect of temperature and frequency on the ac conductivity of the sample is given in Fig. 5.7. It can be observed that the frequency dependence of conductivity shows two distinct regions, within the measured frequency range 10 Hz-1MHz, they are (a) the low frequency plateau region and (b) high frequency dispersion region. The low frequency plateau region corresponds to the frequency independent conductivity, σ_{dc}. The plateau region of conductivity increases with increase in temperature and the value of plateau region conductivity also increase with temperature. At high temperatures and low frequencies, this contribution is nearly frequency independent and thus can be assumed to reflect the dc conductivity. This type of conductivity is attributed to the long range transport of mobile electrons in response to the

temperature and field. At very high frequencies, the conductivity is found to be linearly dependent on frequency due to hopping transport of localized charge carriers [Elliott S.R 1987]. The ac conductivity of most of the materials is explained by the Jonscher's power law equation [Jonscher A.K 1977]. The detailed discussion is given in chapter 3(Section 3.3.4).

It is interesting to see that the ac conductivity is strongly dependent on Ce content of $(Ca_{0.75}Ce_{1-x}RE_xTi_{0.25})(Ti_{1.5}Ta_{0.5})O_7$ (where x=0, 0.25, 0.5, 0.75). The value of ac conductivity at each temperature decreases drastically with decrease in Ce content in $(Ca_{0.75}Ce_{1-x}RE_xTi_{0.25})(Ti_{1.5}Ta_{0.5})O_7$.

5.3.4 Electrical conductivity and NTC thermistor parameters

The authors have already reported pyrochlore structured semiconducting compounds in Ca-Ce-Ti-Ta/Nb-O system [Deepa M *et al* 2009]. The semiconductivity may be due to the variable valency of cerium. Here the structure will be stable only if Cerium remains in the Ce^{3+} state in order to satisfy the oxygen stoichiometry of the compound instead of its stable valency as Ce^{4+}. The excess oxygen coming from CeO_2 will be released to the atmosphere leaving behind an electron in the lattice and this electron will be responsible for the semiconductivity of the compound.

The electrical conductivity data of the above compounds reveals that they are semiconducting in nature. Fig. 5.8 shows the electrical conductivity

(log σ) as a function of absolute temperature (1000/T) temperature. The nature of variation obeys the Arrehnius equation $\sigma = \sigma_0 \exp(-Ea/K_BT)$ where Ea is the activation energy, K_B Boltzmann constant, T is the absolute temperature and σ_0 is the pre-exponential factor. A decrease in conductivity is observed as cerium is substituted by other rare earths. This decrease in conductivity may be due to the reduction in the number of conduction electrons contributed by cerium.
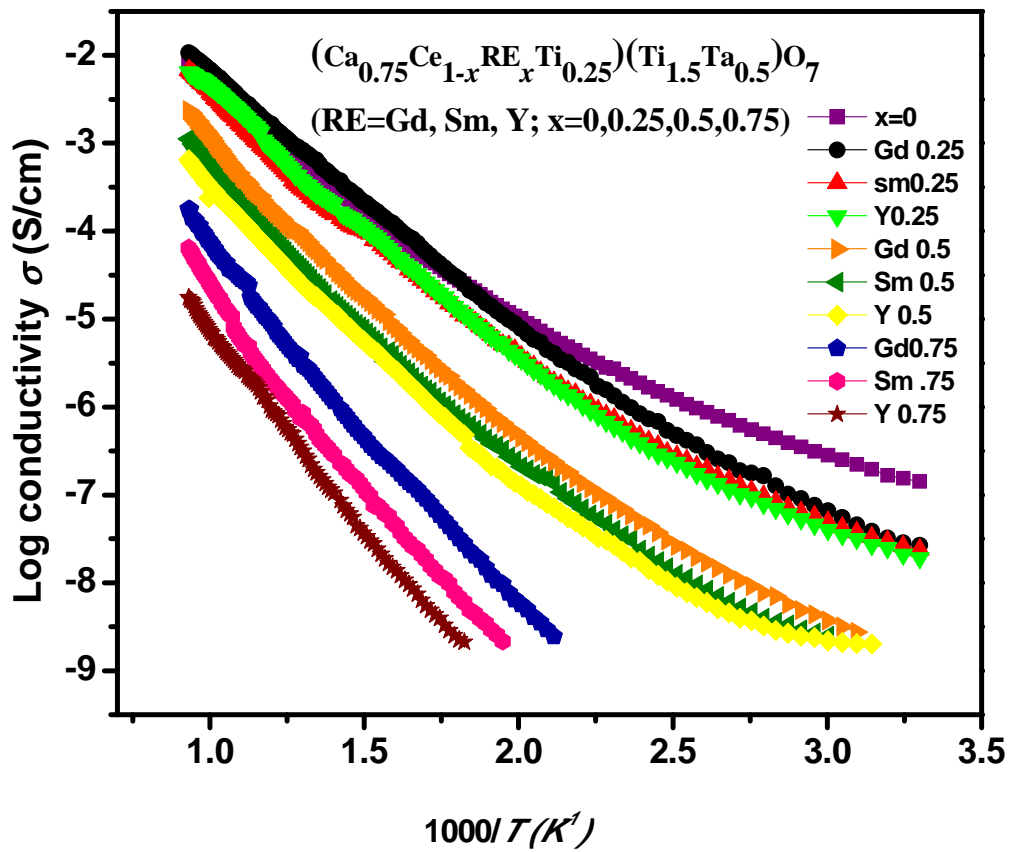
Fig.5.8 Variation of log conductivity (σ) vs. reciprocal of temperature for $(Ca_{0.75}Ce_{1-x}RE_xTi_{0.25})(Ti_{1.5}Ta_{0.5})O_7$ (RE=Gd, Sm, Y; x=0, 0.25, 0.5, 0.75)

The relation between resistance and temperature for a negative temperature coefficient thermistor is expressed by the following equation [Nobre M. A. L and Lanfredi S 2002]

$$R_T = R_N \exp\left[\beta\left(\frac{T_N - T}{TT_N}\right)\right] \qquad (5.3)$$

where R_T is the resistance at temperature T, R_N is the resistance at temperature T_N known, and β is a thermistor characteristic parameter. Rewriting and rearranging the terms of equation (5.3), β can be derived as follows:

$$\beta = \left[\frac{TT_N}{T_N - T}\right]\ln\left(\frac{R_T}{R_N}\right) \qquad (5.4)$$

The thermistor sensitivity is defined by the temperature coefficient of resistance α, which can be expressed as a function of the β parameter, in according to following equation:

$$\alpha = \left(1/R\right)[d(R)/dT] = -\beta/T^2 \qquad (5.5)$$

Considering Arrhenius plot Fig. 5.8 α and β parameters were calculated by the above equations. The values are calculated in two temperature ranges ie from 300°C to 600°C and 400°C to 800°C and the data are given in Table 5.1 and Table 5.2 respectively. The activation energies of conduction are calculated from the slopes of the plots in the temperature range of 400°C to

147

Composition	Thermistor constant β (K)	Sensitivity $\alpha(K^{-1})$	
		300°C (K^{-1})	600°C (K^{-1})
x=0	6376	-0.0194	-0.00837
Gd 0.25	6663	-0.0203	-0.00874
Sm 0.25	6776	-0.0206	-0.00889
Y0.25	7307	-0.0222	-0.00958
Gd 0.5	7432	-0.0226	-0.00980
Sm 0.5	7738	-0.0236	-0.01020
Y0.5	7836	-0.0239	-0.01028
Gd 0.75	9266	-0.0282	-0.01220
Sm 0.75	9493	-0.0289	-0.01250
Y0.75	10300	-0.0314	-0.01351

Table 5.1 β Constant and sensitivity α for $(Ca_{0.75}Ce_{1-x}RE_xTi_{0.25})(Ti_{1.5}Ta_{0.5})O_7$ (RE = Gd, Sm, Y; x=0, 0.25, 0.5, 0.75) in the temperature range of 300°C to 600°C.

Composition	Thermistor constant β(K)	Sensitivity α (k^{-1})		Aging constant at 500°C (%)	Activation Energy (eV)
		at 400°C (K^{-1})	at 800°C (K^{-1})		
x=0	6905	-0.0152	-0.0059	2.05	0.59
Gd 0.25	6918	-0.0153	-0.0060	0.33	0.60
Sm 0.25	7221	-0.0159	-0.0063	1.76	0.67
Y0.25	7523	-0.0166	-0.0065	1.76	0.69
Gd 0.5	8252	-0.0196	-0.0077	2.92	0.65
Sm0.5	8411	-0.0186	-0.0073	2.65	0.72
Y 0.5	8635	-0.0191	-0.0075	1.73	0.74
Gd 0.75	10580	-0.0234	-0.0092	2.12	0.90
Sm0.75	10914	-0.0241	-0.0095	2.855	0.93
Y 0.75	11123	-0.0246	-0.0097	1.72	0.97

Table 5.2 β Constant, α and Activation energy for $(Ca_{0.75}Ce_{1-x}RE_xTi_{0.25})(Ti_{1.5}Ta_{0.5})O_7$ (RE = Gd, Sm, Y; x=0, 0.25, 0.5, 0.75) in the temperature range of 400°C to 800°C.

800°C and are listed in Table 5.2. The aging tests at 500°C reveal that the variation of the aging coefficient (ΔR/R) is 1–3% for the time period of 500 h.

In accordance with expectation, the β values are found to be increasing with the decrease in cerium concentration starting from $x = 0$ to $x = 0.75$ this indicates that the conductivity of these compounds mainly depends on the concentration of cerium in the composition. In addition to the reduction in conduction electrons arising from cerium with increase in the rare earth substitution, the increase of resistivity of the thermistors could be due to an increase in the grain boundary area as observed in the microstructure. This can be explained as follows: The grain boundaries act as a scattering center of charge carriers. As a consequence, the relative frequency of electron scattering increases, and their mobility decreases, resulting in an increase in the resistivity [Park K 2005]. The variation of β value with the concentration of different rare earths has been given in Fig.5.9. On further investigation one can see that Y substitution yields a high value of β constant followed by Sm and then Gd. This may be due to the contribution of electrons by the rare earth for conduction. Gd has more number of valence $\bar{e}$ s than Sm and then Y. The $\beta_{400/800°C}$ value of the different compositions lies in the range of 6000-12000K. The results indicate that the thermistor characteristics can be tuned to the desired value by changing the cerium concentration in the compound. It is

observed that these values are in the desirable range of high temperature thermistors [Feteira A 2009].

The dependence of $\beta_{300/600°C}$ constant of the samples on different rare earth concentration is shown in Fig. 5.9. Drastic variation in β constant is observed with change in Ce concentration. Hence we can conclude that by varying the Ce content in the composition the β constant can easily be tuned. Further fine tuning of β constant will be possible with small amount of rare earth addition (Gd, Sm or Y).
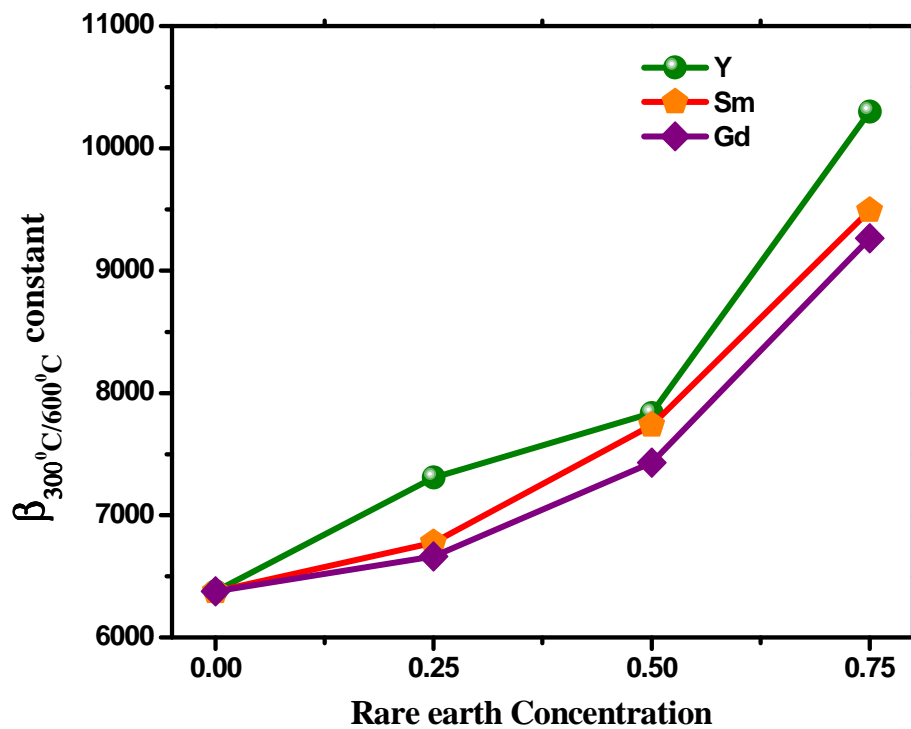
Fig. 5.9 Variation of $\beta_{300/600°C}$ constant with different rare earth concentration

5.3.5. Conclusions

An enhancement of thermistor parameters of $Ca_{0.75}CeTi_{0.25})(Ti_{1.5}Ta_{0.5})O_7$ ceramic is observed with rare earth doping. The thermistor constant obtained are in the desirable range of a high temperature thermistor. It has been observed that the cerium concentration play a major role in controlling these properties. Hence it has been concluded that the electrical properties can be tuned with varying the cerium concentration in the compounds. Further the fine tuning of NTC thermistor parameters can be tuned with small amount of other rare earth doping.

CHAPTER 6

SYNTHESIS AND CHARACTERISATION OF NEW POWELLITE TYPE SEMICONDUCTING OXIDES IN
Ca – Ce – Nb – M – O (M =Mo or W) SYSTEM

6.1 Introduction

Complex oxides have supplied numerous materials of interest to solid-state chemists, condensed matter physicists, and materials scientists. They exhibit interesting transport properties such as superconductivity [Meng Q B *et al* 1998], metallic conductivity [Tejada-Rosales E M *et al* 2002], semiconductivity [Deepa M *et al* 2009], magnetism etc. Semiconducting oxides are a very important group of materials, their applications span through photocatalysts [Zhou L 2006], NTC thermistors [Park K 2005], gas sensors [Ding H *et al* 2005] etc. Semiconducting oxides have been reported with different crystal structures such as perovskite, pyrochlore, spinel etc. Semiconducting ceramics are commonly polycrystalline spinels (MMn_2O_4 where M = Ni, Fe, Co, Cu, Zn) with a combination of cations of transition metals, are the known materials for negative temperature coefficient of resistance (NTC) thermistors [Sarrion M.L.M and Morales M 1995]. NTC thermistors are widely used in automotive, house appliances, aerospace as elements for suppression of in-rush current, for temperature measurements, control etc [Feteira A 2009]. However, the application of these materials is limited to temperatures below 300 °C due to their instability and changing electrical characteristic [de Gyorgyfalva G and Reaney I.M 2001]. Therefore,

there is a need for the development of new materials which have good electrical characteristics at high temperatures.

Tungstates and molybdates having powellite or scheelite structure are found to be very interesting due to their structural, electronic, and catalytic properties. Because of their exceptional properties, they are found to have potential applications in various fields, such as photoluminescence, hosts for lanthanide activated lasers etc. This versatile structure allows a variety of A and B cations with 1+, 2+, 3+, 4+ valency and 5+, 6+ valency respectively to be accommodated [Hazen R.M *et al* 1985]. The only condition is that the A and B cations should be capable of eight fold and tetrahedral coordination respectively. Many of the electrical properties of the tungstates and molybdates have been reported as semiconductor to metal transition [Shi F.N *et al* 1995] low TCK dielectrics etc [Nair K R *et al* 2008].

The present study deals with the synthesis and characterization of novel powellite structured semiconducting ceramic oxides in Ca-Ce-Nb-M-O system (M=Mo or W). Earlier studies on $CaLnNbMoO_8$ (where Ln = La, Sm …) show good dielectric properties [Nair K.R *et al* 2008], but when other rare earths is replaced by cerium, the compound becomes grayish black and semiconducting. The semiconducting nature of the compound is probably due to conversion of Ce^{4+} to Ce^{3+} in the lattice to reduce the number of oxygen atoms to maintain

154

the oxygen stoichiometry (4:8) in the powellite type structure. In this study, a new series of powellite type semiconducting ceramic oxides in a Ca – Ce – Nb– M – O (M = Mo or W) system were prepared in different stoichiometric compositions to investigate the effect of Ce content on the structure, microstructure and semiconductivity.

6.2 Experimental

The polycrystalline samples of Ca-Ce-Nb-M-O (where M = Mo or W) were synthesized through conventional solid state route. Stoichiometric amounts of $CaCO_3$, CeO_2, Nb_2O_5, MoO_3 and WO_3 were taken as the starting reagents (Acros 99.9% purity). In sequence these oxides were rigorously mixed using an agate mortar with acetone as the mixing medium so as to form a homogeneous mixture. Crystalline powders were prepared by calcinations of precursor powders in a furnace at $1100^{o}C/3h$ with a heating rate of $5°C/min$. The calcination was repeated twice with intermittent grinding. The calcined powder was then made into pellets with 10 mm diameter and 2 mm thickness by isostatic pressing at a pressure of 250 MPa. 4 wt% of polyvinyl alcohol (PVA; hydrolysis level 85-88%) solution was added to reduce the brittleness of the pellets. The green density of the compacted pellets is observed to be in the range of 40-45%. The pellets were preheated at 600 °C to remove PVA and were sintered at $1200^{o}C$ for 9 h.

The crystal structure of the samples was identified by powder X-ray diffraction analysis with Ni filtered CuKα radiation using a Phillips X'pert diffractometer. The microstructure of the samples was recorded by a scanning electron microscope of JEOL JSM 5600 on the thermally etched pellets. The XPS analysis was performed on the pellets in an ultrahigh vacuum using a PHI Versa probe scanning XPS microprobe with monochromatic X-ray source of Al Kα (hv=1486.6 eV). Impedance measurements of the pellets were carried out from 30 to 600° C in the frequency range 10 Hz to 1 MHz using a computer controlled impedance analyzer (Solartron, SI 1260).In order to measure the electrical conductivity the pellets were coated with a high temperature silver paste and cured at 600 ^{o}C for 30 minutes and silver wires were attached to the electroded surfaces. The conductivity was measured in a temperature range of 45 to 600 ^{o}C using a high resolution digital multimeter (Philips, PM 2525 multimeter). The readings were recorded with a slow heating after equilibrating the pellet for 2 min at each measuring temperature. The aging coefficient was measured by the relative ΔR/R of the thermistor held at 500°C in air for different periods of time up to 200h.

6.3 Results and discussion

6.3.1 Powder X-ray diffraction studies

Fig.6.1 shows the powder X-ray diffraction patterns of the sintered compounds for the compositions: $Ca_2CeNbM_2O_{12}$, $CaCeNbMO_8$ (where M = Mo or W) and $CaCe_2Nb_2MoO_{12}$. The patterns are similar to the earlier reported Ca-RE-Nb-M-O (where RE = La,Y,Gd.. and M=Mo or W) belonging to the space group $I4_1/a$ (No.88) [Nair K.R *et al* 2008].
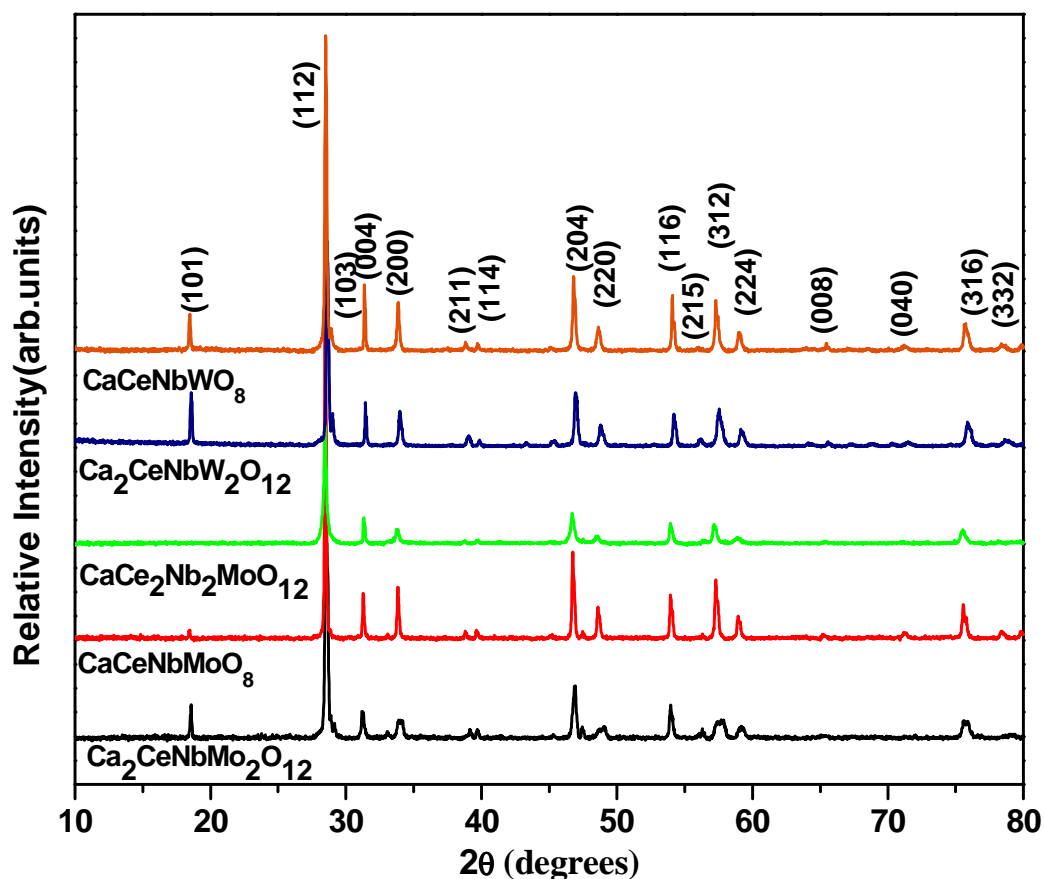
Fig. 6.1 Powder X-ray diffraction patterns for various stoichiometries in Ca-Ce-Nb-M-O system (where M=Mo or W).

All the reflections were assigned to the powellite structure in accordance with the American Mineralogist Crystal Structure data base [http://rruff.geo.arizona.edu/AMS/xtal_data/DIF fiels/12045.txt]. These compounds can be considered as solid solutions in the system x (CaMO$_4$)– $(1-x)$(CeNbO$_4$) ($0<x<1$) where CaMO$_4$ has a powellite type structure [Achary S.N *et al* 2006] and CeNbO$_4$ has a fergusonite related structure [Brixner L.H and Blasse G 1990]. The prominent peaks correspond to (112), (004), (200), (204), (220), (116) and (312) lattice planes [Nair K.R *et al* 2008]. The sharp and intense peaks of the patterns indicate the crystalline nature of the samples. It is also observed that the intensity of the peaks is different in molybdate and tungstates. It is to be mentioned here that the intensity of (101) reflection is very strong in the scheelite type of CaWO$_4$ pattern whereas in the case of powellite type CaMoO$_4$ pattern it is relatively weak. Based on these observations, we indexed the present compounds to the powellite type structure. The lattice parameters *a* and *c* are given in Table 6.1.

6.3.2 Raman Spectroscopic analysis

Raman spectroscopy is a subtle tool capable to provide the short range structural differences since it is primarily sensitive to oxygen-cation vibrations. The compound crystallizes at ambient conditions in powellite structure that has the space group $I4_1$ /a (C^6_{4h}) with four formula units per body-centered unit

cell. The cations are at S_4 sites whereas the sixteen oxygen atoms are on general C_1 sites, group theoretical considerations lead us to expect 13 Raman active modes [Porto S.P.S and Scott J.F 1967].

$$\Gamma = 3A_g + 5B_g + 5E_g \qquad\qquad (6.1)$$

In the present study the Raman spectra were taken both for tungstates and molybdates. On the basis of the available literature different modes of the Raman spectra (Fig. 6.2) were indexed. Three external modes T (B_g), T (E_g), R (A_g) are found both for molybdates and tungstates at 90-110, 141, 204-214 cm$^-$^{1} and 84, 112-116, 212-215cm^{-1} respectively. The internal modes A_g, B_g, E_g, B_g and A_g has been detected at 316-322, 390-402, 794-808, 844 & 877 cm^{-1} for molybdates and A_g, B_g, B_g and A_g are found at 326-328, 401, 809-815 & 909 cm^{-1} for tungstates.
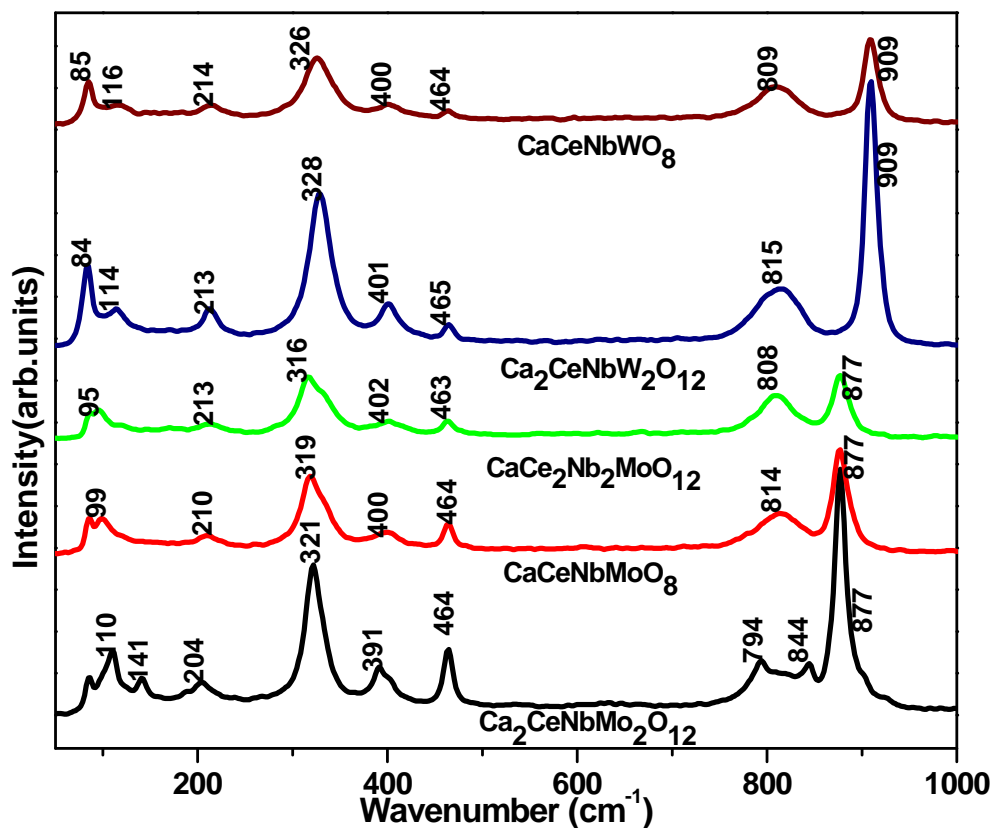
Fig. 6.2 Raman spectra for various stoichiometries in (a) Ca-Ce-Nb-M-O system (where M = Mo or W).

The spectra provide an evidence of the powellite structure for all the compounds. The mode observed around 465 cm^{-1} is usually IR active mode and only visible in Raman due to some stretching modes arises from another cation oxygen bonds [Frost R.L *et al* 2007]. The Raman spectra analysis unequivocally says that all these compounds belong to the powellite structure.

6.3.3 Scanning electron microscopy and microstructure

Fig. 6.3 shows the SEM micrographs of the polished thermally etched samples. Both the oxides show well sintered and well grown grains in 1-5µm size range with almost same morphological appearance.
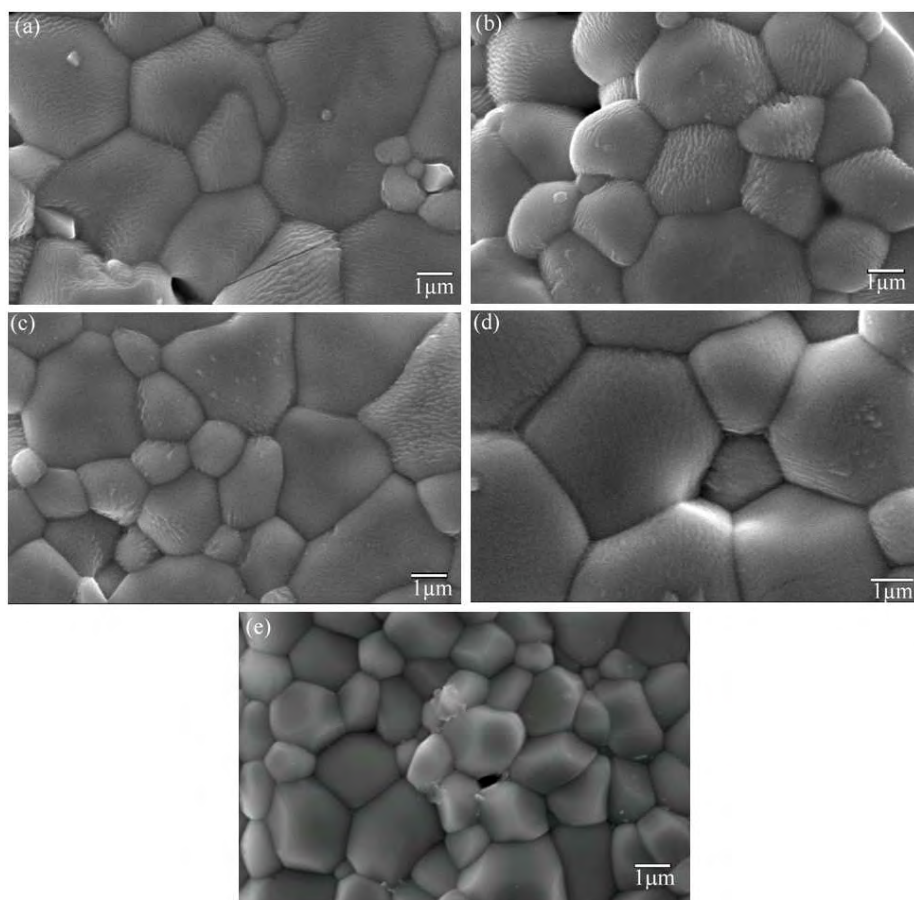
Fig. 6.3 Typical micrographs of (a) $Ca_2CeNbMo_2O_{12}$ (b) $CaCeNbMoO_8$
(c) $CaCe_2Nb_2MoO_{12}$ (d) $Ca_2CeNbW_2O_{12}$ and (e) $CaCeNbWO_8$.

6.3.4 X-ray photoelectron spectroscopy

Fig. 6.4 shows the Ce 3d XP spectra and the curve fitting example of Ce 3d XPS peaks recorded for $CaCeNbWO_8$. The XPS Ce $3d_{5/2}$ and $3d_{3/2}$ doublets

are commonly denoted by u and v and extend in the energy range of 880-920 eV [Mullins D.R *et al*1998]. The peaks labeled u are due to $3d_{3/2}$ spin orbit states and those labeled v are the corresponding $3d_{5/2}$ spin-orbit states. The *u'*/*v'* doublet is due to the photoemission from the Ce (III) cations.
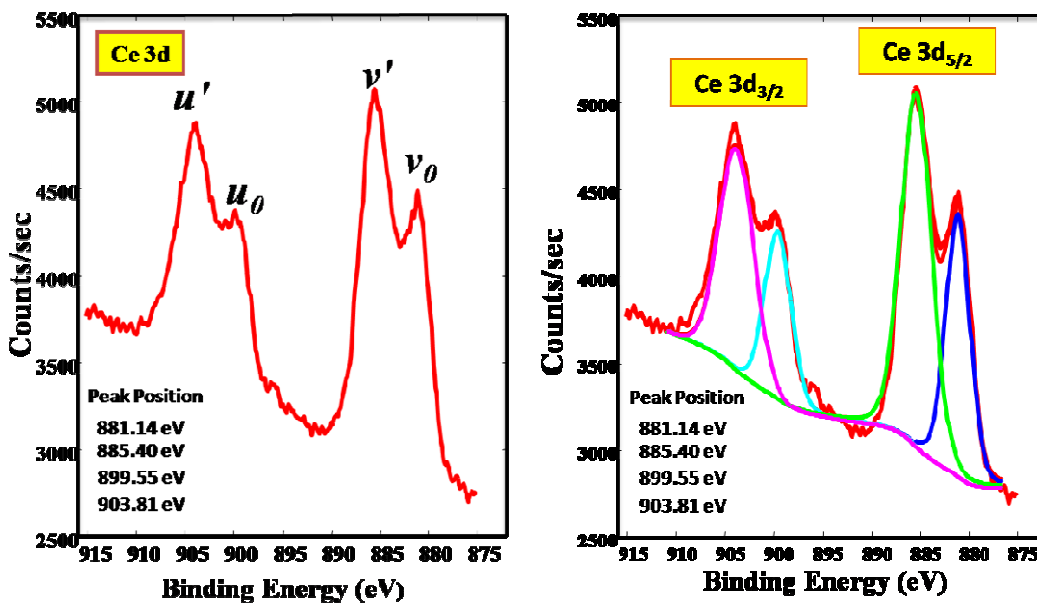
Fig. 6.4. Ce 3d XP spectra and the curve fitting example of Ce 3d XPS peaks for $CaCeNbWO_8$.

The Ce 3d spectrum of $CaCeNbWO_8$ contains only the completely reduced Ce $^{3+}$ cation. The another doublet observed in the spectrum is labeled as u_o and v_o [Francisco M.S.P *et al* 2001].These peaks are a shakedown feature resulting from the transfer of one electron from a filled O 2p orbital to a Ce 4f orbital during photoemission from Ce^{3+} cations. The presence of u_o/v_o and *u′*/*v'* doublet peaks in the spectra indicates the presence of reduced cerium i.e. Ce^{3+} in $CaCeNbWO_8$.

6.3.5 Impedance spectroscopic analysis

Impedance spectroscopy is used to study the electrical properties of all the compounds. Polycrystalline materials have variety of frequency-dependent effects associated with heterogeneities. The frequency dependent properties of materials can be described via the complex permittivity (ε^*), complex impedance (Z^*) and dielectric loss or dissipation factor (tan δ) [Ashok Kumar *et al* 2006].

The frequency dependence of real component of impedance, Z' is plotted for different temperatures for various compositions in Ca-Ce-Nb-M-O (where M=Mo or W) in Fig. 6.5. Typical curves are observed in figures. The temperature affects strongly the magnitude of resistance. At lower temperatures, Z' decreases monotonically with increasing frequency up to a certain frequency and then becomes frequency independent. At higher temperatures, Z' is almost constant. The higher values of Z' at lower frequencies and low temperatures means the polarization is larger.
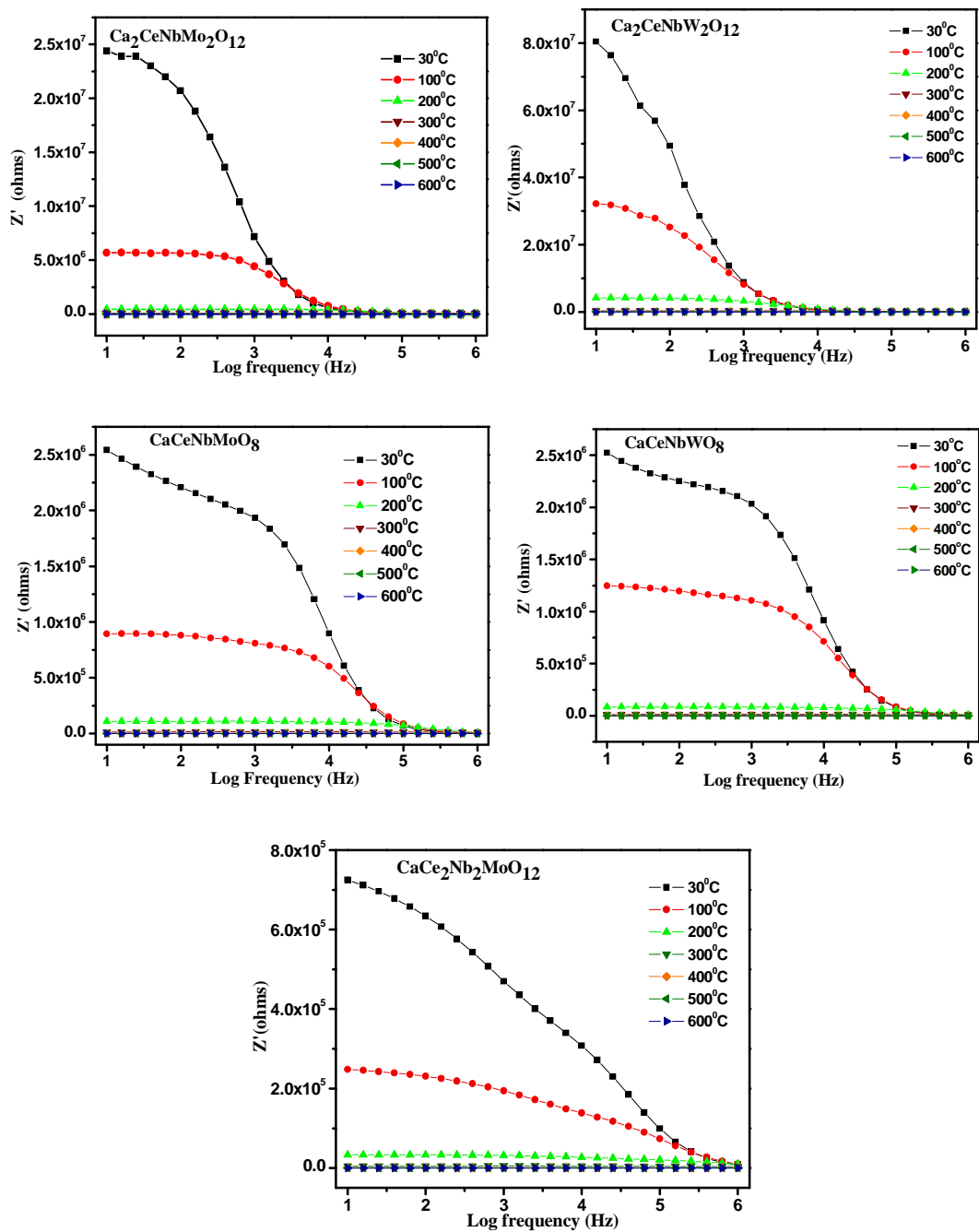
Fig. 6.5 Impedance curves of real (Z') component as a function of log frequency at various temperatures for various compositions in Ca-Ce-Nb-M-O system (where M = Mo or W).

164
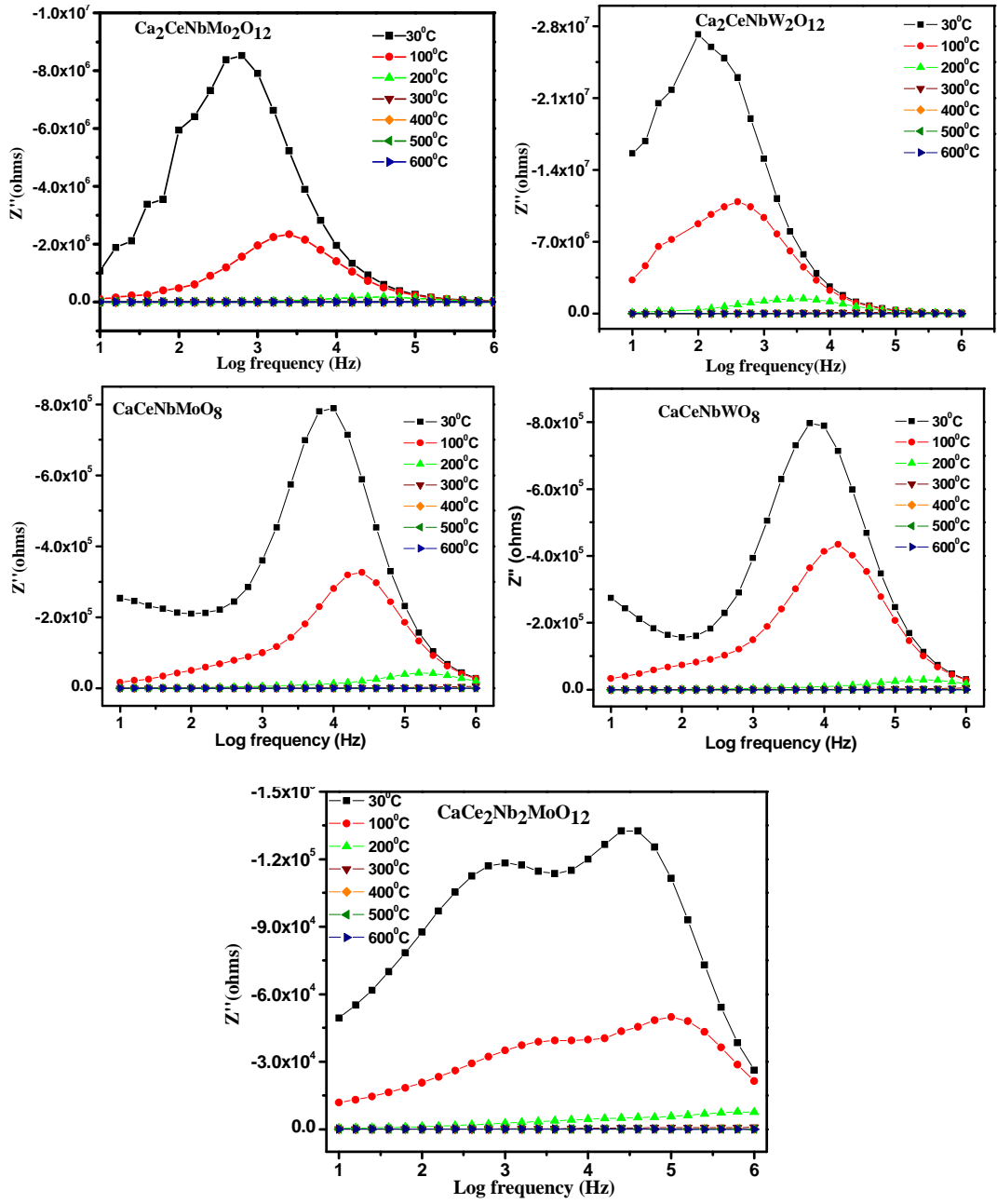
Fig. 6.6 Impedance curves of imaginary (Z″) component as a function of log frequency at various temperatures for various compositions in Ca-Ce-Nb-M-O (where M = Mo or W) system.

165

The frequency dependence of imaginary component of impedance Z" is plotted for different temperatures in Fig. 6.6. The variation of imaginary part of impedance with frequency at different temperatures provides information about the relaxation frequency of the resistive component. The peak shifts towards higher frequency with increasing temperature showing that the resistance of the bulk material is decreasing. Also the magnitude of Z" decreases with increasing frequency. This indicates the spreading of the relaxation times. This would imply that the relaxation is temperature dependent, and there is apparently not a single relaxation time. Thereby relaxation processes involved with their own discrete relaxation times depending on the temperature. As the temperature is increased, in addition to the expected decrease in magnitude of Z", there is a shift in the peak frequencies towards the high frequency side. Also it is evident that with increasing temperature, there is a broadening of the peaks and at higher temperatures, the curves appear almost flat. This behaviour is apparently due to the presence of space charges in the material.

The effect of temperature and frequency on the ac conductivity of the sample is given in Fig. 6.7. It can be observed that the frequency dependence of conductivity shows two distinct regions, within the measured frequency range 10 Hz-1MHz, they are (a) the low frequency plateau region and (b) high frequency dispersion region. The low frequency plateau region corresponds to

the frequency independent conductivity, σ_{dc}. The plateau region of conductivity increases with increase in temperature and the value of plateau region conductivity also increase with temperature. At high temperatures and low frequencies, this contribution is nearly frequency independent and thus can be assumed to reflect the dc conductivity. This type of conductivity is attributed to the long range transport of mobile electrons in response to the temperature and field. At very high frequencies, the conductivity is found to be linearly dependent on frequency due to hopping transport of localized charge carriers [Elliott S.R 1987]. The ac conductivity of most of the materials is explained by the Jonscher's power law equation [Jonscher A.K 1977].

$$\sigma(\omega) = \sigma_{dc} + A\omega^{n} \qquad (6.2)$$

where $\sigma(\omega)$ is the frequency dependent conductivity at frequency ω, σ_{dc} is the dc term associated to the mobile charge, A is a frequency independent and temperature-dependent parameter and n is the slope of high frequency dispersion data (n assumes a value between 0 and 1). It is very clear from Fig. 6.7 that the conductivity behavior exhibited by the compound does not fit this simple equation. As mentioned in the earlier text there is a visible change in the slopes as we go from lower frequency region to the higher frequency region. Hence in this system two slopes can be drawn one in the low plateau region and other in the dispersion region.
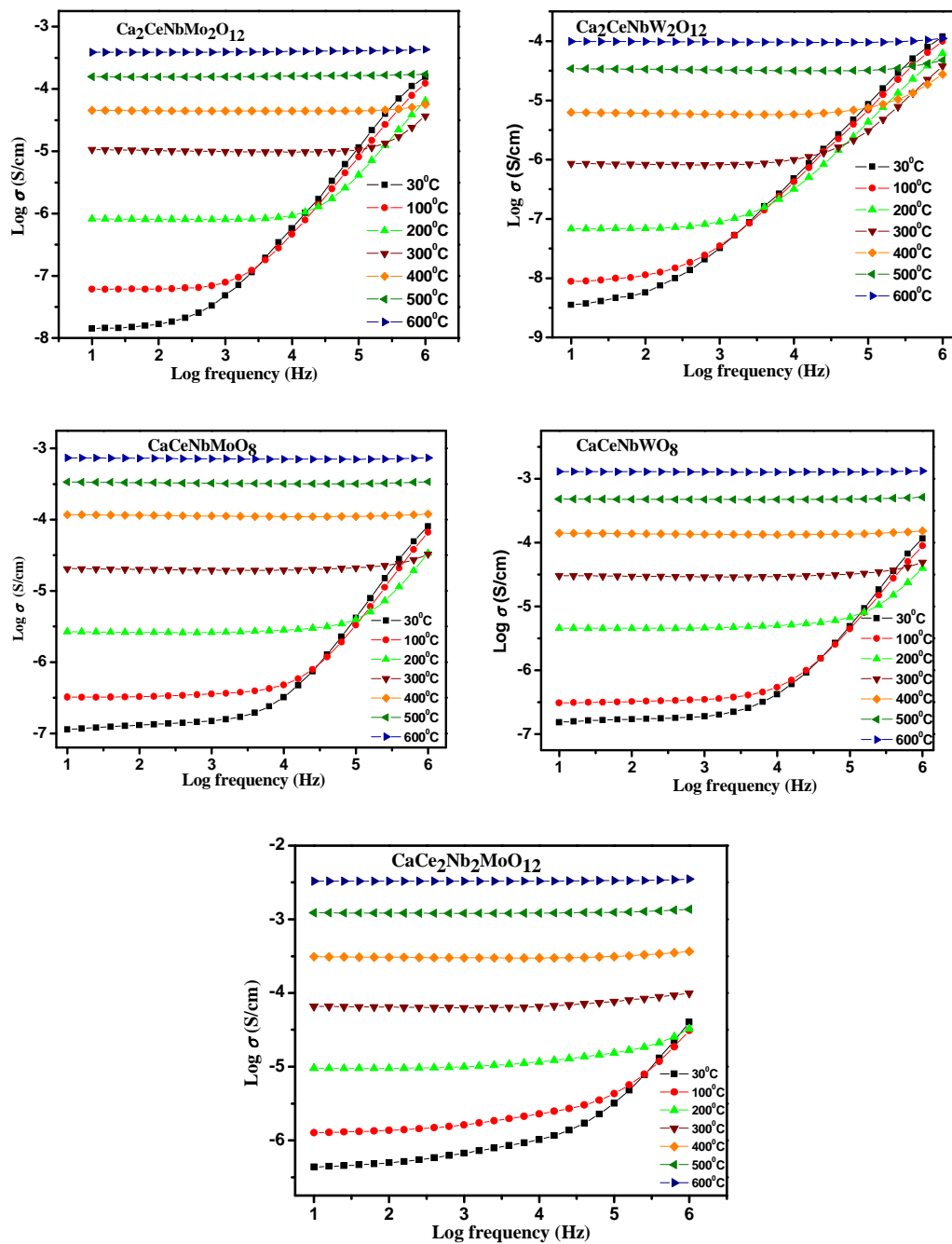
Fig. 6.7 Impedance curves of log ac conductivity as a function of log frequency at various temperatures for Ca-Ce-Nb-M-O (where M = Mo or W) system.

Therefore the frequency dependent ac conductivity can be characterized using the two term power relation

$$\sigma(\omega) = \sigma_0 + A_1\omega^{n_1} + A_2\omega^{n_2} \qquad (6.3)$$

Again A_1 and A_2 are frequency independent and temperature dependent constants. The slopes n_1 and n_2 will be, n_1 can be $0 \leq n_1 \leq 1$ and n_2 can be $0 \leq n_2 \leq 2$. The term σ_0 corresponding to the translational hopping gives the long range electrical transport (i.e dc conductivity) in the long time. The second term, $A_1\omega^{n_1}$ characterizes the low frequency region and corresponds to the translational hopping motion (short range hopping), whereas the one at high frequencies $A_2\omega^{n_2}$ corresponds to a localized or reorientational hopping or hopping of electron back and forth between two charged defects [Funke K1993]. The conduction mechanism can be explained as discussed in chapter 3 (section 3.3.4).

6.3.6 Electrical conductivity and NTC thermistor parameters

It has been already reported that powellite structured compounds in Ca-RE-Nb-Mo-O (RE=Y, La, Nd, Sm or Bi) which are colorless and insulators [Nair K.R *et al* 2008]. But when the rare-earth used is cerium the compound has become grayish-black and semiconducting. This may be due to the variable valency of cerium.

Here the structure will be stable only if cerium remains in the Ce^{3+} state in order to satisfy the oxygen stoichiometry of the compound instead of its stable valency as Ce^{4+}. The excess oxygen coming from CeO_2 will be released to the atmosphere leaving behind an electron in the lattice and this electron will be responsible for the semiconductivity of the compound. This explanation is consistent with the XPS results.
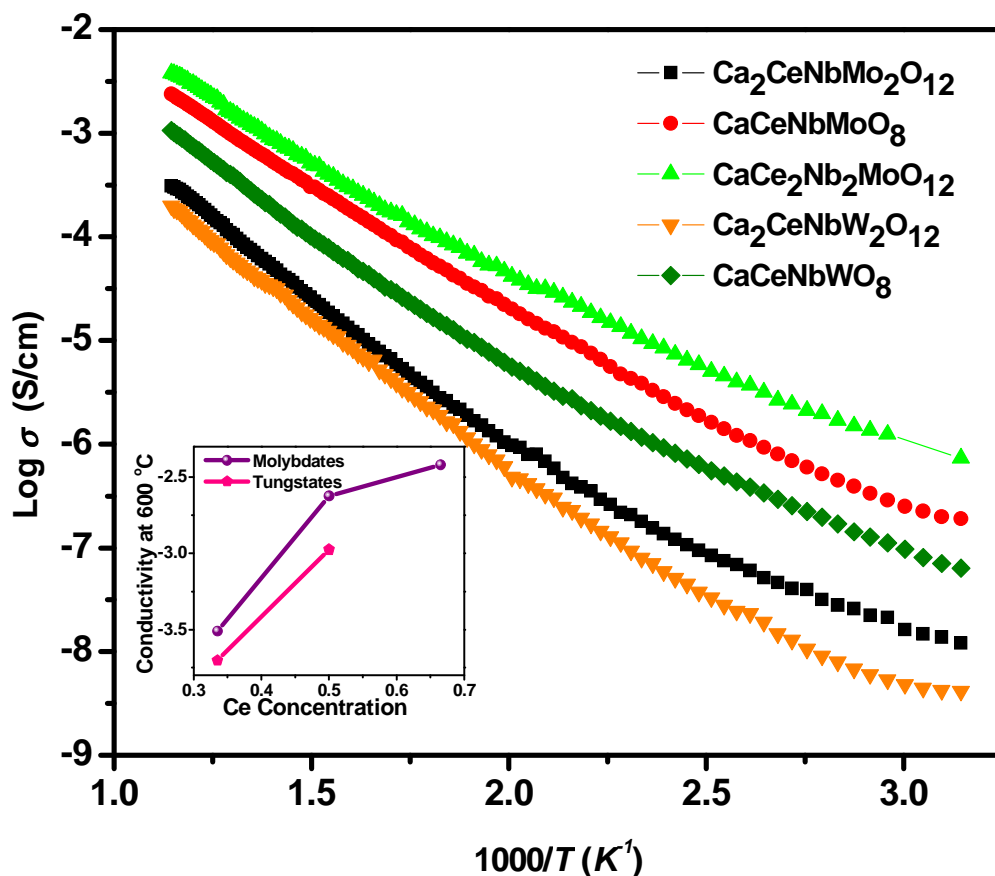
Fig. 6.8. Variation of log conductivity (σ) vs. reciprocal of temperature for Molybdates and Tungstates and the variation of conductivity with cerium concentration at 600°C in inset.

The electrical conductivity data of the above compounds reveals that they are semiconducting in nature. Fig.6.8 shows the electrical conductivity ($\log \sigma$) as a function of absolute temperature ($1000/T$) temperature. The nature of variation obeys the Arrehnius equation $\sigma = \sigma_0 \exp(-Ea/K_B T)$ where Ea is the activation energy, T is the absolute temperature and σ_0 is the pre-exponential factor. The activation energies of conduction are calculated from the slopes of the plots in the temperature range of 300°C to 600°C and are listed in Table 6.1. The conductivity is found to be increasing with the Ce content and is given in the inset of Fig.6. 8.

The relation between resistance and temperature for a negative temperature coefficient thermistor is expressed by the following equation [Nobre M.A.L and Lanfredi S 2003]

$$R_T = R_N \exp\left[\beta\left(\frac{T_N - T}{T T_N}\right)\right] \qquad (6.4)$$

where R_T is the resistance at temperature T, R_N is the resistance at temperature T_N known, and β is a thermistor characteristic parameter. Rewriting and rearranging the terms of equation (6.4), β can be derived as follows:

$$\beta = \left[\frac{T T_N}{T_N - T}\right] \ln\left(\frac{R_T}{R_N}\right) \qquad (6.5)$$

The thermistor sensitivity is defined by the temperature coefficient of resistance α, which can be expressed as a function of the β parameter, in according to following equation:

$$\alpha = \left(\frac{1}{R}\right)[d(R)/dT] = -\beta/T^2 \qquad (6.6)$$

Compounds	Lattice parameter		β(K)	α (K^{-1})		Activation energy (eV)
	a (Å)	c (Å)		300 °C	600 °C	
Ca$_2$CeNbMo$_2$O$_{12}$	5.2341	11.3691	6909	0.0211	0.0091	0.587
CaCeNbMoO$_8$	5.2831	11.3685	5659	0.0172	0.0074	0.488
CaCe$_2$Nb$_2$MoO$_{12}$	5.2673	11.3641	5518	0.0168	0.0072	0.487
Ca$_2$CeNbW$_2$O$_{12}$	5.2771	11.3851	6939	0.0210	0.0090	0.611
CaCeNbWO$_8$	5.2876	11.3870	6328	0.0193	0.0083	0.551

Table 6.1 Lattice parameter, β constant, α and Activation Energy for various compositions in a Ca–Ce–Nb–M–O (M = Mo or W) system.

Considering Arrhenius plot (Fig. 6.8), α and β parameters were calculated by the above equations. The values are calculated in the temperature range from 300 to 600°C and depicted in Table 6.1. The β value of the different compositions lies in the range of 5000-7000K. The aging tests at 500 °C reveals that the variation of aging coefficient ($\Delta R/R$) is 1-2% for the time

period of 200 h. The above results suggest that the thermistor characteristics can be tuned to the desired value by changing the cerium concentration in the compound. It is observed that these values are in the desirable range of high temperature thermistors [Feltz A 2000]. However more rigorous tests such as electrical characteristics for repeated thermal cycles and long duration are to be performed to qualify as a thermistor device.

6.4 Conclusions

In conclusion, a series of new NTC ceramic oxides in Ca – Ce – Nb – M – O (M = Mo or W) system through solid state route. The powder X-ray diffraction and Raman spectroscopy analyses showed that all these compounds belong to tetragonal powellite type structure with the space group $I4_1/a$. These compounds, having good NTC characteristics in a wide range of temperature, may find application in devices like high temperature thermistors.

CHAPTER 7

TETRAGONAL TUNGSTEN BRONZE TYPE
SEMICONDUCTING OXIDES IN Ba-Ce-Ti-Ta-O SYSTEM

7.1 Introduction

Now-a-days a large number of oxides of different structural families are available with wide variety of electrical properties such as superconductivity [Yamauchi T 2007], ferroelectricity [Yang K 2006], magnetism [Kravchenko E. A 2002], semiconductivity [Vrieland E. G 1964], ionic conductivity etc [Takamura H and Tuller H.L 2000]. Semiconducting oxides have been widely used in electronic industries because of their unique and useful electrical characteristics. Semiconducting ceramics find several applications as in thermistors [Yan X. and Xu G 2009], PTCR materials [Chatterjee S *et al* 2003], gas sensors [Lee J.H. 2009], catalysts and photoelectrolysis of water [Yazawa K *et al* 1979]. Nickel manganite-based semiconducting materials are widely used as negative temperature coefficient (NTC) thermistor materials. Classical ceramic NTC resistors composed of spinel structure (MMn_2O_4) with M = Ni, Co, Fe, Cu, Zn show aging of the electrical properties and their application is commonly limited to temperatures below 300°C. Research is going on in synthesis of ceramic materials with good thermal stability and free from aging of electrical properties [Justin M. Varghese *et al* 2008].

Solid solutions of ceramic complex oxides having tungsten–bronze (TB) type structure have been extensively studied for dielectrics since this structure endures various substitutions and thus has the potential to tailor the electrical

properties. The family of tetragonal tungsten bronze (TTB) compounds, with the general chemical formulas $(A_1)_4(A_2)_2C_4B_{10}O_{30}$ and $(A_1)_4(A_2)_2B_{10}O_{30}$ in which A_1, A_2, C, and B are the 15-, 12-, 9-, and 6-fold-coordinated oxygen octahedra sites in the crystal structure. The common chemical formula is $(A_1)_2(A_2)_4(C)_4(B_1)_2(B_2)_8O_{30}$, where positions A_1, A_2, B_1, B_2 and C will be filled by different valency cations or may be partially empty. In tungsten bronze niobates, B_1 and B_2 are filled by Nb^{5+}, A_1, A_2 and C are filled by alkali and/or alkaline earth metal ions. The BO_6 octahedra are linked by their corners to form three different types (A_l: square, A_2: pentagonal, and C: triangular) of tunnels running through the structure parallel to the c-axis. Tungsten bronzes M_xWO_3 (M = alkali atoms) have long been the subject of investigations for their interesting structural, electronic and electrochromic properties [Masetti E *et al* 1995].

The present chapter deals with the synthesis and characterization of novel tetragonal tungsten bronze (TTB) structured semiconducting ceramic oxides in Ba-Ce-Ti-Ta-O system. Earlier studies on Ba-RE-Ti-Nb/Ta-O (RE = La,……) show good dielectric properties [Peter Koshy *et al* 1998], but when Ce is replaced by other rare earths, the compound becomes black and semiconducting. The semiconducting nature of the compound is probably due to conversion of Ce^{4+} to Ce^{3+} in the lattice to reduce the number of oxygen

atoms to maintain the oxygen stoichiometry in the TTB type structure. In the present study, a new series of tetragonal tungsten bronze type semiconducting ceramic oxides in Ba – Ce – Ti – Ta – O system were prepared in different stoichiometric compositions to investigate the effect of Ce content on the structure, microstructure and semiconductivity.

7.2 Experimental

The polycrystalline samples of $BaCe_5Ti_7Ta_3O_{30}$, $Ba_2Ce_4Ti_6Ta_4O_{30}$ $Ba_3Ce_3Ti_5Ta_5O_{30}$, $Ba_4Ce_2Ti_4Ta_6O_{30}$ and $Ba_5CeTi_3Ta_7O_{30}$ were synthesized through conventional solid state route. Stoichiometric amounts of $BaCO_3$, CeO_2, TiO_2 and Ta_2O_5 were taken as the starting reagents (Acros 99.9% purity). In sequence these oxides were rigorously mixed using an agate mortar with acetone as the mixing medium so as to form a homogeneous mixture. Crystalline powders were prepared by calcinations of precursor powders in a furnace at $1300^oC/3h$ with a heating rate of 5°C/min. The calcination was repeated twice with intermittent grinding. The calcined powder was then made into pellets with 10 mm diameter and 2 mm thickness by isostatic pressing at a pressure of 250 MPa. 4 wt. % of polyvinyl alcohol (PVA; hydrolysis level 85-88%) solution was added to reduce the brittleness of the pellets. The green density of the compacted pellets is observed to be in the range of 40-45%. The

pellets were preheated at 600°C to remove PVA and were sintered at 1350 ^{o}C for 9 h.

The crystal structure of the samples was identified by powder X-ray diffraction analysis with Ni filtered CuKα radiation using a Phillips X'pert diffractometer. The microstructure of the samples was recorded by a scanning electron microscope of JEOL JSM 5600 on the thermally etched pellets. To measure the electrical properties of the compounds, a high temperature curing silver paste was applied to both sides of the pellets and cured at 600°C for 30min in a tubular furnace. These pellets were then attached with long silver lead wires on both sides. Impedance measurements of the pellets were carried out from 30 to 600° C in the frequency range 10 Hz to 1 MHz using a computer controlled impedance analyzer (Solartron, SI 1260). The dc conductivity with respect to temperature was measured using a high-resolution digital multimeter (Philips, PM 2525 multimeter). The conductivity was measured in a temperature range of 30–600°C. The readings were recorded with a slow heating after equilibrating the pellet for 2 min at each measuring temperature.

7.3 Results and discussion

7.3.1 Powder X-ray diffraction analysis
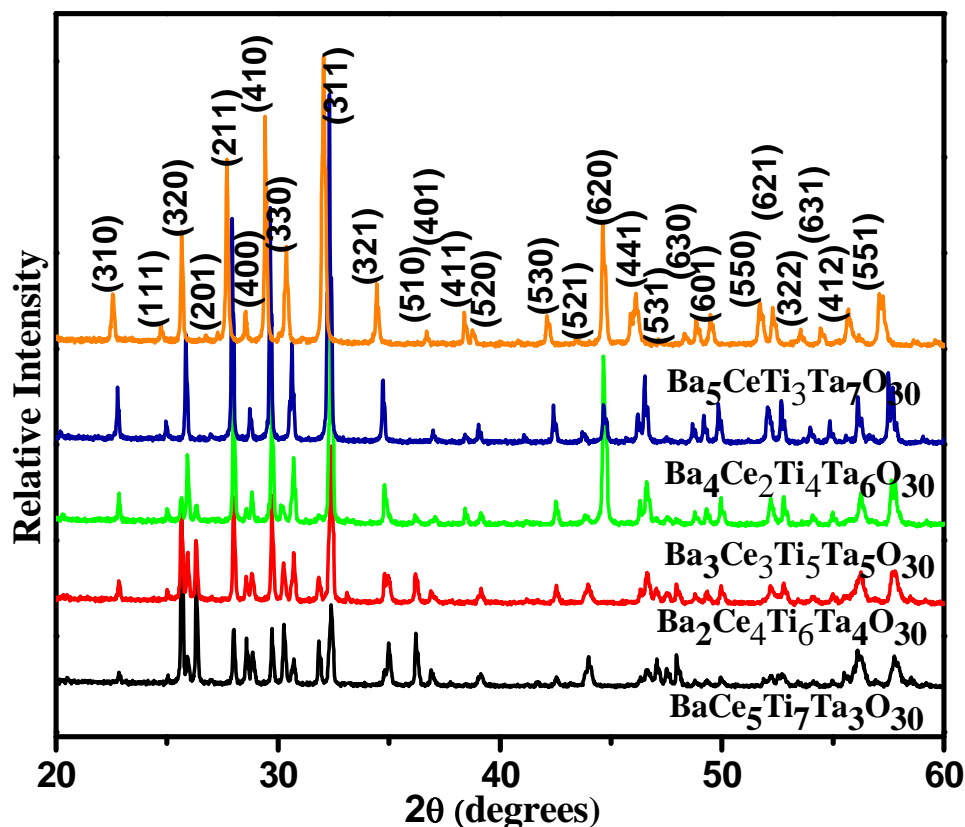
Fig.7.1 Powder X-ray diffraction patterns of various compositions in Ba-Ce-Ti-Ta-O system

Powder XRD patterns of the samples are shown in Fig. 7.1. The tungsten bronze phase mentioned here is similar to that of $Ba_3La_3Ti_5Nd_5O_{30}$ (JCPDS No. 39-1331). The indexed X- ray diffraction patterns show that the compounds are single phase. The sharp peaks in the XRD pattern suggest the high crystalline nature of the compounds. There is a significant difference in

the intensities observed with different compositions. The unit cell parameters of the compounds were calculated and tabulated in Table 7.1.

7.3.2 Raman spectroscopic studies
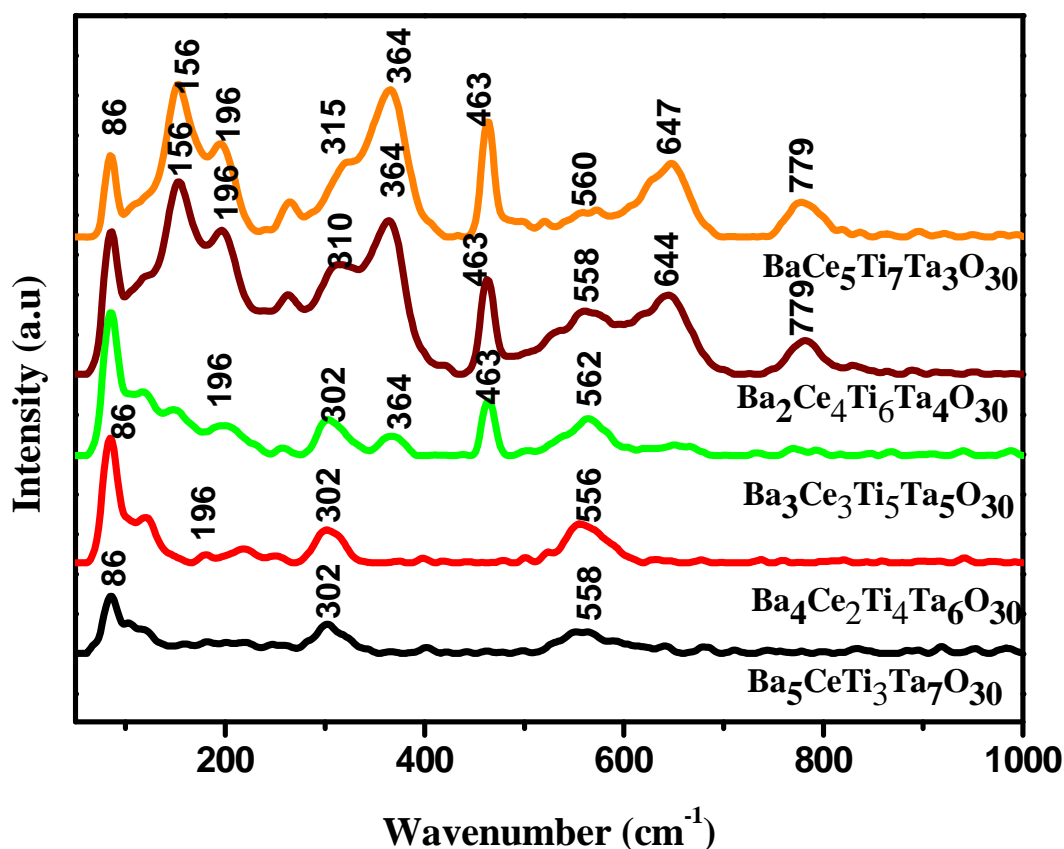
Fig. 7.2 Raman spectra for various stoichiometries in Ba-Ce-Ti-Ta-O system.

Raman spectroscopy has been successfully used as a tool for studying the structure of tetragonal tungsten bronze compounds. It is a very sensitive technique for structural modifications and constitutes a powerful tool for the detection of symmetry changes. The point groups associated to these room temperature structure is C_{4v} (*P4bm*) for the tetragonal phase.

These modes can be classified according to the following irreducible representations of the C_{4v} point group at the center of the Brillouin zone:

$$\Gamma = 19A_1 + 15A_2 + 14B_1 + 18B_2 + 36E \qquad (7.1)$$

Three of these modes belonging to A_1 and E (two fold degenerate) representations are acoustic modes and all the other modes, except A_2 modes, are Raman active. Therefore, there are 120 Raman active modes that are significantly superior to the number of Raman lines observed in the experiments. It is possible that several nearly degenerate phonon modes may appear as a single broad band with asymmetric line-shape [Burns G. *et al* 1969]. Another reason that the Raman lines of TTB ferroelectric compounds are fairly broad comes from the structural disorder which causes breakdown of the Brillouin zone-center wave vector selection rules, making the assignment of Raman peaks to specific irreducible representation of the point group difficult.

Fig.7.2 shows the room-temperature Raman spectra of the 5 compositions of Ba-Ce-Ti-Ta-O ceramics. With the changes in elemental constitution, say with decrease in cerium the Raman spectra exhibit broadening of all Raman modes. This is a signature of the lattice disordering. The different behavior of O-Ta-O bending and Ta-O stretching vibrations can be attributed to the large number of modes involved in the spectral range between 150 and

320 cm^{-1} as reported in the literature on TTB ferroelectric materials [Xia H.R. *et al*1997] while in the range 550 to 750 cm^{-1}, only two peaks were reported [Amzallag E. *et al*1971; Wilde R.E 1991].The B_1 and B_2 modes are observed near 664 and 780cm^{-1}.

7.3.3 Scanning electron microscopy and microstructure

The SEM micrographs recorded from thermally etched surface (1325°C/30 min) of the sintered pellets are shown in Fig. 7.3. The microstructure of all the sintered compounds reveals well-grown grains. It is observed that as the cerium concentration is decreasing in the sample the amount of porosity has been increased. In addition to it the shape of the grains changes from flat rod type nature to more elongated shape. The grain size evaluated from the micrograph was found to be in the range of 3–5 μm.
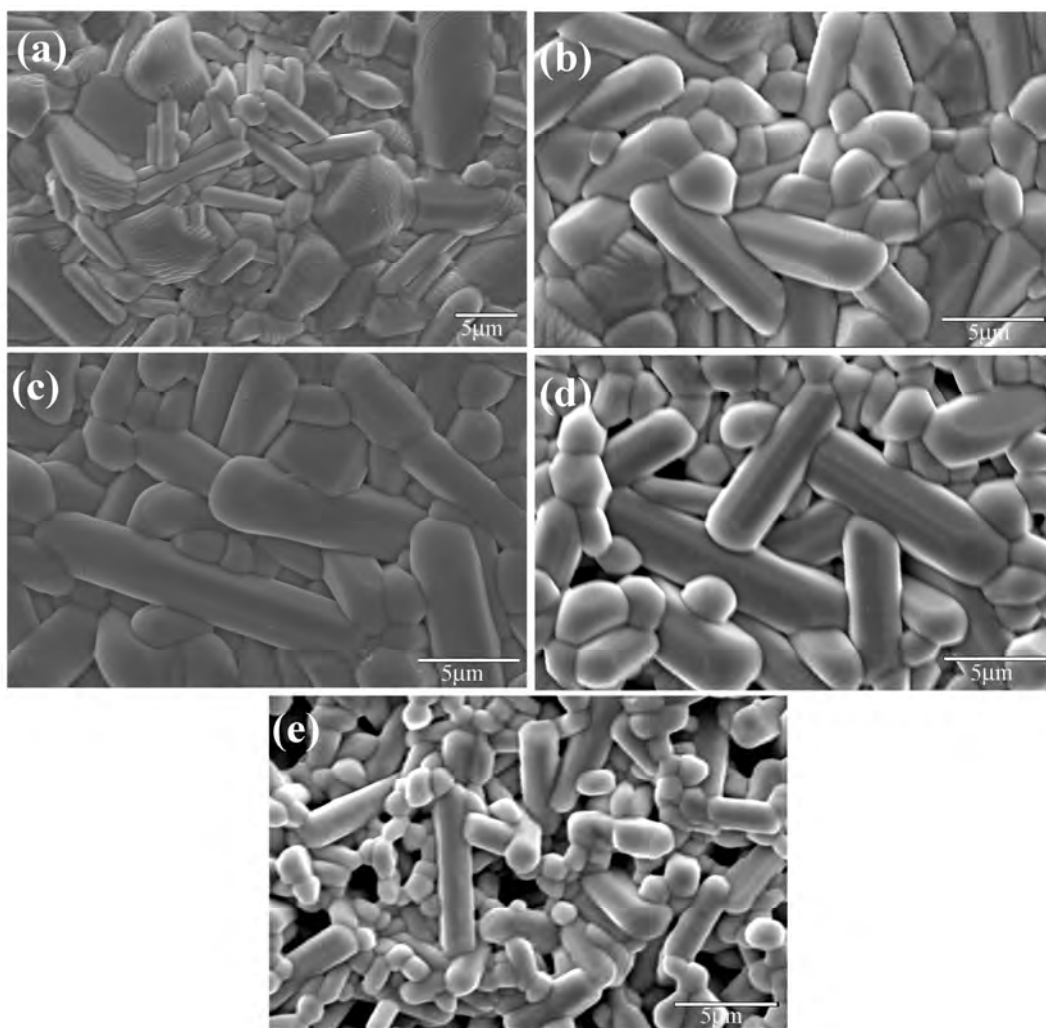
Fig.7.3 Typical micrographs of (a) $BaCe_5Ti_7Ta_3O_{30}$, (b) $Ba_2Ce_4Ti_6Ta_4O_{30}$ (c) $Ba_3Ce_3Ti_5Ta_5O_{30}$ (d) $Ba_4Ce_2Ti_4Ta_6O_{30}$ (e) $Ba_5CeTi_3Ta_7O_{30}$.

7.3.4 Impedance spectroscopic studies

Impedance spectroscopy has been employed to evaluate the electronic and ionic components of the total charge transport. This method involves the employment of low amplitude ac frequency signal over the sample and separation of real and imaginary parts of impedance. The impedance

measurements were carried out for all the samples in the frequency range of 10 Hz to 1 MHz and in the temperature range of 30 to 600°C.

Fig. 7.4 shows the variation of the real part of impedance (Z') with frequency at different temperatures. It is observed that the magnitude of Z' decreases with the increase in both frequency as well as temperature. The Z' values for all temperatures merge at higher temperature. This may be due to the release of space charges. The curves also display single-relaxation process and indicate increase in ac conductivity with the increase in temperature and frequency.

Fig. 7.5 shows the variation of imaginary part of impedance (Z'') with log frequency from 30 to 600°C. The Z'' value deceases with increase in temperature and it reaches a maximum value at a particular frequency for every temperature indicating a relaxation mechanism in the compound. This peak value shifts from low frequency region to high frequency region with increase of temperature. Peak broadening is also seen in this material confirming the presence of space charges with increase of temperature. And due to the accumulation of space charges, Z'' magnitude merges to a single value at high frequency region.
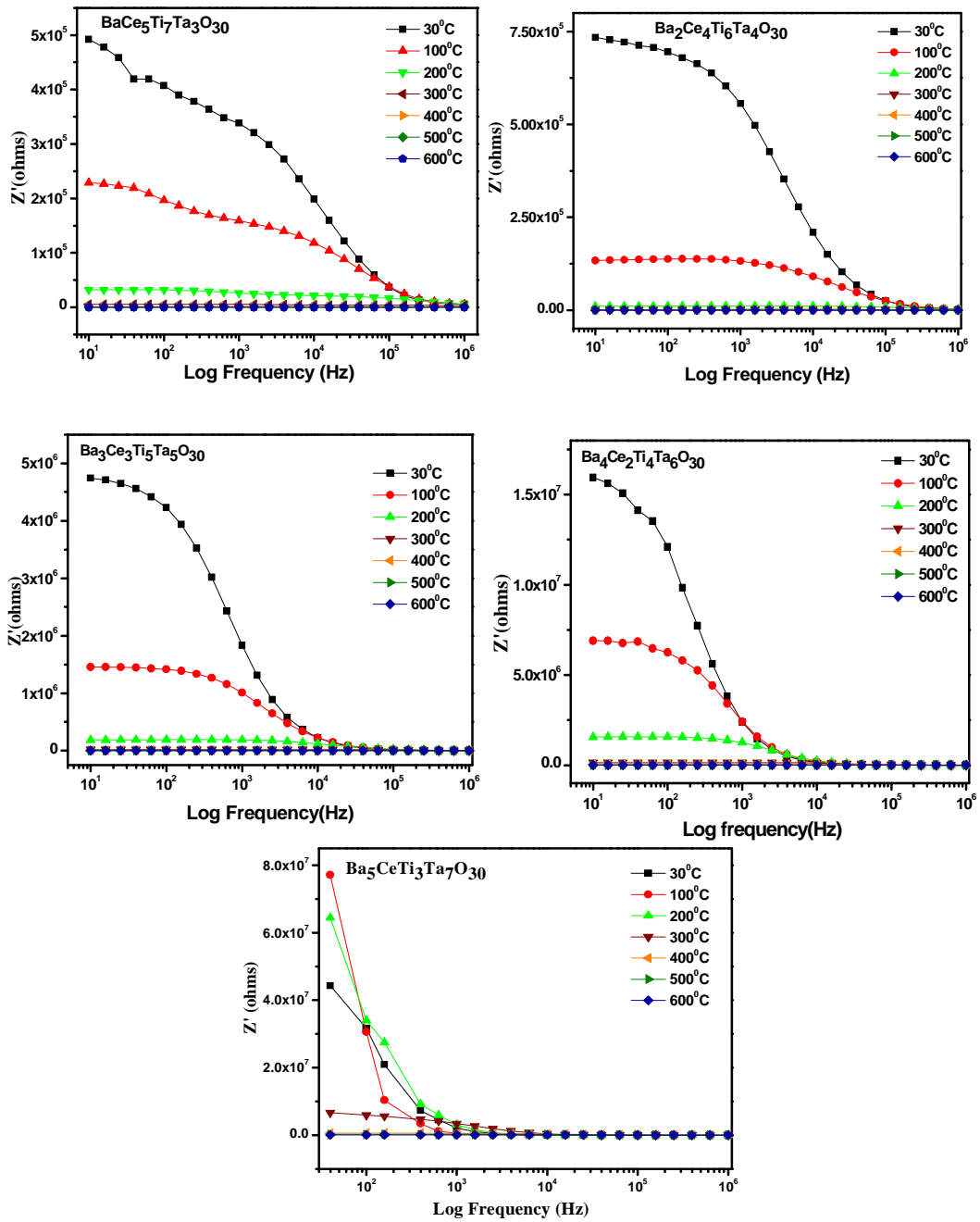
Fig. 7.4 Impedance curves of real component (Z') as a function of log frequency at various temperatures for various compositions in Ba-Ce-Ti-Ta-O system.
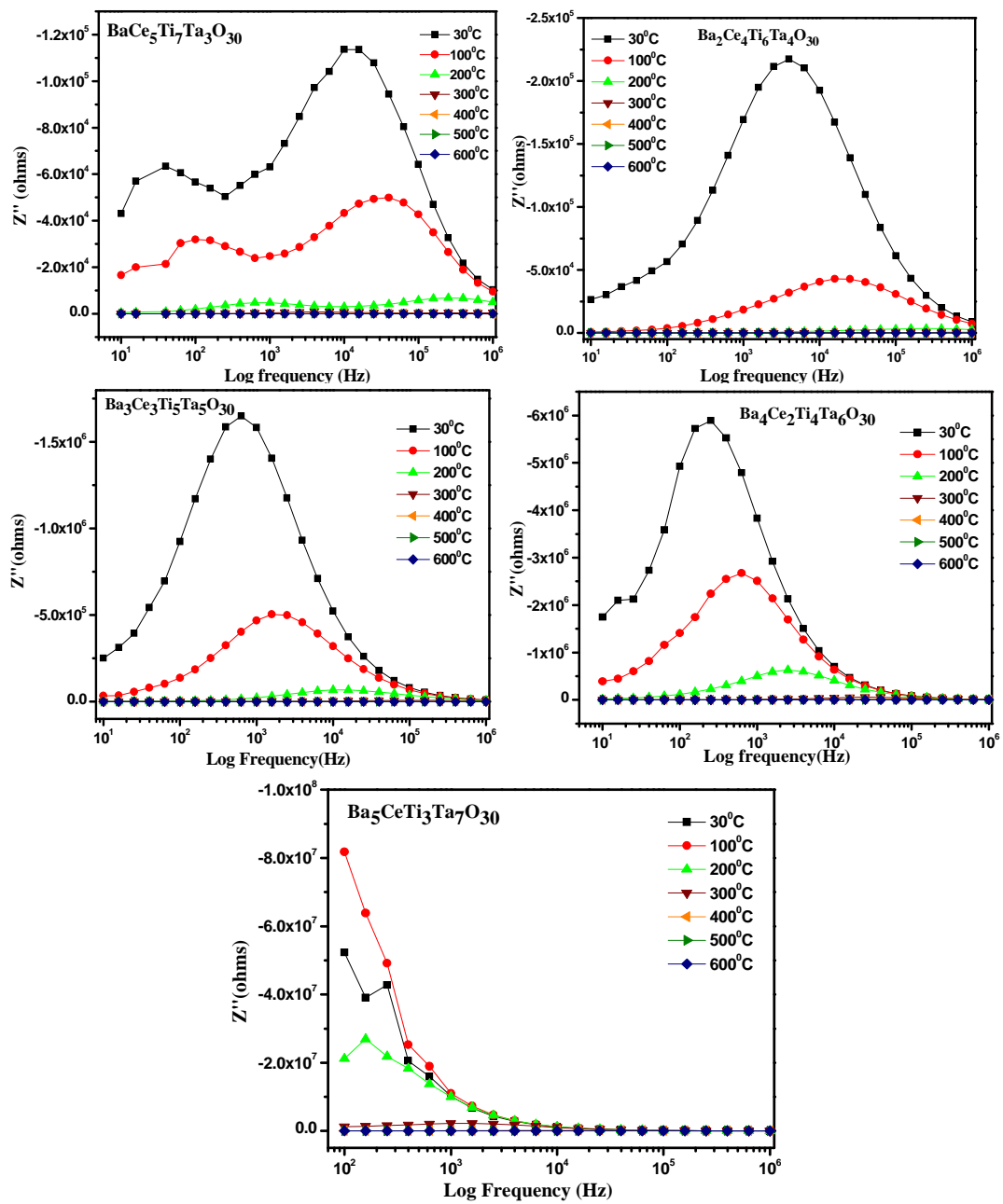
Fig. 7.5 Impedance curves of imaginary component (Z'') as a function of log frequency at various temperatures for various compositions in Ba- Ce-Ti-Ta-O system.
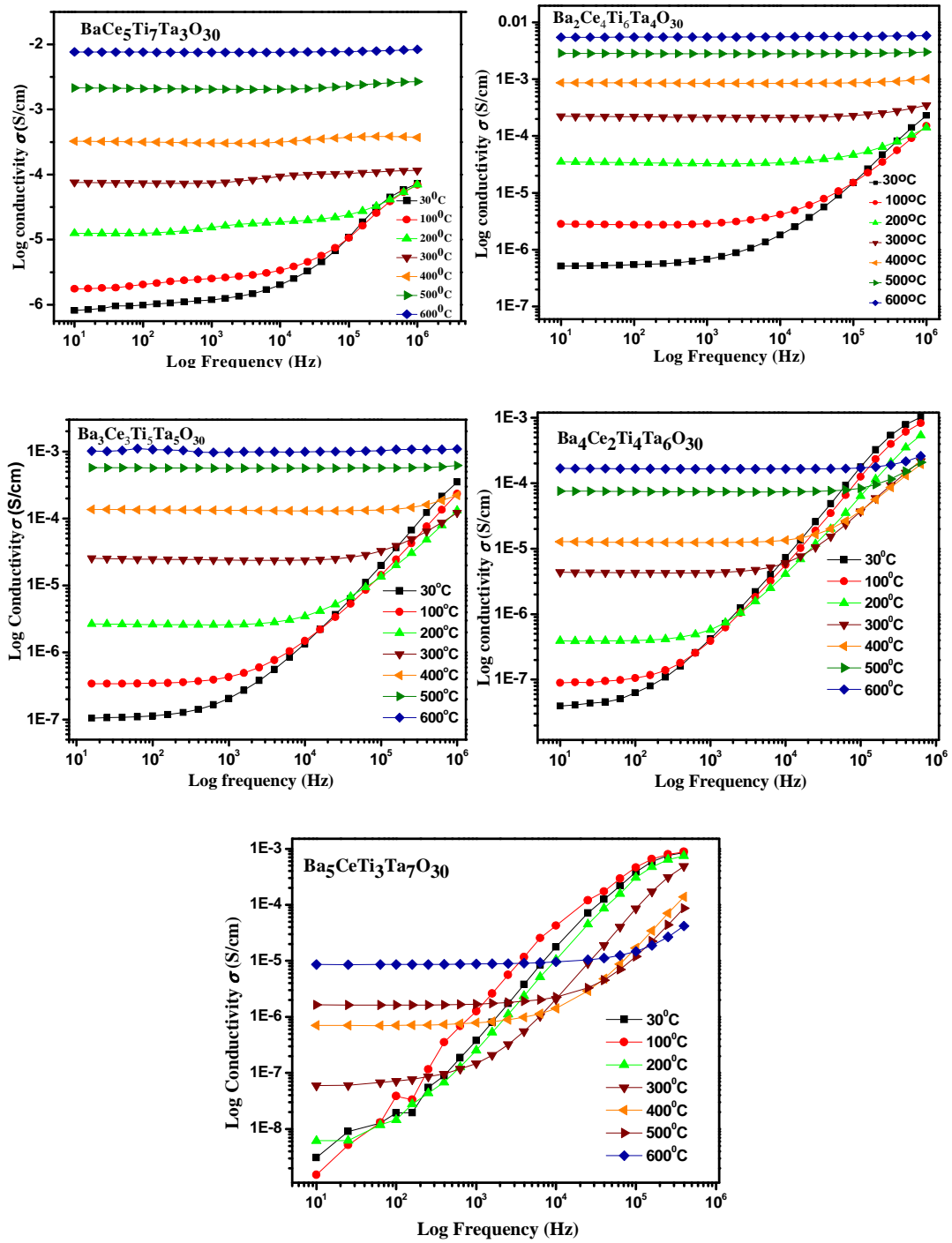
Fig. 7.6 Impedance curves of log ac conductivity (σ) as a function of log frequency at various temperatures for Ba-Ce-Ti-Ta-O system.

Fig. 7.6 shows the ac conductivity plots (log σ) versus log f over a wide range of temperatures. All the curves show frequency – independent plateau corresponding to dc conductivity effects. It is known that ac conductivity is dependent on frequency in fast ionic conductors. The conductivity is governed by the Jonscher's universal power law [Jonscher 1977].

$$\sigma(\omega) = \sigma_{dc} + A\omega^n \qquad (7.2)$$

Where $\sigma_{a.c.}(\omega)$ is the conductivity at frequency ω, σ_o is the dc term associated to the mobile charge, A is a frequency independent and temperature-dependent parameter and n is the slope of high frequency dispersion data (n assumes a value between 0 and 1).

It is very clear from Fig. 7.6 that the conductivity behaviour exhibited by the compound does not fit this simple equation. There is a visible change in the slopes as we go from lower frequency region to the higher frequency region. Hence in this system two slopes can be drawn one in the low plateau region and other in the dispersion region. Therefore the frequency dependent ac conductivity can be characterized using the two term power relation

$$\sigma(\omega) = \sigma_0 + A_1\omega^{n_1} + A_2\omega^{n_2} \qquad (7.3)$$

Again A_1 and A_2 are frequency independent and temperature dependent constants. The slopes n_1 and n_2 will be, n_1 can be $0 \leq n_1 \leq 1$ and n_2 can be $0 \leq n_2 \leq 2$. The term σ_0 corresponding to the translational hopping gives the long range

electrical transport (i.e dc conductivity) in the long time. The second term, $A_1\omega^{n_1}$ characterizes the low frequency region and corresponds to the translational hopping motion (short range hopping), whereas the one at high frequencies $A_2\omega^{n_2}$ corresponds to a localized or reorientational hopping or hopping of electron back and forth between two charged defects [Funke 1993]. Discussions on the conductivity mechanism are given in chapter 3 (Sec.3.3.4).

7.3.5 Electrical conductivity and NTC thermistor characteristics
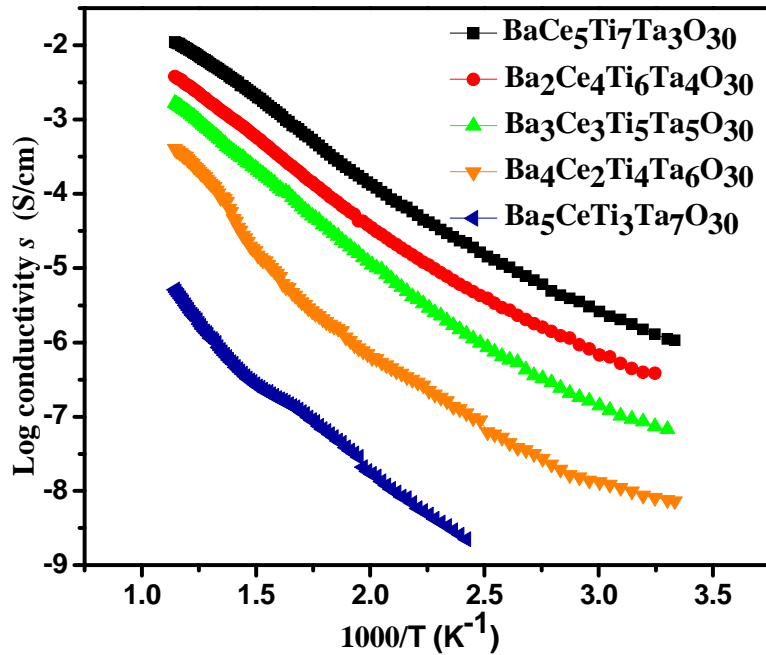
Fig.7.7 Variation of log conductivity (σ) vs. reciprocal of temperature for Ba-Ce-Ti-Ta-O system

Figure 7.7 shows the electrical conductivity (log σ) as a function of absolute temperature (1000/T). The nature of the variation obeys the Arrhenius equation σ=σ₀exp (-Ea/K_BT), where Ea is the activation energy, K_B is Boltzmann constant, T is the absolute temperature, and σ_0 is the pre exponential factor. The activation energies of conduction are calculated from the slopes of the plots in the temperature range of 300– 600°C and are listed in Table 7.1. The relation between resistance and temperature for a NTC thermistor is expressed by the following equation.

$$R_T = R_N \exp\left[\beta\left(\frac{T_N - T}{TT_N} \right) \right] \qquad (7.4)$$

Where R_T is the resistance at temperature T, R_N is the resistance at temperature T_N and β is the thermistor characteristic parameter. Rewriting and rearranging the terms of Eq. (7.3), β can be derived as follows:

$$\beta = \left[\frac{TT_N}{T_N - T} \right] \ln\left(\frac{R_T}{R_N} \right) \qquad (7.5)$$

The thermistor sensitivity is defined by the temperature coefficient of resistance α, which can be expressed as a function of the β parameter, according to the following equation:

$$\alpha = \left(\frac{1}{R} \right) [d(R)/dT] = -\beta/T^2 \qquad (7.6)$$

Compounds	Lattice parameter		β(K)	α (K^{-1})		Activation energy (eV)
	a (Å)	c (Å)		300 °C	600°C	
BaCe$_5$Ti$_7$Ta$_3$O$_{30}$	12.3764	3.8899	5038	0.0153	0.0066	0.438
Ba$_2$Ce$_4$Ti$_6$Ta$_4$O$_{30}$	12.3714	3.8874	5453	.0166	0.0072	0.472
Ba$_3$Ce$_3$Ti$_5$Ta$_5$O$_{30}$	12.3755	3.8886	5816	0.0177	0.0076	0.493
Ba$_4$Ce$_2$Ti$_4$Ta$_6$O$_{30}$	12.4066	3.8964	6410	0.01952	0.0084	0.565
Ba$_5$CeTi$_3$Ta$_7$O$_{30}$	12.1192	4.0449	6741	0.0205	0.0088	0.584

Table 7.1 Lattice parameter, β constant, α and Activation Energy for various compositions in Ba–Ce–Ti–Ta–O system.

Considering the Arrhenius plot in Fig.7.8, the α and β parameters were calculated using the above equations. The values were calculated in the temperature range from 30°C to 600°C, and are presented in Table 7.1. The β value of the different compositions lies in the range of 5000–7000 K. The above results suggest that the electrical characteristics can be tuned to the desired value by changing the cerium concentration in the compound. It is observed that these values are in the desirable range of high-temperature thermistors [Houivet D *et al* 2004]. The aging tests at 500°C reveal that the variation of the aging coefficient (ΔR/R) is 1–2% for the time period of 500 h.

However, more rigorous tests such as electrical characteristics for repeated thermal cycles and long duration have to be performed to qualify as a thermistor device.

7.4 Conclusions

A series of new NTC ceramic oxides in Ba – Ce – Ti – Ta - O system has been prepared through solid state route. The powder X-ray diffraction and Raman spectroscopy analyses showed that all these compounds belong to tetragonal tungsten bronze type structure with the space group *P4bm.* These compounds having good NTC characteristics in a wide range of temperature may find application in devices like high temperature thermistors.

CHAPTER 8

CONCLUSIONS AND FUTURE SCOPE OF THE WORK

8.1 Significant Conclusions

A new class of semiconducting ceramics in different crystal systems: pyrochlore, powellite and tetragonal tungsten bronze have been designed by exploiting the variable valency of cerium (Ce). The effect of cerium concentration on the structure, microstructure and electrical properties of these quaternary oxides has been studied. The possibility of these oxides as NTC thermistor for high temperature sensing is also explored. The major conclusions drawn from the study is presented in this chapter.

1. The semiconducting nature of the compound is due to the conversion of Ce^{4+} to Ce^{3+} in the lattice to maintain the oxygen stoichiometry in the structure. The conductivity mechanism is studied using Impedance spectroscopy.

2. The X-ray photoelectron analysis proves that cerium gets stabilized in 3+ state in all the compositions.

3. Cerium containing single phase pyrochlores have been synthesized by introducing displacive disordering in the system.

4. The microstructure analysis of the $(CaCe_{0.75}Ti_{0.25})$ $(Ti_{1.25}M_{0.75})O_7$ and $(Ca_{0.75}CeTi_{0.25})(Ti_{1.5}M_{0.5})O_7$ (M = Nb or Ta) ceramics reveals that the sintering temperature and in turn the grain morphology influences the electrical properties.

5. Enhancement of the thermistor parameters are observed with rare-earth (Gd, Sm and Y) substitution in $(Ca_{0.75}CeTi_{0.25})(Ti_{1.5}Ta_{0.5})O_7$ ceramic. The electrical properties reveal that cerium is the main contributor of conductivity and fine tuning of thermistor constant (β value) is possible with suitable amount of rare earth substitution.

6. Powellite structured quaternary NTC ceramics have been reported for the first time.

7. Tetragonal tungsten bronze ceramics in Ba-Ce-Ti-Ta-O system has also been studied for NTC thermistor applications.

8. The β constant (300°C to 600°C) of 5000 K–11000K provides a sensitivity α in the range of -0.6% K^{-1} to -1.5% K^{-1} at 600°C. These values are in the admissible range of a high temperature NTC thermistor.

9. The aging factor is found to be in the range of 1-3% at 500°C for a period of 500h.

10. The NTC parameters can be tuned to the desired value by changing the Ce concentration in the composition.

11. These ceramics fulfill the requirements of a material for high temperature NTC applications.

8.2 Future scope of this work

1. The synthesized semiconducting oxides having low band gap may exhibit good photocatalytic properties. The possibility of these compounds for Hydrogen production through photoelectrolysis of water and as photocatalyst for water purification can be explored.

2. The conductivity mechanism and its dependency on the crystal structure can be studied in detail.

3. NTCR thermistors operating at very high temperatures such as 1000°C and above can be developed via tuning of the thermistor characteristics by adjusting the Ce content in the composition.

LIST OF PUBLICATIONS

Publications in refereed journals

1. Pyrochlore type semiconducting ceramic oxides in Ca – Ce – Ti – M - O system(M = Nb or Ta) – structure, microstructure and electrical properties

   M. Deepa, P.Prabhakar Rao, A.N Radhakrishnan, K.S.Sibi, Peter Koshy

   Materials Research Bulletin, Volume 44, Issue 7, 1 July 2009, Pages 1481-1488

2. New NTC ceramics in Ca-Ce-Nb-M-O (M = Mo or W) system

   M. Deepa, P. Prabhakar Rao, S.Sumi, A.N. Radhakrishnan, Peter Koshy

   Journal of the American Ceramic Society, Volume 93, Issue 6, June 2010, Pages 1576 - 1579

3. Order–disorder phase transformations in quaternary pyrochlore oxide system: Investigated by X-ray diffraction, transmission electron microscopy and Raman spectroscopic techniques

   A.N. Radhakrishnan, P. Prabhakar Rao, K.S. Sibi, **M. Deepa**, Peter Koshy

   Journal of Solid State Chemistry, Volume 182, Issue 8, August 2009, Pages 2312 - 2318

4. Novel powellite-based red-emitting phosphors: $CaLa_{1-x}NbMoO_8:x Eu^{3+}$ for white light emitting diodes

   MariyamThomas, P.PrabhakarRao, **M.Deepa**, M.R.Chandran, Peter Koshy,

   Journal of Solid State Chemistry, Volume 182, 2009 Pages 203–207

5. Oxide ion conductivity and relaxation in $CaREZrNbO_7$ (RE = La, Nd, Sm, Gd, and Y) system

   K.S. Sibi, A.N. Radhakrishnan, **M. Deepa**, P. Prabhakar Rao, Peter Koshy

   Solid State Ionics, Volume 180, Issues 20-22, 17 August 2009, Pages 1164-1172

6. Structural and electrical properties of nonstoichiometric semiconducting

Pyrochlores in Ca-Ce-Ti-Nb-O system

M. Deepa, P. Prabhakar Rao, S. Sumi, M.R. Chandran, Peter Koshy

Materials Chemistry and Physics (under review)

7. Electrical conductivity and Impedance spectroscopy studies of aeschynite type semiconducting oxides: $CeTiMO_6$ (M = Nb or Ta)

S. Sumi, P. Prabhakar Rao, **M. Deepa**, Peter Koshy

Journal of Applied Physics (Accepted Manuscript)

8. Enhancement of NTC thermistor characteristics by rare earth (Gd,Sm and Y) doping of in$(Ca_{0.75}CeTi_{0.25})(Ti_{1.5}Ta_{0.5})O_7$ ceramic

M. Deepa, P. Prabhakar Rao, S. Sumi, M.R. Chandran, Peter Koshy

(Manuscript under preparation)

9. Tetragonal tungsten bronze structured NTC ceramics in Ba-Ce-Ti-Ta-O system

M. Deepa, P. Prabhakar Rao, S. Sumi, Peter Koshy

(Manuscript under preparation)

Papers Presented in Conferences:

1. Novel semiconducting oxide in A-Ce-M- O (A= Na, K; M=Nb, Ta) system

M. Deepa, P.Prabhakar Rao and Peter Koshy

Presented in International conference on Advanced Materials and composites (ICAMC-07) held at Thiruvananthapuram during 24-26th October 2007

2. New semiconducting Pyrochlore type Oxides in Ca-Ce-Ti-Nb-O system-their structure, microstructure and Electrical conductivity studies.

M.Deepa, P.Prabhakar Rao and Peter Koshy

Presented in National Conference on Electron Microscope & Allied Fields and XXIX Annual Meeting of EMSI (EMSI NC-2007) held at University of Delhi during 26-28th November 2007.

3. Structure Property Correlation of New Semi conducting Pyrochlore type Oxides in Ca – Ce –Ti – M – O (M=Nb or Ta) System.

   M.Deepa, P.Prabhakar Rao and Peter koshy

   Presented in National Conference on Electron Microscope & Allied Fields and XXX Annual Meeting of EMSI (EMSI NC-2009) held at Bundelkhand University, Jhansi during 17-20th January 2009

4. Effect of Rare earth (Gd, Sm, Y) doping on the Electrical properties of Ca-Ce-Ti-Ta-O high temperature NTC Thermistors

   M. Deepa, S. Sumi, P. Prabhakar Rao, M.R.Chandran and Peter Koshy

   Presented in International conference on Advanced Functional Materials (ICAFM-2009) held at Thiruvananthapuram during 9-10th December 2009

5. Impedance Spectroscopy of Semiconducting Oxides:CeTiMO6 (M= Nb or Ta)

   S. Sumi, P. Prabhakar Rao, **M. Deepa**, M.R. Chandran, Peter Koshy

   Presented in International conference on Advanced Functional Materials (ICAFM-2009) held at Thiruvananthapuram during 9-10th December 2009

AWARD

   Best paper poster award for "Effect of Rare earth (Gd, Sm, Y) doping on the Electrical properties of Ca-Ce-Ti-Ta-O high temperature NTC Thermistors"

   M. Deepa, S. Sumi, P. Prabhakar Rao, M.R.Chandran and Peter Koshy

   Presented in International conference on Advanced Functional Materials (ICAFM-2009) held at Thiruvananthapuram during 9-10th December 2009

REFERENCES

Abrahams S. C, Jamieson P. B, Bernstein J. L, "Ferroelectric tungsten bronze-type crystal structures. III. potassium lithium niobate $K_{(6-x-y)}Li_{(4+x)}Nb_{(10+y)}O_{30}$" *J. Chem. Phys.* **54** (1979) 2355.

Achary S. N., Patwe S. J., Mathews M. D., Tyagi A. K., "High temperature crystal chemistry and thermal expansion of synthetic powellite ($CaMoO_4$): a high temperature X-ray diffraction (HT-XRD) study," *J. Phys. Chem. Solids,* **67** (2006) 774.

Amzallag E., Chang T. S., Pantell R. H, Feigelson R. S, "Raman Scattering by $Sr_xBa_{1-x}Nb_2O_6$" *J. Appl. Phys.* **42** (1971) 3254.

Amstel J, "Electrical resistance material"; *U.S. Patent* #2111708 (1935).

Ashok Kumar, Singh B P, Choudhary R N P, Thakur A.K "Characterization of electrical properties of Pb-modified $BaSnO_3$ using impedance spectroscopy" *Mater. chem. Phys.* **99** (2006) 150.

Astheimer W., Wormser E.M., "High speed infrared radiometers" *J. Opt. Soc. Am.* **49** (1959) 179.

Ayer Jr. W. J., Rose K. "Notes on the negative temperature coefficient of resistance and superconductivity of niobium nitride thin films" *Phys. Lett. A*, **45** (1973) 333.

Basu A., Brinkman W., Hashemi T., "NTC characteristics of bismuth based ceramic at high temperature" *Int .J. Inorg. Mater*, **3** (2001) 1219

Becker J. A, Green C. B, Pearson G. L, "Properties and uses of thermistors—thermally sensitive resistors", *Bell System Tech. J., ***26** (1947)170.

Boccaccini A. R, Bernardo E, Blain L, Boccaccini D. N. "Borosilicate and lead silicate glass matrix composites containing pyrochlore phases for nuclear waste encapsulation" *J. Nucl. Mater.* **327** (2004) 148.

Brixner L. H., Blasse G.,"High-resolution X-Ray excited Gd^{3+} emission in some fergusonite-type $LnNbO_4$ compounds," *Mater. Res. Bull.,* **25** (1990) 1003.

Brook R. J, "Concise encyclopaedia of advanced ceramic materials", *The MIT Press*, Cambridge, Massachusetts (1990).

Burns G., Axe J.D., O'kane D.F., "Raman measurements of $NaBa_2Nb_5O_{15}$ and related ferroelectrics" *Solid State Commun.* **7** (1969) 933.

Carina Börrnert, Wilder Carrillo-Cabrera, Paul Simon, Hubert Langbein "$V_{2.38}Nb_{10.7}O_{32.7}$: A V_2O_5–Nb_2O_5 mixed oxide tunnel structure related to the tetragonal tungsten bronzes" *J. Solid State Chem.* **183** (2010)1038.

Chatterjee S., Biljana D. S.,. Maiti H. S "Effect of additives and powder preparation techniques on PTCR properties of barium titanate" *Mater.Chem.Phys.***78** (2003) 702.

Cheremisinoff N. P, "Hand book of ceramics and composites" *Marcel Dekker INC*, New York, (1990).

Chi E. O, Gandini A., Ok K.M., Zhang L., Halasyamani P. S. "Syntheses, structures, second-harmonic generating, and ferroelectric properties of tungsten bronzes: $A_6M_2M'_8O_{30}$ (A = Sr^{2+}, Ba^{2+}, or Pb^{2+}; M = Ti^{4+}, Zr^{4+}, or Hf^{4+}; M' = Nb^{5+} or Ta^{5+})" *Chem.Mater.*,**16** (2004) 3616.

Csete de Györgyfalva G. D. C., Nolte A. N, Reaney I. M., "Correlation between microstructure and conductance in NTC thermistors produced from oxide powders" *J. Eur. Ceram. Soc.* **19** (1999) 857.

Cullity B. D., "Elements of X-ray diffraction" *Addison Wesley publishing company*, Inc. USA, (1959).

Deepa M., Prabhakar Rao P., Radhakrishnan A. N., Sibi K. S, Peter Koshy, ''Pyrochlore type semiconducting ceramic oxides in Ca–Ce–Ti–M–O system (M=Nb or Ta)-structure, microstructure and electrical properties,'' *Mater. Res. Bull.*, **44** (2009) 1481.

de Gyorgyfalva G., Reaney I. M., "Decomposition of $NiMn_2O_4$ spinel: an NTC thermistor material," *J. Eur. Ceram. Soc.,* **21** (2001) 2145.

Dengwei J, Liejin G, Liang Z, Ximin Z, Huan L, Mingtao L, Shaohua S, Guanjie L, Xiaowei H, Xianghui Z, Kai Z, Lijin M, Penghui G, "Efficient

solar hydrogen production by photocatalytic water splitting: From fundamental study to pilot demonstration" *Int. J. Hydrogen Energy,* Article in press, Available online 9 February 2010.

Ding H., Ge H., Liu J., "High performance of gas identification by wavelet transform-based fast feature extraction from temperature modulated semiconductor gas sensors," *Sens. Actuat. B-Chem.,* **107** (2005) 749.

Duan C.J., Wang X. J., Otten W. M., Delsing A. C. A., Zhao J. T., Hintzen H. T. "Preparation, electronic structure and photoluminescence properties of Eu^{2+}- and Ce^{3+}/Li+-activated alkaline earth silicon nitride $MSiN_2$ (M = Sr, Ba)." *Chem.Mater.* **20** (2008) 1597.

Dunitz J. D, Orgel L. E, "Electronic properties of transition-metal Oxides –II: Cation distribution amongst octahedral and tetrahedral sites," *J. Phys.Chem. Solids*, **3** (1957) 318.

Elisabetta D.B, Enrico T, Manuela B, Vega K, R. Vasant Kumar, "Solid state ceramic gas sensors based on interfacing ionic conductors with semiconducting oxides" *J. Eur. Ceram. Soc.* **20** (2000) 2691.

Elliott S. R., " A.C. conduction in amorphous chalcogenide and pnictide semiconductors" *Adv. Phys* **36** (1987) 135.

Fan R., Chen X. H, Gui Z, Sun Z, Li S. Y, Chen Z. Y, "Chemical synthesis and electronic conduction properties of sodium and potassium tungsten bronzes" *J. Phys. Chem. Solids* **61** (2000) 2029.

Faraday M, ''On conducting power generally'' *Experimental Researches in Electricity,* Royal Institution, London, (1833) 119.

Feltz A., "Perovskite forming ceramics of the system $Sr_xLa_{1-x} Ti^{IV}_{x+y}Co^{II}_yCo^{III}_{1-x-2y}O_3$ for NTC thermistor applications", *J. Eur. Ceram. Soc.,* **20** (2000) 2367.

Feteira A., "Negative temperature coefficient resistance (NTCR) ceramic thermistors: An industrial perspective" *J. Am. Ceram. Soc.*, **92** (2009) 967.

Filonenko V. P., Grenthe C., Nygren M., Sundberg M., Zibrov I. P "Structure and thermal stability of $La_{0.10}WO_{3+y}$; A hexagonal tungsten bronze related phase formed at high pressure" *J. Solid State Chem.***163** (2002) 84.

Francisco M. S. P., Mastelaro V. R., P. A. P. Nascente, and A. O. Florentino, "Activity and characterization by XPS, HR-TEM, Raman Spectroscopy, and BET surface area of CuO/CeO_2-TiO_2 Catalysts," *J. Phys. Chem. B,* **105** (2001)10515.

Frost R. L., Bouzaid J., Butler I. S., "Raman spectroscopic study of the molybdate mineral *szenicsite* and comparison with other paragenetically

related molybdate minerals," *Spectroscopy Lett.: An Inter.J. Rapid Comm.,* **40** (2007) 603.

Funke K., "Jump relaxation in solid electrolytes" *Prog. Solid State Chem.* **22** (1993) 111.

Gaines R. V, Skinner H. C. W, Foord E. E, Mason B, Rosenzweig A, "Dana's new mineralogy", *Wiley,* New York, (1997) 8th edition 341–352.

Glerup, M., Nielsen O. F., Poulsen F.W, "The structural transformation from the pyrochlore structure, $A_2B_2O_7$, to the fluorite structure, AO_2, studied by Raman spectroscopy and defect chemistry modeling." *J. Solid State Chem.* **160** (2001) 25.

Goldstein J. I, Newbery D. E, Echlin P, Joy D. C, Fiori C, Lifshin E, "Scanning electron microscopy and X-ray microanalysis", *Plenum press*, New York, 1981.

Goodhew P. J, Humphreys F. J, Beanland R, "Electron microscopy and analysis" 3rd Edn. *Taylor & Francis*, London, 2001.

Grenthe C., Sundberg M., Filonenko V. P., Zibrov I. P. "Effects of pressure and temperature on the formation of tungsten-bronze-related phases, RE_xWO_{3+y},with RE=La and Nd"*J. Solid State Chem.* **168** (2002) 284.

Guo J., Dong C., Yang L., Fu G , " Crystal structure and electrical properties of new tungsten bronzes: $B_xWO_3(0.01 \leq x \leq 0.08)$" *Mater.Res.Bull.* **42** (2007) 1384.

Gupta A, Aggarwal R, Gupta P, Dutta T, Roger J. Narayan, Narayan J, "Semiconductor to metal transition characteristics of VO_2 thin films grown epitaxially on Si (001)" *Appl.Phys.Lett*. **95** (2009) 111915.

Hammond C, "The basics of crystallography and diffraction" 2nd Edn. *Oxford university press*, London, 2001.

Hazen R. M., Finger L.W., J. W. E. Mariathasan, "High-pressure crystal chemistry of scheelite-type tungstates and molybdates," *J. Phys. Chem. Solids,* **46** (1985) 253.

Hernandez T., Martın P. "Microstructural and optical features of a Eu-monazite" *J. Eur. Ceram. Soc.***27** (2007) 109.

Hess, N. J., Begg B. D., Conradson S. D., McCready D. E., Gassman P. L., Weber. W. J, "Spectroscopic investigations of the structural phase transition in $Gd_2(Ti_{1-y}Zr_y)_2O_7$ pyrochlores." *J.Phys.Chem.B* **106** (2002) 4663.

Holze R, "Impedance spectroscopy [E. Barsoukov and J.R. Macdonald (Eds.)]" *J. Solid State Electrochem*. **12** (2008) 651.

Houivet D., Bernard J., Haussonne J.M. "High temperature NTC ceramic resistors (ambient–1000°C)" *J. Eur.Ceram.Soc.***24** (2004) 1237.

http://rruff.geo.arizona.edu/AMS/xtal_data/DIFfiels/12045.txt.

Huiling D, Xi Y. "Structural trends and dielectric properties of Bi-based pyrochlores" *J. Mater. Sci.: Mater. Electron.* **15** (2004) 613.

Hussain A, Kihlborg L. "Crystal physics, diffraction, theoretical and general crystallography" *Acta Cryst.* A **32** (1976) 551.

Istomin, S. Y., O. G. D'Yachenko, E. V. Antipov, G. Svensson "Synthesis and characterization of reduced niobates $CaLnNb_2O_7$, Ln = Y, Nd with a pyrochlore structure." *Mater. Res. Bull.***32** (1997) 421.

Jamieson P. B., Abrahams S. C., Bernstein J. L. "Ferroelectric tungsten bronze-type crystal structures. I. Barium Strontium niobate $Ba_{0.27}Sr_{0.75}Nb_2O_{5.78}$" *J. Chem. Phys*. **48** (1968) 5048.

Jonscher A. K., "The 'universal' dielectric response" *Nature* **267** (1977) 673.

Justin M. Varghese, Seema A., Dayas K.R. "Microstructural, electrical and reliability aspects of chromium doped Ni–Mn–Fe–O NTC thermistor materials" *Mater. Sci. Eng., B* **149** (2008) 47.

Kharton V.V., Marques F.M.B, "Mixed ionic-electronic conductors: effects of ceramic microstructure on transport properties" *Curr. Opin. Solid ST. M.* **6** (2002) 261.

Kihlborg L., Blomqvist H., Sundberg M. "Low members of the intergrowth tungsten bronze family by partial substitution of molybdenum for tungsten" *J. Solid State Chem.* **162** (2001) 341.

Kimura H., Noda Y., Kohn K. "Spin-driven ferroelectricity in the multiferroic compounds of RMn_2O_5" *J. Magn. Magn. Mater.* **321**(2009) 854.

Kosacki I., Tuller H. L., "Donor-doped $Gd_2Ti_2O_7$ as a semiconductor-type oxygen sensor" *Sensors and Actuators B: Chem.* **25** (1995) 370.

Kravchenko E. A, Orlov V. G, "Magnetism of mixed bismuth–boron oxides. ^{209}Bi NQR of $Bi_3B_5O_{12}$ in external magnetic fields" *Phys. B: Conden. Matt.*, **312-313** (2002) 772.

Kwon Y, Hwang Y. K, Kwon Y.U "Syntheses and electrical properties of tetragonal tungsten bronze type solid solution $Ba_{6-x}La_x$) $Nb_{10}O_{30+\delta}$ (x = 0, 1, 2, 3) and $Sr_6Nb_{10}O_{30}$" *Mater. Res. Bull.* **32** (1997)1495.

Lee J.H. "Gas sensors using hierarchical and hollow oxide nanostructures: Overview" *Sens. Actuators, B:Chem.,* **140** (2009) 319.

Lei L.W., Fu Z.Y., Zhang J.Y. "Influence of sintering temperature on microstructure and magnetotransport properties of $La_{0.8}Na_{0.2}MnO_3$ ceramics" *Mater. Lett.* **60** (2006) 970.

Lian J., Wang L. M., Wang S. X., Chen J., Boatner L. A., Ewing R. C. "Nanoscale manipulation of pyrochlore: new nanocomposite ionic conductors" *Phys. Rev. Lett.* **87** (2001)145901.

Licia M. Robin W. G., Kurt E. S., "Disorder in pyrochlore oxides" *J. Am .Ceram .Soc*. **83** (2000) 1873.

Liu X., Luo Y, Li X, "Electrical properties of BaTiO$_3$-based NTC ceramics doped by BaBiO$_3$ and Y$_2$O$_3$" *J. Alloys Compd.,* **459** (2008) 45.

Long D. A., "Raman Spectroscopy" *Mc Graw Hills*, New York, 1977.

Lu T, Steele B. C. H, "Electrical conductivity of polycrystalline BiVO$_4$ samples having the scheelite structure" *Solid State Ionics* **21** (1986) 339.

Luan J., Cai H., Zheng S., Hao X., Luan G., Wu X., Zou Z., "Structural and photocatalytic properties of novel Bi$_2$GaVO$_7$" *Mater.Chem.Phys* **104** (2007) 119.

Macdonald J.R., "Impedance spectroscopy", *John Wiley and Sons*, New York, (1987).

Macher K. R., O. Fruhwirth, K. Gatterer, Herzog G. W., "Perovskite versus spinel type NTC materials for application at elevated temperatures" *J. Microelectron. Electron. Components Mater.,* **26** (1996)79.

Machida M, Yabunaka J, Kijima T, "Synthesis and photocatalytic property of layered perovskite tantalates, $RbLnTa_2O_7$ (Ln = La, Pr, Nd, and Sm)" Chem. Mater. **12** (2000) 812.

Malato S, Fernández-Ibáñez P, Maldonado M.I, Blanco J, Gernjak W, "Decontamination and disinfection of water by solar photocatalysis: recent overview and trends*" Catal. Today* **147** (2009) 1.

Masetti E, Dini D., Decker F, "The electrochromic response of tungsten bronzes M_xWO_3 with different ions and insertion rates" *Sol. Energy Mater. Sol. Cells*., **39** (1995) 301.

Matjaz valant, Peter K. Davies , "Crystal chemistry and dielectric properties of chemically substituted $(Bi_{1.5}Zn_{1.0}Nb_{1.5})O_7$ and $Bi_2(Zn_{2/3}Nb_{4/3})O_7$ pyrochlores" *J. Am.Ceram.Soc.* **83** (2000) 147.

McGee T. D, "Principles and methods of temperature measurement" *Wiley-IEEE*, New York, 1988.

McHale A. E., "Processing additives, engineering materials hand book ceramics and glasses, vol.4", *The Materials Information Society*, USA 1991.

Meng Q. B., Wu Z. J., Zhang S. Y., "Dependence of superconducting temperature on chemical bond parameters in $YBa_2Cu_3O_{6+\delta}$ (δ=0-1),"*J. Phys. Chem. Solids,* **59** (1998) 633.

Monica Lira-Cantu, Frederik C. Krebs, "Hybrid solar cells based on MEH-PPV and thin film semiconductor oxides (TiO_2, Nb_2O_5, ZnO, CeO_2 and CeO_2–TiO_2): Performance improvement during long-time irradiation" *Sol. Energy Mater. Sol. Cells*, **90** (2006) 2076.

Moore D. M., Reynolds Jr., R. C, "X–ray diffraction and the identification and the analysis of clay minerals", *Oxford University Press*, New York, 1989.

Mullins D. R., Overbury S.H., Huntley D. R., "Electron spectroscopy of single crystal and polycrystalline cerium oxide surfaces" *Surface Sci.* **409** (1998) 307.

Nair K. R, Prabhakar Rao P, Sameera S, Mohan V. S, Chandran M. R, P. Koshy, "New powellite type oxides in Ca-R-Nb-Mo-O system (R=Y, La, Nd, Sm or Bi) - Their synthesis, structure and dielectric properties," *Mater. Lett.,* **62** (2008) 2868.

Nakano T, Momono N , Matsuzaki T, Nagata T, Yokoyama M, Oda M and Ido M. "Effects of Zn substitution on magnetic properties and superconductivity in $La_{2-x}Sr_xCuO_4$" *Phys.C: Superconduct.* **317-318** (1999) 575.

Nobre M. A. L., Lanfredi S "New evidence of grain boundary phenomenon in $Zn_7Sb_2O_{12}$ ceramic: an analysis by impedance spectroscopy" *Mater.Lett.,* **50** (2001) 322.

Nobre M. A. L., Lanfredi S, ''Thermistor ceramic with negative temperature coefficient based on $Zn_7Sb_2O_{12}$: An inverse spinel-type phase,'' *Appl. Phys. Lett*., **81** (2002) 451.

Nobre M. A. L., Lanfredi S., "Negative temperature coefficient thermistor based on $Bi_3Zn_2Sb_3O_{14}$ ceramic: An oxide semiconductor at high temperature" *Appl. Phys. Lett.* **82** (2003) 2284.

Nowotny M.K, Bogdanoff P, Dittrich T, Fiechter S, Fujishima A, Tributsch H, "Observations of p-type semiconductivity in titanium dioxide at room temperature" *Mater. Lett.,* **64** (2010) 928.

Nguyen B, Liu Y, Withers R. L, "The local crystal chemistry and dielectric properties of the cubic pyrochlore phase in the $Bi_2O_3 – M^{2+} O – Nb_2O_5$ ($M^{2+}= Ni^{2+}$ and Mg^{2+}) systems" *J. Solid State Chem.* **180** (2007) 549.

Nguyen B, Liu Y, Withers R.L, "Relaxor dielectric properties of a $(Ca_{1.5}Ti_{0.5})(NbTi)O_7$ 'misplaced-displacive' cubic pyrochlore synthesized via metallorganic decomposition" *Solid State Commun.* **145** (2008) 72.

Park K., "Fabrication and electrical properties of Mn-Ni-Co-Cu-Si oxides negative temperature coefficient thermistors," *J. Am. Ceram. Soc.,* **88** (2005) 862.

Park K., Han I.H "Effect of Al_2O_3 addition on the microstructure and electrical

properties of $(Mn_{0.37}Ni_{0.3}Co_{0.33-x}Al_x)O_4$ $(0{\leq}x{\leq}0.03)$ NTC thermistors" *Mater. Sci. Eng., B* **119** (2005) 55.

Paulauskas I.E, Katz J.E, Jellison Jr G.E, Lewis N.S, Boatner L.A, "Photoelectrochemical studies of semiconducting photoanodes for hydrogen production via water dissociation " *Thin Solid Films*, **516** (2008) 8175.

Peter Koshy, Prasannakumari L, Sebastian M.T "Preparation, characterization and dielectric properties of $Ba_3Ln_3Ti_5Nb_5O_{30}$ (Ln=La, Nd) ceramics" *J. Mater. Sci.: Mater. Electron.* **9** (1998) 43.

Pierre E. D., Barringer E. A., Bowen H. K. "Preparation and sintering behavior of fine-grained Al_2O_3-SiO_2 composite"*J.Am.Ceram.Soc.***68** (1985) C-76.

Plcharski, J., Weiczorek W. "PEO based composite solid electrolyte containing nasicon." *Solid state ionics* **28** (1988) 979.

Polaiz-Barramco A., Gutierrez-Amador M.P., Huanosta A. , Valezuela R., "Phase transitions in ferrimagnetic and ferroelectric ceramics by ac measurements" *Appl. Phys. Lett.* **73** (1998) 2039.

Porter L.C, Appelman E, Beno M. A, Cariss C. S, Carlson K. D, Cohen H, Geiser U, Thorn R. J, Williams J.M. "Synthesis, conductivity, and X-ray photoelectron spectrum of $Bi_2Sr_2CuO_{7+X}$. A new ternary bismuth-

oxide system exhibiting metallic conductivity" *Solid State Commun.* **66** (1988) 1105.

Porto S. P. S., Scott J. F., "Raman Spectra of $CaWO_4$, $SrWO_4$, $CaMoO_4$, and $SrMoO_4$," *Phys. Rev.,* **157** (1967) 716.

Prabhakar Rao P., Ravindran Nair K., Peter Koshy, "$Ba_3Ce_3Ti_5Nb_5O_{30}$—a novel ceramic oxide semiconductor" *Mater. Lett.* **57** (2003) 4127.

Prabhakar Rao P., Liji S. J, Nair K. R., P. Koshy, "$Ca_3Ce_{3-x}M_xTi_7Nb_2O_{26.5}$ (M=Y, Sm or Gd; x=0, 1 or 2)—pyrochlore-type ceramic oxide semiconductors" *Physica B: Condensed Matter,* **349** (2004) 115.

Prabhakar Rao P., Ravindran Nair K., Peter Koshy, Vaidyan V. K., "New dielectric materials based on pyrochlore-type oxides-$Ca_3RE_3Ti_7Ta_2O_{26.5}$ (RE = Pr, Sm, Gd, Dy or Y): Structure, FT-IR spectra, microstructure and dielectric properties" *J. Mater Sci. Mater Electron* **17** (2006) 497.

Prabhakar Rao,. P., Liji S. J., Ravindaran Nair K., Peter Koshy "New pyrochlore-type oxides in Ca-R-Ti-Nb-O system (R=Y, Sm or Gd)--structure, FT-IR spectra and dielectric properties." *Mater.Lett.* **58** (2004) 1924.

Prasad N. V., Prasad G., Bhimasankaran T., Suryanarayana S. V.,Kumar G. S

"Synthesis and electrical properties of $SmBi_5Fe_2Ti_3O_{18}$" *Mod. Phys. Lett. B* **12** (1998) 371.

Rahaman M. N, "Ceramic processing and sintering" 2nd ed., Revised and Extended, Marcel Dekker, New York, (2003).

Ranga Raju M. R., Choudhary R. N. P., "Effect of Zr^{+4} ion substitution on the structural, dielectric and electrical properties of $Sr_5LaTi_3Nb_7O_{30}$ceramics" *J. Mat. Sci.* **39** (2004) 1765.

Ratnakar R. N., Warren K. C., "Progress in photorefractive tungsten bronze crystals," *J. Opt. Soc. Am. B* **3** (1986) 274.

Reddy B. M., Khan A., Yamada Y., Kobayashi T., Loridant S., Volta J.C., "Structural characterization of CeO_2–TiO_2 and V_2O_5/CeO_2–TiO_2 catalysts by Raman and XPS techniques" *J. Phys. Chem. B* **107**(2003) 5162.

Robert M. Hazen L.W. F, Mariathasan J. W. E, "High-pressure crystal chemistry of scheelite-type tungstates and molybdates" *J. Phys. Chem. Solids,* **46** (1985) 253.

Roth R.S, Vanderah T.A, Border P, Grey I.E, Mumme W.G, Cai L, Nino J.C, "Pyrochlore formation, phase relations, and properties in the CaO-TiO_2-$(Nb,Ta)_2O_5$ systems" *J. Solid State Chem.* **181** (2008) 406.

Ruben S, ''Electrical Pyrometer Resistance'' *U.S. Patent* #2021491(1930).

Sarrion M. L. M., Morales M., "Preparation and characterization of NTC

thermistors - Nickel manganites doped with Lithium," *J. Am. Ceram. Soc.,* **78** (1995) 915.

Saruhan, B., P. Francois, Fritscher K., Schulz U,. "EB-PVD processing of pyrochlore-structured $La_2Zr_2O_7$-based TBCs." *Surf. Coat. Technol.***182** (2004)175.

Scarr R.W.A., Setterington R.A., "Thermistors their theory, manufacture and application", *Inst. of Elect. Engrs. (IEE)*, **107 B** (1960) 395–405.

Schilling A., Cantoni M., Guo J. D, Ott H. R. "Superconductivity above 130 K in the Hg-Ba-Ca-Cu-O system" *Nature* **363** (1996) 56.

Schubert K. E, ''Resistor compositions containing pyrochlore-related oxides and cadmium Oxide'' *U.S. Patent* #3560410 (1969).

Segal D., "Chemical synthesis of advanced ceramic materials" *Cambridge University Press*, Cambridge (1991).

Sekhar C. R, Malay K. K, Gupta D. D, "Tin dioxide based transparent semiconducting films deposited by the dip-coating technique" *Surf. Coat. Technol*. **102** (1998) 73.

Sen S., Choudhary R. N. P., "Impedance studies of Sr modified $BaZr_{0.05}Ti_{0.95}O_3$ ceramics" *Mater.Chem.Phys*. **87** (2004) 256.

Severin K. P, "Energy dispersive spectrometry of common rock forming minerals" *Kluver Academic publishers,* Dordrecht, The Netherlands (2004).

Shannon R. D., "Revised effective ionic radii and systematic studies of interatomic distances in halides and chalcogenides" *Acta Crystallogr. A* **32** (1976) 751.

Shi F. N, Meng J. A, Ren Y. F, "Semiconductor to metal transition in $Ln_2Mo_3O_9$ compounds," *Mater. Res. Bull.,* **30** (1995) 1285.

Slater P. R, Irvine J. T. S, "Synthesis and electrical characterisation of the tetragonal tungsten bronze type phases, $(Ba/Sr/Ca/La)_{0.6}M_xNb_{1-x}O_{3-\delta}$ (M=Mg, Ni, Mn, Cr, Fe, In, Sn): evaluation as potential anode materials for solid oxide fuel cells" *Solid State Ionics* **124** (1999) 61.

Srinivas K., Sarah P, Suryanarayana S. V., "Impedance spectroscopy study of polycrystalline $Bi_6Fe_2Ti_3O_{18}$" *Bull. Mater. Sci.* **26** (2003) 247.

Su W.F., Lu Y.T., "Synthesis, phase transformation and dielectric properties of sol–gel derived $Bi_2Ti_2O_7$ ceramics" *Mater.Chem.Phys*. **80** (2003) 632.

Subramanian M. A , Aravamudan G,. Subba Rao G. V, "Oxide pyrochlores — A review" *Prog. Solid State Chem.* **15** (1983) 55.

Taga Y., "Titanium oxide based visible light photocatalysts: materials design and applications" *Thin Solid Films*, **517** (2009) 3167.

Takai, S., Adachi T., Esaka T., "Investigation of the localized oxide ion interstitials of $PbWO_4$-based oxide ion conductors by means of impedance spectroscopy." *Mater. Res.Bull.* **41**(2006) 2088.

Takamura H., Tuller H.L. "Ionic conductivity of Gd_2GaSbO_7–$Gd_2Zr_2O_7$ solid solutions with structural disorder" *Solid State Ionics*, **134** (2000) 67.

Tatsumi K, Hibino M, Kudo T, "Synthesis of new tungsten bronze phases from peroxo-polytungstate precursors" *Solid State Ionics* **96** (1997) 35.

Tejada-Rosales E. M., Oro-Sole J., Gomez-Romero P., "Synthesis, characterization and electrical properties of the series of oxides $Ag_5Pb_{2-x}Cu_xO_6$ ($0.0 \leq x \leq 0.5$)," *J. Solid State Chem.,* **163** (2002) 151.

Thomas M., P. P. Rao, M. Deepa, M. R. Chandran, and P. Koshy, "Novel powellite-based red-emitting phosphors: $CaLa_{1-x}NbMoO_8$:$x$$Eu^{3+}$ for white light emitting diodes," *J. Solid State Chem.,* **182** (2009) 203.

Tian Z.R., Tong W., Wang J.Y., Duan N.G., Venkatesan V. K., Suib S.L "Manganese oxide mesoporous structures: mixed-valent semiconducting catalysts" *Science* **276** (1997) 926.

Tribotte B, Haussonne J. M, Desgardin G, "$K_2Sr_4Nb_{10}O_{30}$-based dielectric ceramics having the tetragonal tungsten bronze structure and temperature-stable high permittivity" *J. Eur. Ceram. Soc*. **19** (1999) 1105.

Vanderah T. A., Lufaso M. W., Adler A. U., Levin I., Nino J. C., Provenzano V., Schenck P. K. "Subsolidus phase equilibria and properties in the system Bi_2O_3:$Mn_2O_{3\pm x}$:Nb_2O_5" *J. Solid State Chem.* **179** (2006) 3467.

Vrieland E. G., Selwood P. W. "Semiconductivity in Eu_2O_3 and Gd_2O_3, and exchange interaction in the system MnO-MgO, as possible criteria for the catalytic decomposition of ammonia" *J. Catal.*, **3** (1964) 539.

Wakiya N, Wang J. K, Saiki A, Shinozaki K, Mizutani N, "Synthesis and dielectric properties of $Ba_{1-x}R_{2x/3}Nb_2O_6$ (R: rare earth) with tetragonal tungsten bronze structure" *J. Eur. Ceram. Soc.* **19** (1999) 1071.

R.E. Wilde "Raman spectrum of $Sr_{0.61}Ba_{0.39}Nb_2O_6$" *J. Raman Spectrosc.* **22** (1991) 321.

Xia H. R., Yu H., Yang H., Wang K. X. , Zhao B. Y., Wei J. Q., Wang J. Y., Liu Y. G. "Raman and infrared reflectivity spectra of potassium lithium niobate single crystals" *Phys. Rev. B* **55** (1997) 14892.

Yamauchi T., Ueda H., Ueda Y. "Observation of pressure-induced superconductivity in β-$Li_xV_2O_5$" *Phys.C: Superconduct.*, **460-462** (2007) 66.

Yan X., Xu G. "Effect of sintering atmosphere on the electrical and optical properties of $(ZnO)_{1-x}(MnO_2)_x$ NTCR ceramics" *Phys.B:Conden.Matt.*, **404** (2009) 2377.

Yanqing Y, Gaoke Z, Shujie Y, Xiong S, "Efficient removal of organic contaminants by a visible light driven photocatalyst $Sr_6Bi_2O_9$", *Chem. Eng. J.*, Article in Press, Available online 20 May 2010.

Yang K., Wang C.L., Li J.C., Zhao M.L., Wang X.Y, "Strain induced ferroelectricity in the $SrZrO_3$ / $SrTiO_3$ superlattice: First principles study" *Solid State Commun.*, **139** (2006) 144.

Yazawa K., Kamogawa H, Morisaki H. "Semiconducting TiO_2 films for photoelectrolysis of water" *Int. J. Hydrogen Energy* **4** (1979) 205.

Zhang H, Lü M, Liu S, Song X, Zhou Y, Xiu Z, Qiu Z, Zhang A, Ma Q, "Preparation and photocatalytic property of pyrochlore $Bi_2Ti_2O_7$ and (Bi, La) $_2Ti_2O_7$ films" *Thin Solid Films*, **517**(2008) 764.

Zheng W.P, Zu. R.D., Zhong L.W., "Nanobelts of semiconducting oxides" *Science* **291** (2001) 1947.

Zhou L., Wang W., Liu S., Zhang L., Xu H., Zhu W., "A sonochemical route to visible-light-driven high-activity $BiVO_4$ photocatalyst, "*J. Molecul. Cata. A: Chem.,* **252** (2006)120.

Zhou Y. C., Rahaman M. N., "Hydrothermal synthesis and sintering of ultrafine CeO_2 powders" *J. Mater. Res.* **8** (1993) 1680.

Zouari S, Ballou R, Cheikhrouhou A, Strobel P, "Structural and magnetic properties of the $(Bi_{2-x}Pr_x)Ru_2O_7$ pyrochlore solid solution $(0 \leq x \leq 2)$" *J. Alloys Compd.* **476** (2009) 43.